UNIVERSITÉ DE SHERBROOKE
Faculté de génie
Département de génie électrique et de génie informatique

DÉVELOPPEMENT D'UN MICROSCOPE À GUIDE D'ONDE À GAINE MÉTALLIQUE COMBINÉ AVEC FLUORESCENCE P L'IMAGERIE DE CELLULES VIVANTES

DEVELOPMENT OF A COMBINED METAL CLAD WAVEGUIDE AND SURFACE ENHANCED FLUORESCENCE MICROSCOPE FOR LIVE CELL IMAGING

Thèse de doctorat
Spécialité : génie électrique

Thomas SÖLLRADL

Jury : Paul CHARETTE (directeur)
Michel GRANDBOIS (directeur)
Michael CANVA
Serge Charlebois
Jean-François Masson

Sherbrooke (Québec) Canada Octobre 2018

To my parents, who gave me roots to grow wings so I can fly.
I will be forever grateful for your unconditional love and support!

RÉSUMÉ

Il y a un intérêt grandissant dans les domaines de la biologie cellulaire et de la pharmacologie pour la détection fiable d'interactions cellule-cellule et d'activités résultantes de l'interaction cellulaire avec l'environnement physique et biochimique. Les techniques de détection sans marquage, telles que celles basées sur la résonance plasmonique de surface, les réseaux de diffraction ou la spectroscopie d'impédance électrique, sont désormais utilisées de façon routinière. Celles-ci permettent de mesurer, entre autres, les signaux cellulaires sous-jacents et l'activité fonctionnelle des cellules exposées à des hormones, des agents pharmacologiques ou encore, des toxines.

Lors de ces tests, le signal mesuré est issu de plusieurs cellules. Il est généralement supposé que le profil de réponse cellulaire est homogène parmi la population de cellules testées. Or, de plus en plus de publications tendent à mettre en évidence un haut niveau d'hétérogénéité au sein d'une population de cellules. Bien que pourvues d'une grande sensibilité, les techniques précédemment mentionnées ont des lacunes en termes de résolution spatiale et de profondeur de sondage, ce qui rend impossible la détection d'activité cellulaire individuelle. Le niveau de complexité augmente lorsque l'on considère que les profils de réponses cellulaires résultent d'un amalgame de divers événements de signalisation cellulaire individuels, ce qui rend difficile l'extraction de la contribution d'une composante précise du signal global mesuré.

Dans cette thèse, une plate-forme d'imagerie a été développée en combinant deux méthodes, l'une sans et l'autre avec marquage. Ces méthodes sont respectivement les guides d'ondes à gaine métallique (MCWG, metal clad waveguide) et la fluorescence exaltée en surface (SEF, surface enhanced fluorescence). L'objectif est de simultanément visualiser et quantifier les signalisations et activités fonctionnelles des cellules individuelles. Des simulations numériques sont présentées qui illustrent les performances attendues du système. Le système a été testé expérimentalement sur une combinaison d'échantillons synthétiques bien définis et de nombreuses cellules vivantes génériques, de nature variée. Nous avons montré que la plateforme MCWG proposée peut atteindre une grande profondeur de mesure (>600 nm) tout en maintenant une bonne résolution latérale (5 μm), permettant ainsi l'observation de cellules individuelles. Contrairement à l'imagerie MCWG, le signal obtenu en SEF ne dépend pas d'un mode de propagation et sa résolution est limitée seulement par la diffraction.

Il a été possible de montrer le caractère hétérogène d'une petite population de cellules en mesurant, sans employer de marqueur, les variations de signalisations et de la morphologie cellulaire. Le caractère unique de chaque cellule en lien avec son profil de réponse a été détecté et quantifié par la mesure de l'activité intracellulaire de cellules endothéliales en état d'apoptose induite. Dans une seconde série d'expériences, le système a été employé pour étudier les changements dans l'intégrité d'un film de cellules confluentes exposé à des stimuli biochimiques. L'utilisation du mode d'imagerie MCWG a permis d'illustrer le lien direct entre le signal mesuré et la formation d'interstices intercellulaires dans la monocouche de cellules.

Les avantages d'un système combiné exploitant des approches avec et sans marqueurs ont été montrés. Ceci a été réalisé par l'emploi de marqueurs fluorescents afin d'associer les variations dans les composantes moléculaires et structurelles des cellules au signal MCWG mesuré. Plus

spécifiquement, le système d'imagerie a été utilisé dans le but de visualiser le cytosquelette de cellules musculaires lisses vasculaires. Finalement, la plateforme d'imagerie a été exploitée afin de mesurer l'activité des signaux médiés par les récepteurs. L'analyse simultanée du signal MCWG, lequel n'emploie pas de marqueur, et du signal calcique associé à l'activation du récepteur de l'angiotensine 1 a permis d'identifier certains éléments caractéristiques du signal obtenu sans marqueur. De plus, en utilisant des inhibiteurs pharmacologiques, il a été possible d'isoler certains chemins de signalisations dans l'activité cellulaire observée.

Mots-clés : Microscopie sans marqueurs, microscopie par fluorescence, biodétection cellulaire, hétérogénéité, plasmons de surfaces, guides d'ondes à gaine métallique.

ABSTRACT

There is a sustained interest in the field of cell biology and pharmacology to reliably detect cell-cell interaction or their signaling and functional activities resulting from their interactions with the physical and biochemical environments. Label-free sensing techniques based on surface plasmon resonance, diffraction grating and electrical impedance spectroscopy are now routinely used for monitoring the underlying cell signaling and functional activity when exposed to hormones, pharmacological agents and toxins.

In these assays, the measured signal derives from the summation of many cells, thereby assuming that the underlying cell response profile is homogeneous within the tested cell population. There is, however, an increasing body of evidence demonstrating a high level of cell-to-cell heterogeneity within a cell population. While highly sensitive, these techniques often lack the spatial resolution and probing depth to detect individual cell signaling activity, thereby hindering the detection heterogeneous cellular activity. Further complexity arises from the fact that cellular response profiles are an integration of complex intracellular signaling events which makes it challenging to precisely delineate the contribution of the underlying intracellular components on the obtained signal profiles.

In this thesis, an imaging platform was developed combining a label-free and label based imaging modality, namely metal clad waveguide (MCWG) and surface enhanced fluorescence (SEF), for the simultaneous visualization and quantification of individual cell signaling and functional activity. Numerical simulations are presented, demonstrating the expected performance of the system and the developed system was experimentally characterized with a combination of well-defined synthetic samples and various live cells models. We have shown that the proposed MCWG imaging platform can achieve a deep probing depth (> 600 nm) while maintaining a lateral resolution (5 μm) allowing the resolution of individual cells. Unlike MCWG imaging, the SEF signal is not dependent on a propagating mode and diffraction limited resolution was achievable.

The label-free detection of cell-to-cell heterogeneity was demonstrated by the real-time monitoring of cell signaling activity and morphological changes in a small population of cells. Heterogeneity in individual cell response profiles was successfully detected and quantified within apoptosis-induced intracellular activity in an endothelial cells model. In a second set of experiments, the system was used to assess changes in the integrity of a confluent cell layer exposes to biochemical stimuli. In this experiment, MCWG imaging modality has allowed to establish a direct link between the obtained sensor signal and the formation of intercellular gaps in the cell monolayer.

The advantages of a combined label-free and label based imaging approach were demonstrated by using fluorescent markers to detect underlying molecular and structural cellular components associated with the MCWG signal. The imaging system was used for the visualization of actin cytoskeleton within vascular smooth muscle cells. Finally, the imaging platform was applied to monitor receptor-mediated signaling activity. The simultaneous analysis of the MCWG label-free signal and the SEF intracellular calcium signal from angiotensin 1 receptor activation

allowed the attribution of label-free signal features. Further, using pharmacological inhibitors allowed to delineate specific signaling pathways in the observed cellular activity.

Keywords : label-free microscopy; fluorescence microscopy, cell-based biosensing; heterogeneity; surface plasmons; metal clad waveguides;

TABLE OF CONTENTS

TABLE OF FIGURES

LIST OF ACRONYMS

Acronym	Definition
AngII	Angiotensin II
AT1R	Angiotensin 1 Receptor
ATR	Attenuated Total Reflection
CBB	Cell-Based Biosensor
CBA	Cell-Based Assays
CCD	Charge Coupled Device
DNA	Deoxyribonucleic Acid
FOV	Field of View
GFP	Green Fluorescent Protein
GPCR	G-Protein Coupled Receptor
HEK293	Human Endothelial Kidney Cells
LOD	Limit of Detection
LR-SPR	Long-Range SPR
MCWG	Metal Clad Waveguide
MCWGI	Metal Clad Waveguide Imaging
NA	Numerical Aperture
RI	Refractive Index
ROCK	Rho-Associated Protein Kinase
RWG	Refractive Waveguide Grating
PAR1	Proteinase-Activated Receptor 1
SPR	Surface Plasmon Resonance
SPRI	Surface Plasmon Resonance Imaging
SNR	Signal-to-Noise Ratio
SP	Surface Plasmon
SPEF	Surface Plasmon Enhanced Fluorescence

TE	Transverse Electric
TIRF	Total Internal Reflection Fluorescence
TRAIL	Tumor Necrosis Factor-Related Apoptosis-Inducing Ligand
TM	Transverse Magnetic
TRITC	Tetramethylrhodamine

CHAPTER 1 Introduction

1.1 Context and Research Problem

Recent developments in the fields of cell biology and pharmacology lead to an increased understanding of how cells sense and interact with their microenvironment and how intracellular signaling events play a major role in maintaining and regulating their functions. This knowledge triggered the development of whole new research fields such as synthetic biology, making it possible to genetically design novel organisms acting as living sensors systems [Levskaya *et al.*, 2005], for therapeutic applications such as cancer therapy [Anderson *et al.*, 2006] or for the commercial production of drugs [Paddon *et al.*, 2013]. These systems, however, require a reliable detection technique (transducer) converting the changes in cellular activity triggered by external stimuli into quantifiable and measurable signals. Different transducer technologies have been developed, with the most widely used approach being the generation of fluorescent dyes (e.g. green fluorescent protein (GFP)) to detect specific signaling events or observe gene transcription [Tsien, 1998]. While highly sensitive to specific hallmarks during intracellular signaling, the use of gene transcription and synthesis of these dyes render such secondary readout mechanisms rather slow, putting the response time in the range of hours. Further, these markers have been reported to sometimes interfere with the cell response itself [Aizawa *et al.*, 1997] and the signal reflects only a small aspect in a larger, more complex signaling cascade leading to the integrated functional response of the cell.

More recently label-free transducer technologies such as electrical impedance spectroscopy [Tiruppathi *et al.*, 1992] and evanescent based technologies such as refractive waveguide grating (RWG) [Fang *et al.*, 2006] and surface plasmon resonance (SPR) [Chabot *et al.*, 2009] have successfully been applied to detect minute changes in cellular activity, providing insight in endothelial function [Benson *et al.*, 2013], apoptosis [Arndt *et al.*, 2004; Maltais *et al.*, 2012] and G-protein coupled receptor (GPCR) signaling [Schröder *et al.*, 2010; Scott & Peters, 2010]. These label-free platforms provide signals similar to classical approaches without the need of exogenous labels and allow for real-time quantification of cellular activity and function.

While highly sensitive, sensor signals of most label-free assays originate form a large number of cells (typically ranging from 100 to 4000). While cell populations are commonly assumed to behave homogeneously within a population, and there is an increasing body of evidence showing that even among genetically identical cells, distinct phenotypical sub-groups exist within a given population [Samadani *et al.*, 2006; Slack *et al.*, 2008]. Such phenotypical heterogeneity is involved in various physiological processes during development [Bahar *et al.*, 2006; Colman-Lerner *et al.*, 2005] or in pathological processes such as tumor heterogeneity [Campbell & Polyak, 2007]. However, label-free sensing technologies lack of a sufficiently high spatial resolution down to a single cell level. This hinders the detection of such heterogeneity and therefore these systems cannot detect phenotypical heterogeneity within a cell population. Evanescent field based sensing platforms such as RWG and SPR natively support imaging and have the potential to overcome this limitation. These methods have been applied to study receptor-ligand binding kinetics, detecting binding events happening at the very proximity of the sensor's surface [Homola, 2003]. For example, most common SPR systems operated in the visible spectral range offer probing depths (defined as the distance at which the evanescent field amplitude decays to $1/e$ of its surface value) in the range up to 200 nm [Homola, 2003]. However, when probing microscopic sized objects such as cells, common structures of interest may be located higher up in the cell body (i.e. actin-cytoskeletal components > 100 nm; intracellular organelles > 200 nm). Thus, a system offering a deeper probing depth (> 200 nm) while maintaining individual cell resolution (< 10 μm) is desirable when one wants to reliably extract individual cell signaling activity.

Further complexity arises from the fact that label-free technologies rely on probing a certain physical property such as the refractive index in the case of evanescent field based assays. The measured cellular structures and organelles have distinct optical properties depending on their molecular density and distance within the probed volume, thereby contributing to varying degrees to the measured sensor signal. Thus, the obtained signal represents multiple intracellular structures, thus to delineate the contribution of individual signaling events and structural components within the signal can often be challenging. To overcome this challenge, evanescent field based methods offer another advantage due to their native support for fluorescence excitation similar to conventional total internal reflectance fluorescence (TIRF) microscopy. For

SPR this technique is termed surface plasmon enhanced fluorescence (SPEF) spectroscopy [Liebermann & Knoll, 2000]. Such a combined label-free and labeled based approach has been used to enhance the detection limits and specificity of biomolecular binding assays [Yao *et al.*, 2004]. More recently, SPEF was also successfully applied to living cells, thereby visualizing the underlying structural components associated with the sensor's signal within a large population of cells [Chabot *et al.*, 2013; He *et al.*, 2006, 2009]. While these studies demonstrate the feasibility of such a combined approach, the lack of high resolution imaging as well as the shallow probing depth limited these studies to structures in the very basal section of the cell and to large populations of cells.

1.2 Research Question and Objectives

To overcome these limitations, the central goal of this work was **to develop a deep probing depth evanescent field based imaging platform for simultaneous label-free and labeled based characterization of individual cell activity**. The advantages of such a combined approach were demonstrated by the visualization and quantification of individual cell activity for different cell types and applications. Such integral assessment of cellular activity ultimately allows one to monitor specific intracellular signaling events and structures, thereby delineating their impact on the obtained label-free sensor signal.

This goal was achieved by completing the following objectives:

1) Development of a high magnification imaging platform capable of discriminating individual cellular activity in both label-free and labeled based imaging modalities.

2) Optimize, fabricate and characterize deep-probe evanescent field based sensor chips. Such sensor chips must be operated at visible wavelengths for fluorescence excitation while maintaining a deep sensing depth and a high resolution to discriminate individual cells.

3) Detect heterogeneity within a cell population and demonstrate the systems' sensing capabilities. Quantify cell-cell heterogeneity and characterize the impact of cellular features on the measured sensor's signal.

4) Demonstrate the benefits of a combined label-free and labeled based sensing approach for simultaneous visualization and quantification of cellular activity, in order to delineate the specific underlying signaling events and structure leading to the sensor's signal detected at a single cell level.

1.3 Thesis Organization

The document is structured in six chapters. After the introduction (Chapter 1), different fundamental concepts from the field of integrated optics form the basis for an overview on different label-free sensing technologies with a focus on evanescent field based sensing (Chapter 2). Further, the different design parameters are discussed in order to optimize the sensor chip and achieve deeper probing depth while maintaining a high spatial resolution using a special class of waveguides, namely metal clad waveguides (MCWGs).

Chapter 3 provides details on the developed imaging platform and the underlying optimization of MCWG based sensor chips. Simulation results are presented, showing how an informed choice was made to obtain the optimal sensor structure that allows for high resolution, deep penetration depth imaging. Further, experimental results are shown demonstrating the system's imaging capabilities on both synthetic and biological samples. This chapter is presented as a scientific article which was published in Optics Express with the title of *"Metal Clad Waveguide (MCWG) Based Imaging using a High Numerical Aperture Microscope Objective"*.

Chapter 4 presents the application of the developed system on live cell sensing using the label-free sensing modality. Two applications are demonstrated with one focusing on intracellular events following the apoptotic response within an endothelial cell population. The second application shows how the additional information from the label-free imaging platform can be used to monitor cell monolayer integrity. This chapter is based on the scientific article published in Biosensors & Bioelectronics under the title "*Label-free visualization and quantification of single cell activity using metal-clad waveguide (MCWG)-based microscopy*".

Chapter 5 combines both the label-free and labeled based imaging modalities for integrated visualization and quantification of individual cellular signaling activity. The capabilities of the system are demonstrated by visualizing the actin cytoskeleton within vascular smooth muscle cells. Individual cell signaling activity is quantified in HEK293-AT1R by following intracellular calcium levels using the fluorescent dye Fluo-8 upon activation of the Angiotensin 1 receptor by its ligand Angiotensin II. The involvement of different intracellular signaling cascades is probed and the advantages of such integral cell assessment are demonstrated. This chapter is based on the draft of a scientific article to be submitted to Biosensors & Bioelectronics under the title "*Monitoring Individual Cell Signaling Activity using Combined Metal Clad Waveguide and Surface Enhanced Fluorescence Microscopy*".

The chapters 6 and 7 present a general discussion and conclusion of the different aspects realized during this work along with an outlook for potential further investigations.

CHAPTER 2 State of the Art

This chapter will introduce different concepts and topics to understand evanescent field based biosensors and their application to cell based biosensing. Initially, the field of integrated optics will be introduced with a focus given on dielectric slab waveguides. This section is followed by surface plasmon resonance (SPR), one of the most widely applied biosensing techniques nowadays. After SPR, a special class of waveguides, namely metal clad waveguides (MCWG), will be discussed. For both SPR as well as the MCWG, an overview of their current applications in biosensing, and in particular cell-based biosensing is given. Besides these two evanescent field based biosensing technologies, two other technologies have emerged for the label-free study of cell activity and behavior which will be briefly discussed following the MCWG section. Evanescent field based sensing technologies natively support microscopy and different imaging concepts have been proposed. These systems along with their application to cellular imaging will be discussed towards the end of this chapter. The chapter concludes by a brief description of how the evanescent field can be used to excite fluorophores and how a combination of label free and label based sensing complement each other in the assessment of cell activity.

2.1 Integrated Optics

The field of integrated optics is concerned with the phenomena of light guided along a thin dielectric film or strip. Since nearly all evanescent based sensor concepts involve some sort of guided light along various waveguide structures, it is important to introduce the underlying concepts of this field to understand the different aspects and behaviors of these sensing technologies.

2.1.1 Refraction, Reflection and Polarization of Light

Let us consider an interface separating two lossless, isotropic, homogeneous dielectric materials with refractive index n_1 and n_2, respectively (Figure 2.1). Light travelling within one of the media undergoes repetitive scattering and re-scattering due to interaction with the medium itself. As such the medium induces repetitive phase shifts of the light which becomes apparent as the phase velocity of the light beam within the media changes compared to the speed of light in

vacuum. This change is expressed as the refractive index n of the media representing the ratio of the phase velocity (υ) inside the media compared to the speed of light (c):

$$n = \frac{c}{v} \text{ and } n = \sqrt{\varepsilon_r \mu_r} \tag{0.1}$$

with ε_r being the relative permittivity and μ_r the relative permeability of the material. Note that most natural materials are non-magnetic at optical frequencies and thus $\mu_r \approx 1$ and $n \approx \sqrt{\varepsilon_r}$ [Hecht, 2002]. If the media is not vacuum and interacting with the light (n > 1) the result is a decreased wave speed. Certain materials (such as metals) do, however, not only alter the speed the wave travels within the media but also its amplitude (i.e. absorption). These materials therefore have a complex refractive index which can be expressed as:

$$\tilde{\varepsilon}_r = \varepsilon'_r - i\varepsilon''_r = \tilde{n}^2 = (n - ik)^2 \tag{0.2}$$

For such materials, the real part of the refractive index (n) represents the ratio of the speed light travelling inside the media with that of vacuum (0.1) while the imaginary part (k) provides information about the decay rate of the wave amplitude inside the media.

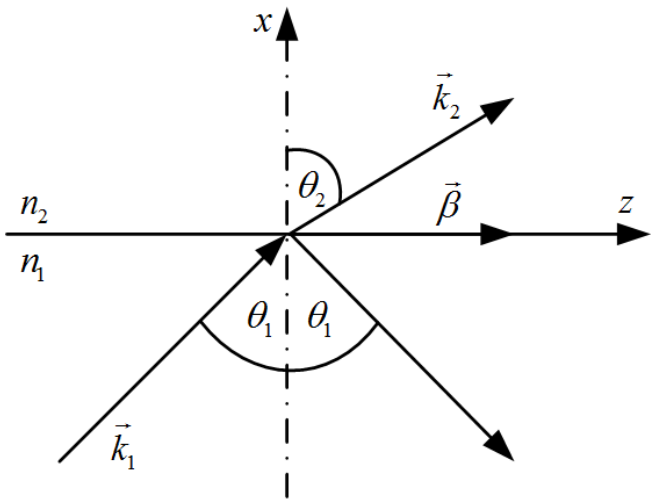

Figure 2.1: Refraction and reflection at an interface ($n_1 > n_2$ and $\theta_2 > \theta_1$)

As shown in Figure 2.1 a light wave, with propagation direction indicated by its wave vector $\vec{k}_1$, perpendicular to the wave fronts of a uniform, monochromatic plane wave with wavelength λ is incident at an angle θ_1 to the interface ($n_1 > n_2$).

The amplitude of $\|\vec{k}\|$ is given as:

$$\|\vec{k}\| = \frac{}{\lambda} \tag{0.3}$$

The light wave will be partially refracted and reflected at the interface and its exit angle θ_2 is given by Snell's Law:

$$n_1 \sin\theta_1 = n_2 \sin\theta_2 \tag{0.4}$$

$$\|\vec{k}_1\| \sin(\theta_1) = \|\vec{k}_2\| \sin(\theta_2) \tag{0.5}$$

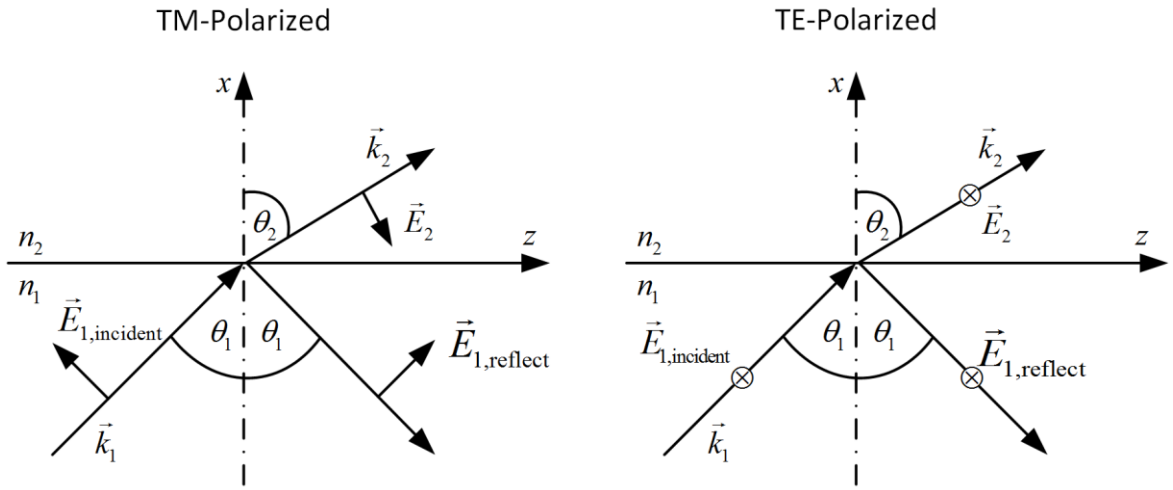

Figure 2.2: Polarization of light. The direction of the electric field with respect to the plane of incidence (x,z) determines the polarization of the light. If the E-Field is in the plane of incidence it is referred to as *transverse magnetic* (TM). If it is perpendicular to the plane of incidence it is *transverse electric* (TE).

While Snell's Law provides the direction of the reflected and transmitted waves, it does not describe the amplitudes of these components. The amplitudes are dependent on the angle of incidence and the polarization of the light and is given by the Fresnel formulas. The polarization of the light gives the orientation of the electric and magnetic fields of the wave with respect to the plane of incidence (Figure 2.2). If the electric field is in the plane of incidence, the light polarization is *transverse magnetic* (TM). On the other hand, if the electric field is perpendicular to the plane of incidence, it's polarization is *transverse electric* (TE). The Fresnel Equations yield the complex reflection and transmission coefficients (r and t) of the wave components and are dependent on their polarization:

$$TE: \mathrm{r}_{12\perp} = \frac{\mathrm{n}_1\cos\theta_1 - \mathrm{n}_2\cos\theta_2}{\mathrm{n}_1\cos\theta_1 + \mathrm{n}_2\cos\theta_2} \; and \; t_{12\perp} = \frac{2n_1\cos\theta_1}{\mathrm{n}_1\cos\theta_1 + \mathrm{n}_2\cos\theta_2}$$
$$TM: \mathrm{r}_{12\parallel} = \frac{\mathrm{n}_2\cos\theta_1 - \mathrm{n}_1\cos\theta_2}{\mathrm{n}_2\cos\theta_1 + \mathrm{n}_1\cos\theta_2} \; and \; t_{12\parallel} = \frac{2n_1\cos\theta_1}{\mathrm{n}_2\cos\theta_1 + \mathrm{n}_1\cos\theta_2} \quad (0.6)$$

These equations describe the reflection and transmission coefficients at an interface as shown in Figure 2.1. These equations can be coupled to describe the reflectivity of a multi-layer stack based on the Abeles matrix method [Abelès, 1950]. Dr. Pierre-Jean Zermatten together with Dr. Vincent Chabot developed a MatLab program in the Biophotonics group of the University of Sherbrooke which is based on this formalism [Yeh, 2005]. The initial version of this code was further modified throughout this thesis and reflected light simulations presented throughout this thesis are based on this code.

2.1.2 Total Internal Reflection and the Evanescent Field

Using the Fresnel Equations (0.6), the reflected and transmitted light intensities for a monochromatic incident light wave can be calculated. Figure 2.3 shows such reflected and transmitted light intensities expressed as the reflectances ($R_{12\perp} = |r_\perp|^2 \; and \; R_{12\parallel} = |r_\parallel|^2$) and the transmittances ($T_{12\perp} = |t_\perp|^2 \; and \; T_{12\parallel} = |t_\parallel|^2$) for a glass/water interface (n_{Glass} = 1.524, n_{Water} = 1.336) for a monochromatic light wave (λ = 470 nm) as a function of the angle of incidence and polarization. While at lower angles of incidence most light gets transmitted (Figure 2.3 B) something interesting happens when θ_i approaches and exceeds the critical angle θ_c (e.g. 61.30° in this case, Figure 2.3 C). The angle of transmittance θ_t becomes 90° and all incident light is reflected back from the surface ($|R| = 1$), a phenomenon known as total internal reflection.

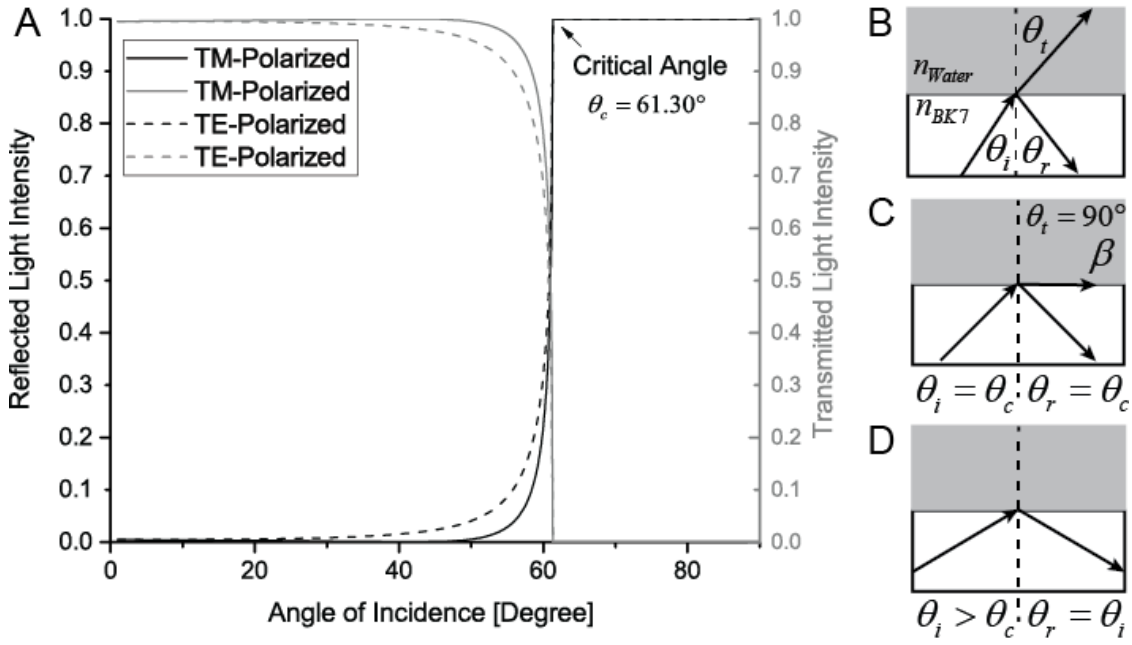

Figure 2.3: Simulated reflected and transmitted light intensity as a function of the angle of incidence for a glass/water interface (n_{Glass} = 1.524, n_{Water} = 1.336) for a monochromatic light wave (λ = 470 nm) (A). B) For $\theta_i < \theta_c$ Part of the light gets reflected back and part is transmitted into the water. C) At the critical angle θ_t becomes 90° and total internal reflection occurs. D) For angles above the critical angle $\theta_i = \theta_r$.

The wave in the top medium beyond the angle of TIR can be described by starting from the general expression for a plane wave with an angular frequency of $\omega = 2\pi f$:

$$\vec{E}(x,y,z,t) = \vec{E}_m(x,y,z)e^{j(\omega t \pm \vec{k}\,)} \tag{0.7}$$

With

$$\begin{aligned} \vec{k} &= k_x\hat{e}_x + k_y\hat{e}_y + k_z\hat{e}_z \\ \vec{r} &= ze_x + y\hat{e}_y + z\hat{e}_z \end{aligned} \tag{0.8}$$

After solving Snell's Law for the above case of TIR (complex with $\sin(\theta_t) > 1$), one finds that there exists a wave at the water/glass interface (E_2) which can be described as [Hecht, 2002]:

$$E_2(x,z) = E_{m2}e^{\pm\alpha x}e^{-j\beta z} \tag{0.9}$$

where E_{m2} is the electric field amplitude, α is the decay rate of the wave along the x-axis and β is the propagation constant of the wave. Thus, an evanescent wave exists traveling parallel along the interface (along the z-axis, attributed by $e^{-j\beta z}$ in (0.9)) with an amplitude that exponentially decays away from to the interface (along the x-axis, attributed by $e^{\pm\alpha x}$ in (0.9)).

The electric field profile for such a water/glass interface is shown in Figure 2.4. Due to constructive interference of the incoming and reflected light at θ_c a small increase in the electric field amplitude can be seen [Liebermann & Knoll, 2000] at the interface which rapidly diminishes away from the glass surface. The depth with which the wave amplitude decays to 1/e (≈37 %) of the value at the interface is called the penetration depth, L_{pen}:

$$L_{pen} = \frac{1}{\alpha} \tag{0.10}$$

where α is the decay rate of the wave amplitude along the x-axis. For the visible spectra it lies typically within hundreds of nanometers away from the interface. The evanescent wave and its penetration into the dielectric (i.e. water in the example above) is of central importance for optical sensors and will be part of deeper discussions later on.

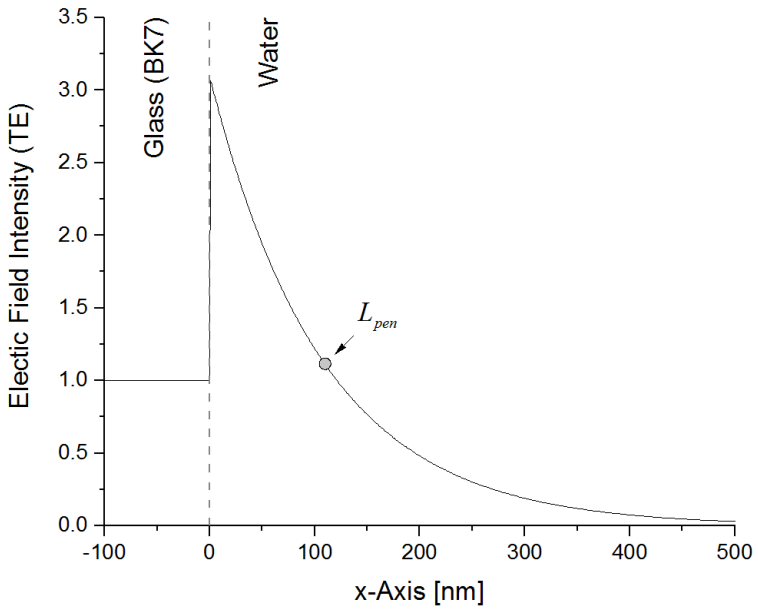

Figure 2.4: Simulated electric field intensity profile for a glass water interface at an angle of incidence of 65° (n_{Glass} = 1.524, n_{Water} = 1.336) for a monochromatic light wave (λ = 470 nm). The electric field amplitude rapidly diminishes in the water. The depth where it decreased to 1/e of its value at the interface is indicated as the penetration depth (gray dot, L_{pen} = 109 nm)

2.1.3Dielectric Slab Waveguides

If a thin, high refractive index dielectric layer is placed on top of the glass substrate, this dielectric slab can then act as the simplest form of an optical waveguide. Figure 2.5 shows a schematic of such a dielectric slab waveguide. It consists of a thin core layer and two semi-infinite volumes surrounding the core layer namely the substrate and the cladding, respectively. For the structure to act as a waveguide the refractive index of the core must be higher than that of the substrate and the cladding ($n_{core} > n_{Substrate} \geq n_{Cladding}$).

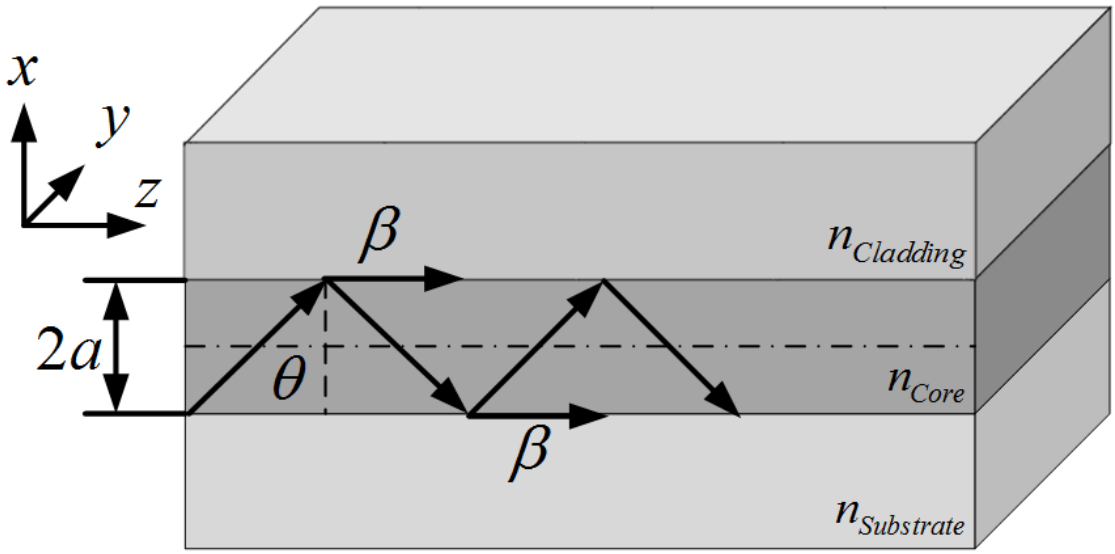

Figure 2.5: Schematic of a dielectric slab waveguide. A thin dielectric layer of a higher refractive index (n_{Core}) forms the core of the waveguide and is surrounded by two semi-infinite volumes having lower refractive indices ($n_{Substrate}$ and $n_{Cladding}$).

For $\theta < \theta_c$ the light is only partially reflected (Figure 2.3 B) and a part will escape the dielectric slab through the cladding or the substrate, respectively. Such modes are also referred to as *radiative modes*. For the case of TIR at each interface ($\theta > \theta_c$) the light can be guided as shown in Figure 2.5. However, not all $\theta > \theta_c$, but rather a discrete set of θ will result in so called *guided modes*. To obtain the θ for which guided modes exists one has to have a look at the phase shifts (φ) imposed on the reflected light for each reflection at the interface [Tamir, 1975]:

$$R = e^{2j\varphi} \tag{0.11}$$

The polarization dependent phase shifts are given by the Fresnel equations as:

$$\tan(\varphi_{TE}) = \frac{\sqrt{n_{Core}^2 \sin^2(\theta) - n_{Sub./Clad.}^2}}{n_{Core}\cos\theta}$$
$$\tan(\varphi_{TM}) = \frac{n_{Core}^2}{n_{Sub./Clad.}^2}\frac{\sqrt{n_{Core}^2 \sin^2(\theta) - n_{Sub./Clad.}^2}}{n_{Core}\cos\theta} \quad (0.12)$$

For the structure shown in Figure 2.5, a phase shift of $kn_{core}2a\cos(\theta)$ for each transverse passage (core/cladding and core/substrate) results in two phase shifts of $-2\varphi_{Core/Clad.}$ and $-2\varphi_{Core/Sub.}$, respectively. For constructive interference and a guided mode to exist, the sum of these phase shifts has to be a multiple of 2π. Thus, the self-consistency condition can be expressed as [Tamir, 1975]:

$$4kn_{core}a\cos\theta - 2\varphi_{substrate} - 2\varphi_{core} = 2\nu\pi \quad (0.13)$$

where ν is an integer (0,1,2…) and is called the *mode number*. From Equation (0.13) the propagation constant (β) of the guided modes for this structure can be derived and is given as:

$$\beta = kn_{eff} = \frac{2\pi}{\lambda}n_{eff} \; with \; n_{eff} = n_{Core} * \sin(\theta) \quad (0.14)$$

The effective refractive index (n_{eff}) determines the velocity of the guided light of the mode.

If, for example, a thin (2a = 500 nm) high refractive index dielectric (i.e. a photoresin such as KMPR, n_{Core} = 1.58) is deposited in between the glass and water volumes, such a structure can act as a waveguide for a monochromatic wave (λ = 470 nm). The propagation constant of the mode can be calculated from Equation (0.14) using numerical tools or mode solvers (e.g. MatLAB or FIMMWAVE). Using this approach, the effective index for the first order modes presented in Figure 2.6 was determined to be $n_{eff,TM}$ = 1.5502 and $n_{eff,TE}$ = 1.5526, respectively. For a given thickness of 500 nm, only one single solution is found for each polarization and the waveguide is referred to as a *single mode waveguide*. Having determined the propagation constant of the modes, the electric field along the x-axis can also be calculated [Pollock & Lipson, 2003]. Figure 2.6 shows the electric field amplitude across the three layer stack (Glass/KMPR/Water). Since $n_{Substrate} \neq n_{cladding}$ the resulting electic field profile is asymmetric, with a larger portion of the energy in the cladding with the higher refractive index (i.e. glass) and the waveguide is called an *asymmetric dielectric slab waveguide*. As with TIR, an electric

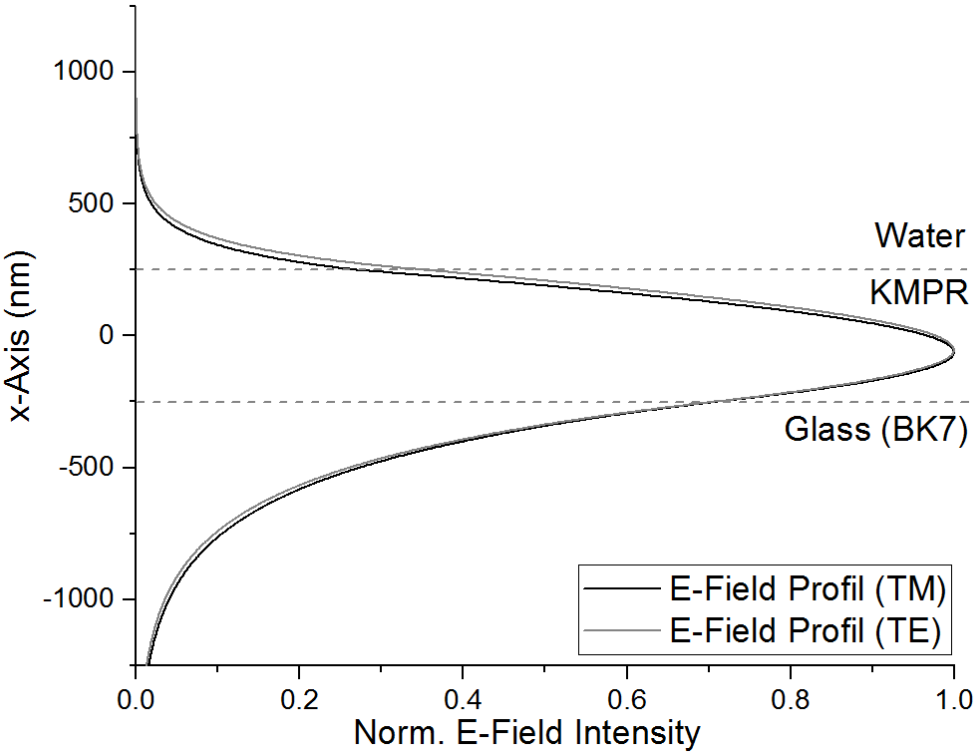

Figure 2.6: Simulated E-Field profile for a dielectric slab waveguide. A thin high refractive index dielectric layer (KMPR, n_{Core} = 1.58) forms the core of an asymmetric dielectric slab waveguide in between a glass substrate (BK7, $n_{Substrate}$ = 1.52) and water ($n_{Cladding}$ = 1.33).

field penetrates in the cladding volume (water and glass) evanescently decaying along the x-axis. In the following, two biosensing techniques will be discuhat utilize this phenomenon to detect binding of biomolecules and follow cellular activity as evanescent field based biosensors.

2.2 Surface Plasmon Resonance (SPR)

Following the discovery of abnormalities in the absorption spectra of polychromatic light from a metallized diffraction grating by Wood in 1902 [Wood, 1902], it was not until 1968 that the effect of surface plasmon resonance was understood simultaneously by Otto and Kretschmann [Kretschmann & Raether, 1968; Andreas Otto, 1968]. In the early 1980s, Liedberg and Nylander were the first to demonstrate that SPR could be used for both gas and biomolecular sensing applications[Bo Liedberg *et al.*, 1983; Nylander *et al.*, 1982]. This lead to the launch of the first commercial SPR platform in 1990: the BIAcore [B Liedberg *et al.*, 1995]. Over the past decades

and following the initial proofs of concept, SPR was applied to a wide range of applications as a label-free sensing approach in the fields of chemistry, engineering and biology.

2.2.1 Definition of Surface Plasmons

A surface plasmon (SP) is a charge density oscillation at the interface between a metal film and a dielectric [Barnes *et al.*, 2003]. Solving Maxwell's equations with the appropriate boundary conditions yields the frequency dependence of the complex SP propagation constant [Jirí Homola, 2006] :

$$\tilde{\mu}_{plasmon} \quad \beta'' + i\beta'' = k_0 \sqrt{\frac{\varepsilon'_M \varepsilon_D}{\varepsilon'_M + \varepsilon_D}} + \mathrm{i} \frac{\varepsilon''_M}{2(\varepsilon'_M)^2} \mathrm{k}_0 \left(\frac{\varepsilon'_M \varepsilon_D}{\varepsilon'_M + \varepsilon_D} \right)^{3/2} \tag{0.15}$$

where β' and β'' are the real and imaginary parts of the propagation constant, k_0 represents the free space light wave vector, ε_M and ε_D are the permittivity of the metal and dielectric, respectively. For a guided mode (called the *surface plasmon mode* or simply surface plasmons) to exist, the real parts of the metal and the dielectric permittivity must have opposite sign for SP to occur at the interface [Jirí Homola, 2006]. Note that surface plasmons are a *surface mode* with exponential decay of the field on each side of the interface. Several metals meet these conditions (permittivity with negative real part) at visible wavelengths such as Au, Ag and Cu, with Au being the one most commonly used in sensing applications due to its chemical stability and sensitivity [Homola, 2003]. Note that a metal/dielectric interface only support a mode for

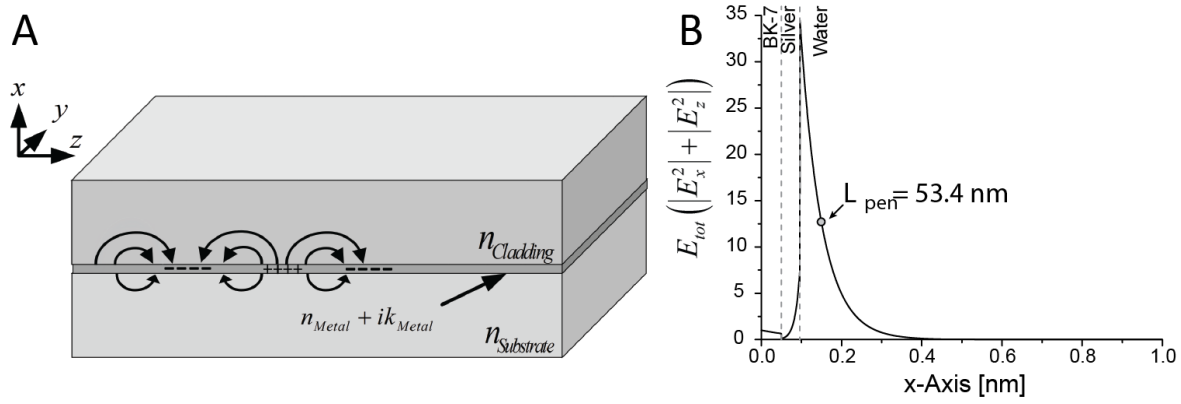

Figure 2.7: SPs at a metal/dielectric interface A. Surface plasmons are charged density oscillation at the metal/dielectric interface. B. Simulated total electric field profile for a BK7/46 nm Ag/Water structure exited at 470 nm. The electric field sharply diminishes in the dielectric layer (water).

TM polarized light (Figure 2.7A). The guided surface wave character of the SP leads to an electric field normal to the interface, which decays exponentially away from the interface (Figure 2.7B) [Homola, 2003]. As the propagation constant of the surface plasmon mode has a non-zero imaginary part, it exhibits attenuation. This attenuation is defined as the distance L in direction of propagation at which the energy of the mode decays to 1/e of its steady-state value [Jirí Homola, 2006]:

$$L = \frac{1}{2\beta''} \tag{0.16}$$

The finite attenuation length has great consequences for the use of surface plasmon based imaging techniques, effectively reducing the achievable lateral resolution for such systems. This will be part of a deeper discussion in Section 2.4.2.

2.2.2Excitation of Surface Plasmon Resonance

To excite surface plasmon resonance, the wave vector of the incident light has to match the SPR wave vector. The most widely used coupling technique is based on a so-called attenuated total reflection (ATR) technique first demonstrated by Kretschmann [Kretschmann & Raether, 1968]. In this configuration, the incident light is reflected at an angle superior to the critical angle at the interface between a high refractive index prism and the bottom side of a thin metal layer. Under phase-matching conditions, the light evanescently tunnels through the metal layer and the TM polarized part of the light excites SPs on the opposing metal surface. The magnitude of the wave vector component along the x-axis of the incident light is:

$$k_{Photon\,ATR} = \frac{2\pi}{\lambda} n_p \sin\theta \tag{0.17}$$

where λ is the wavelength of the incident light, n_p is the refractive index of the prism and θ is the angle of incidence.

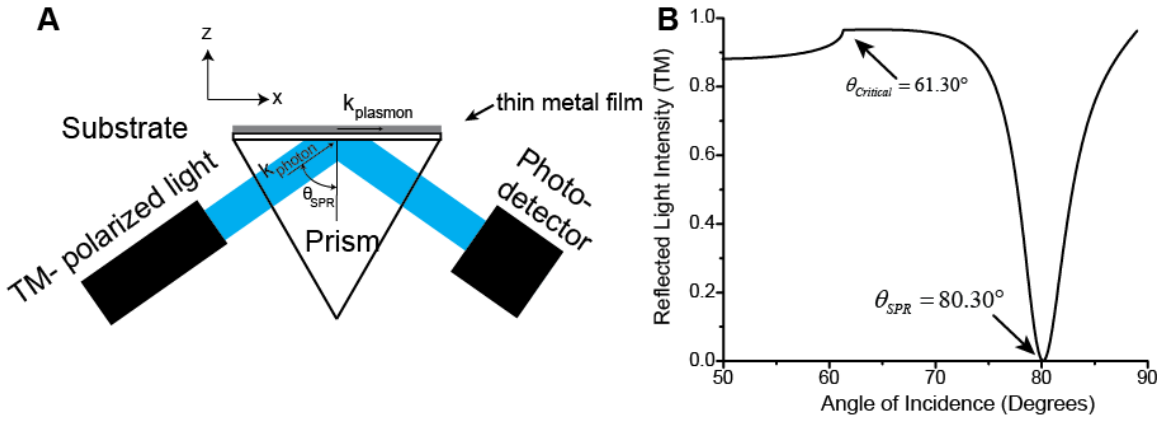

Figure 2.8: Excitation of SPR using ATR coupling technique **A** Schematic of an ATR based SPR setup. TM-polarized light is reflected at an angle superior to the critical angle from an interface between the prism and a metal layer. The reflected light intensity is recorded by a photodetector. **B** Simulated reflected light intensity as a function of the angle of incidence for a BK7/46 nm Ag/Water stack exited at 470 nm. Both, the critical angle and the coupling angle for SPR are indicated.

A schematic of the ATR coupling technique is shown in Figure 2.8A. TM- polarized light is reflected at an angle superior to the critical angle and the reflected light intensity is recorded by a photodetector. A simulation of the reflected light intensity for a BK7/46 nm Ag/Water stack as a function of the angle of incidence is shown in Figure 2.8B. When θ approaches θ_c a similar effect can be observed as in TIR and the light intensity increases reaching a maximum at θ_c. Unlike in TIR, for $\theta > \theta_c$ a sharp drop in light intensity becomes visible, reaching a minimum in intensity at θ_{SPR}. At this angle $k_{PhotonATR} = \beta'_{Plasmon}$ and critical coupling is achieved. From (0.15) together with (0.17) the critical coupling angle θ_{SPR} can be written as:

$$\theta_{SPR} = \sin^{-1}\left(\frac{1}{n_p}\sqrt{\frac{\varepsilon_M n_D^2}{\varepsilon_M + n_D^2}}\right) \tag{0.18}$$

It is important to note that θ_{SPR} is strongly dependent on the refractive index of the dielectric (n_D) above the thin metal layer. Any variation in n_D will directly translate into a variation of θ_{SPR}. Since biomolecules and cells exhibit a refractive index larger than water, SPR can be used to detect changes of biomolecular contents at the metal/dielectric interface forming the underlying principle of SPR based biosensing.

2.2.3 Surface Plasmon Resonance Biosensing

In conventional SPR, biorecognition elements (ex: antibodies, ligands, etc.) are immobilized on the metal surface. Analyte molecules in the fluid can then specifically bind to the biorecognition elements, producing an increase in refractive index at the sensing surface, thereby generating a shift in θ_{SPR}, detectable by the system.

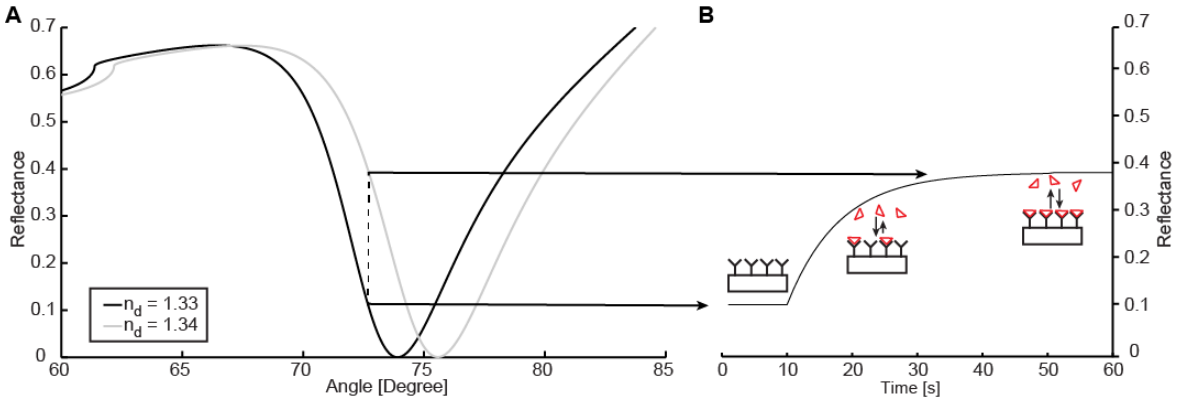

Figure 2.9: Impact of refractive index changes in close proximity to the metal surface that change coupling conditions (A). When light is incident at a fixed angle of incidence and the reflected light intensity is recorded, refractive index changes can be followed in real-time (B).

Binding events can be measured without the need for any labeling of the analyte molecules (Figure 2.9A). Moreover, by keeping the angle of incidence constant and following the reflected light intensity changes, the binding kinetics can be observed in real time (Figure 2.9B). Once equilibrium is reached, the shift in the dip of the SPR spectra can be converted into the analyte molecule concentration on the surface [Tumolo *et al.*, 2004]. SPR biosensors can be tailored for the detection of any analyte if a biomolecular recognition element is available. SPR does not require fluorescent or radioactive labels. Furthermore, unbinding of an analyte can also be observed, enabling the detection of the recovery of the sensing layer, making continuous monitoring possible. These features helped SPR to become an established method to study a broad range of bimolecular interactions such as: antibody-antigen [Fägerstam *et al.*, 1990], receptor ligand [Ward *et al.*, 1995] nucleic acid-nucleic acid [M. Yang *et al.*, 1998]and nucleic acid-protein [Fisher *et al.*, 1994] and with more than 20.000 PubMed listed publications so far.

Besides the characterization of molecular interactions, more complex biorecognition elements have been used such as, artificial cell membranes [Knoll *et al.*, 2000] and whole biological organisms such as bacteriophage [Balasubramanian *et al.*, 2007]. In drug screening or medical

diagnosis, however, single biomolecule interactions are only a small part of a complex functional process. This illustrates the necessity to shift from single biomolecule detection methods to more complex, functional biorecognition elements such as whole cells.

2.2.4Living Cell-Based Surface Plasmon Resonance Biosensing

There is an increased interest in biosensors using living cells, since such assays can be used for functional diagnostics. A cell-based biosensor (CBB) uses living cells as a biorecognition elements. External stimuli (e.g. environmental, food or blood samples) change the cellular microenvironment and trigger distinct cellular responses (Figure 2.10) [Banerjee *et al.*, 2008; Bernard *et al.*, 2014; Ziegler, 2000]. These changes in the cell can be correlated to analyte composition and are used to report for example live pathogens, active toxins or cytokines [Banerjee & Bhunia, 2009]. CBB have the advantage of providing insight into physiological effects of the analyte at different levels (organelle, cellular or tissue) [Pancrazio *et al.*, 1999].
In the past decade, different cell-based assays (CBA) have been developed to detect changes in

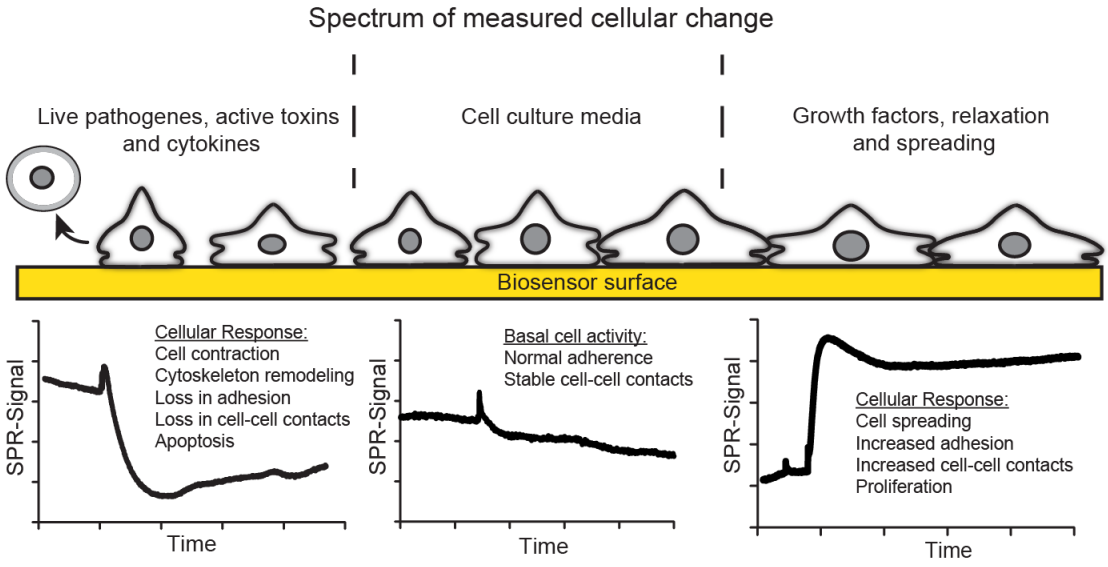

Figure 2.10: Spectrum of measurable cell responses by SPR and their impact on the SPR signal.

cellular physiology [Ziegler, 2000]. Some, for example, utilize changes in the metabolic response of cells by measuring change in oxygen or glucose consumption, while others detect the metabolic end-products such as lactic acid secreted from the cells into the media [Rawson *et al.*, 1989; Ziegler, 2000]. While such assays rely on the detection of secondary cellular

markers, rendering their response rather slow, other CBAs follow cellular responses in real-time. Conductivity assays have been used, exploiting the electrical resistance of a cell monolayer in order to measure cell-cell and cell substrate interactions [Lo *et al.*, 1993] which is presented in more details towards the end of this chapter. Other transducers such as quartz crystal microbalance (QCM) [Marx *et al.*, 2001] and field effect transistors (FET) [Sakata & Sugimoto, 2011] were also proposed.

More recently, optical based transducer techniques such as optical gratings and SPR were found to be sensitive tools to follow cellular responses in real-time, without any need for labeling with exogenous markers [Chabot *et al.*, 2009; Scott & Peters, 2010]. The high sensitivity of SPR, along with the capability for fluorescence using SPEF and the potential application for single cell imaging and endoscopic instruments make this transducer technique a valuable tool for clinical diagnosis [Yanase *et al.*, 2014]. SPR based CBA have successfully been applied for the detection of allergens [H*et al., 2002; Yanase et al.*, 2010] and to study the therapeutic effect of drugs [Kosaihira & Ona, 2008; Nishijima *et al.*, 2010]. Our group further developed multiple SPR based CBA utilizing cells for the detection of pro-apoptotic factors, toxins and hormones [Chabot *et al.*, 2009; Cuerrier *et al.*, 2008; Maltais *et al.*, 2012].

One potential limitation of SPR based CBA is the penetration depth which lies within the hundreds of nanometers range. This results in a relatively shallow sensing depth when it comes to measuring responses of living organisms such as cells and bacteria that are in the range of micrometers in size. It is therefore beneficial to achieve a deeper SPR penetration depth to maximize the molecular content within the evanescent field of the organism under study. To overcome these limitations, a “hybrid” structure between a dielectric slab waveguide and SPR, namely *metal clad waveguides,* can be used.

2.3 Metal Clad Waveguides (MCWGs)

Metal clad waveguides were first described shortly after SPR in the early 70’s [Kaminow *et al.*, 1974; Reisinger, 1973] and were initially applied as polarizers and mode filters [Suematsu *et al.*, 1972]. Besides the term MCWGs, multiple other terminologies have been used throughout the literature to describe essentially the same structures such as metal clad leaky waveguides

(MCLWs) [Mohammed Zourob *et al.*, 2003; Mohammed Zourob & Goddard, 2005], coupled plasmon-waveguide resonance (CPWR) [Salamon *et al.*, 1997; Salamon & Tollin, 2001], plasmon-waveguide resonance (PWR) sensors [Abbas *et al.*, 2011] and guided wave surface polarizations (GWSP) [Herminghaus & Leiderer, 1989]. Throughout this work, the term MCWG will be used with respect to their sensing capabilities, MCWGs have seen less attention throughout the last decades compared to SPR, and their applications focused mainly on gas sensing [Herminghaus & Leiderer, 1989; Osterfeld *et al.*, 1993; A. Otto & Sohler, 1971; Podgorsek *et al.*, 1997; Podgorsek & Franke, 1998]. More recently, MCWGs were also applied in biosensing and, due to their advantages in terms of evanescent field penetration depth, applied to larger objects such as cells and bacteria [N. Skivesen *et al.*, 2007; M Zourob *et al.*, 2005; Mohammed Zourob *et al.*, 2003].

2.3.1 Definition of Metal Clad Waveguides

A MCWG is similar to a dielectric slab waveguide with the only difference being that a thin metal layer forms the lower cladding. A schematic of a MCWG is shown in Figure 2.11. As most common metals (e.g. Ag, Au, Al, Cr and Ni) have large imaginary components of their

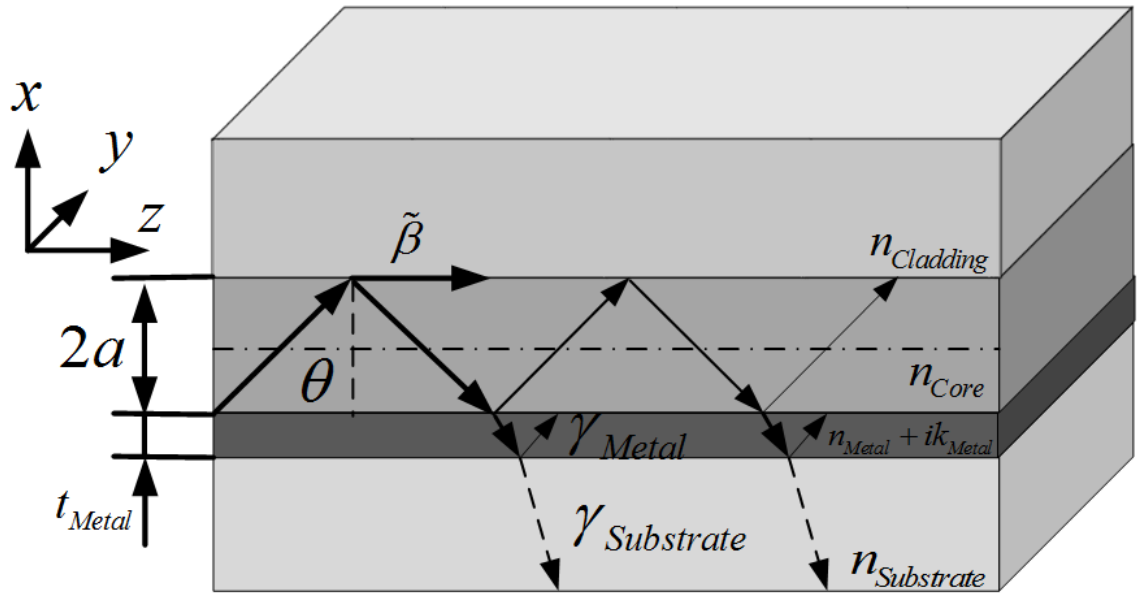

Figure 2.11: Schematic of a MCWG. The basic setup of a MCWG sensor chip is similar to that of a classical dielectric waveguide with the only difference being a thin metal layer as the substrate. Due to the complex refractive index of the metal (n_{Metal}+ik_{Metal}) absorption losses (γ_{Metal}) and radiation losses ($\gamma_{Substrate}$) render the mode lossy.

refractive index in the visible spectra [Johnson & Christy, 1972], they introduce high losses for the light propagations in such structures (γ_{Metal}, Figure 2.11). To study the propagation of waves in such structures, the same analysis as in Section 2.1.3 can be applied, just that now the complex refractive indices are used to account for the losses in the metal layer. If a high refractive index substrate is used, as it is the case with the ATR coupling technique, a small portion of the guided light back-couples into the substrate leading to additional damping losses for the guided mode ($\gamma_{Substrate}$) [Jirí Homola, 2006]. Thus, such modes are often referred to as *leaky* modes. This leads to a complex propagation constant of the mode $\tilde{\mu}$ [illegible], where β" accounts for the propagation losses (γ_{Metal} and $\gamma_{Substrate}$) of the waveguide. The same discussion of the complex propagation constant for SPR is also valid for MCWGs. Using numerical tools, one can calculate $\tilde{\mu}$ for these structures. All calculations involving the characteristics of MCWG were obtained using the FIMMWAVE (Photon Design Inc., V6.3.1 (x64)) software.

2.3.2Characteristics of MCWG Sensor Chips

MCWG based sensor chips are highly flexible in terms of their sensing characteristics and can be tailored to suit different sensing needs. Starting from the SPR structure introduced in

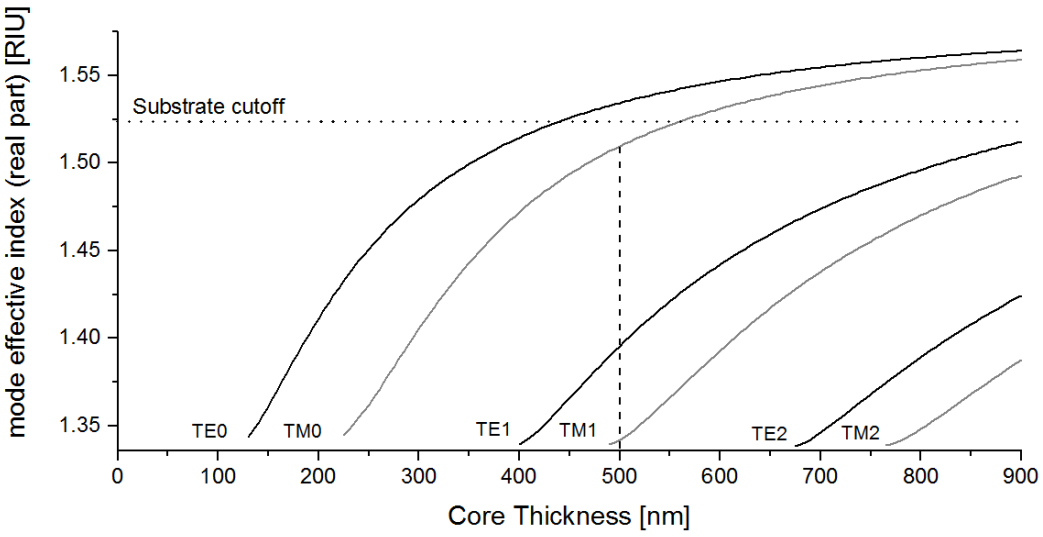

Figure 2.12: Guided modes effective index for a MCWG as a function of core thickness. Beyond a minimum dielectric core thickness (cutoff thickness), it is capable of supporting guided modes. With increasing thickness, the effective index of the guided mode also increases and more modes are supported by the structure.

Section 2.2.1, a high refractive index dielectric (e.g. photoresist KMPR) is deposited on top of the thin metal layer (t_{Ag} = 50 nm). Depending on the thickness of the dielectric core layer, an increasing number of guided modes is supported by the MCWG structure. Figure 2.12 shows the real part of the effective refractive index (n_{eff}) of each individual mode as a function of core thickness. The minimum core thickness, termed the *cutoff thickness*, (e.g. 130 nm for TE0 and 225 nm for TM0), is needed for the structure to support a single mode in TE or TM. With increasing core thickness more guided modes are supported and the structure acts as a *multimode* waveguide. Furthermore, the effective index of the modes gradually increases with increasing core thicknesses. The core thickness determines the sensing characteristics of the MCWG structure.

If, for example, a KMPR core layer of t_{KMPR} = 500 nm is selected, the MCWG supports two guided modes in TM (TM0 and TM1) and one mode in TE (TE1). Using the ATR prism coupling technique as introduced in Section 2.2.2, light can be coupled into the individual modes and Figure 2.13 shows simulated reflected light intensities for the MCWG and compares them to the SPR sensor chip introduced above. While the SPR sensor chip supports only one TM mode (θ_{SPR} = 80.30°, Figure 2.13A), two TM-modes are observed in the MCWG structure ($\theta_{MCWG,TM0}$ = 82.10° and $\theta_{MCWG,TM1}$ = 61.60°, Figure 2.13A). Further, in contrast to SPR, MCWG also support TE modes ($\theta_{MCWG,TE1}$ = 66.30°, Figure 2.13B) which can be used to provide additional insight into the optical anisotropy of samples [Salamon & Tollin, 2001].

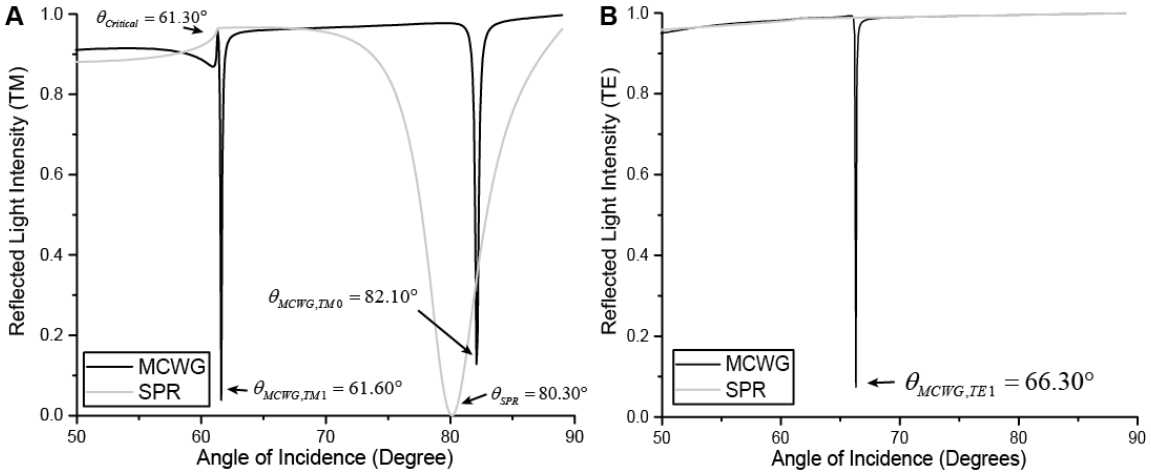

Figure 2.13: Simulated reflected light intensity for a SPR (BK7/50 nm Ag/ Water) and MCWG (BK7/50 nm Ag/500 nm KMPR/ Water) structure for TM (A) and TE (B) respectively. Only the fundamental TM mode is observed for SPR, while two TM modes and one TE mode are supported by the MCWG structure.

In terms of resolution, one striking feature when comparing the reflectance dips of SPR and MCWG is how "sharp" the MCWG dips appear. This characteristic is quantified by the full width half max (FWHM) of the dip. SPR has a $FWHM_{SPR} = 18.30°$ which is much larger compared to the MCWG modes with $FWHM_{MCWG,TM0} = 0.328°$ and $FWHM_{MCWG,TM1} = 0.145°$, respectively. Depending on the underlying detection system, the dip shape has a great impact on the sensitivity of the sensor. If the system is based on angular interrogation and reflected light intensity is the measured signal (as it is the case for the system developed during this thesis), the FWHM has a direct impact on the resolution of the system [Nina Skivesen *et al.*, 2005]. Changes in the refractive index of the dielectric cladding will ultimately change the effective refractive index of the mode, thereby shifting the dip position. If the angle of incidence is kept constant such changes directly translate to variations of the reflected light intensity. Figure 2.14 demonstrates this principle for SPR and MCWG for a small change of the cladding refractive index ($\Delta n_c = 0.001$). Such a refractive index (RI) step leads to a small change in

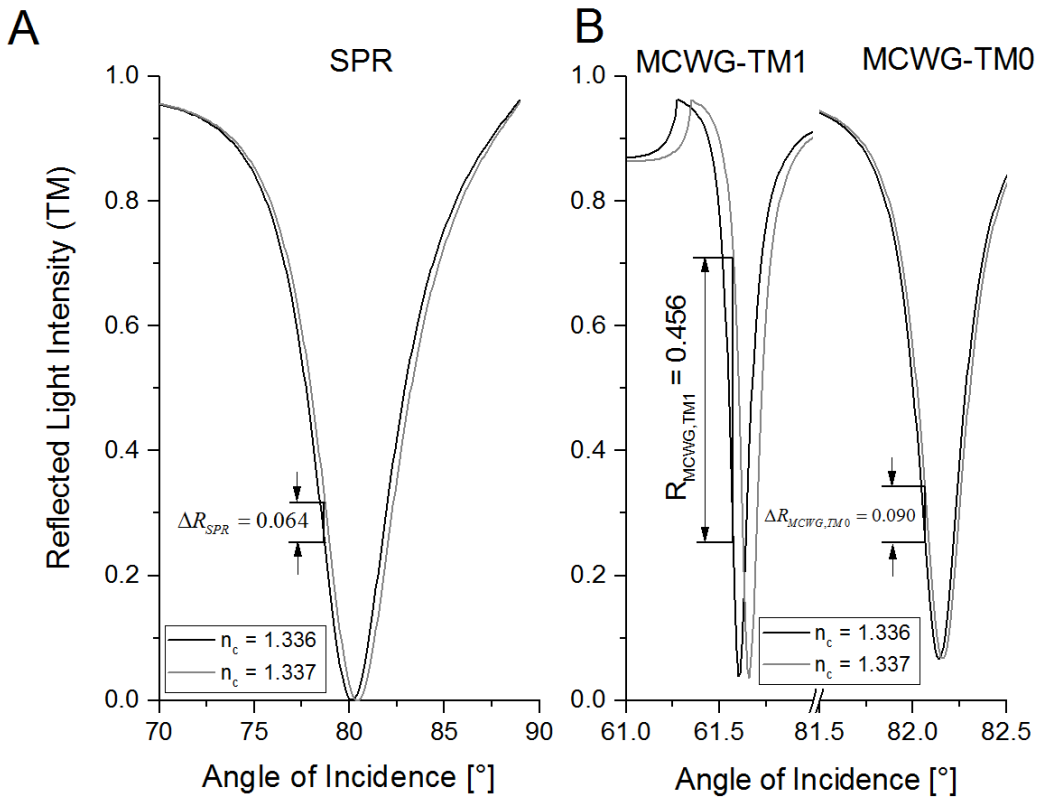

Figure 2.14: Change in reflectance for $\Delta n_c = 0.001$. A small FWHM leads to a larger increase in reflected light when the refractive index of the cladding changes and allows for an easier estimation of the dip minimum.

reflectance for SPR ($\Delta R_{SPR} = 0.064$). In MCWG it is slightly larger for the MCWG-TM0 mode ($\Delta R_{MCWG,TM0} = 0.090$) and much larger for the MCWG-TM1 mode ($\Delta R_{MCWG,TM1} = 0.456$). The difference between the MCWG-TM0 and MCWG-TM1 modes is explained by how close these modes are to their cutoff. To achieve highest sensitivity, MCWG are best operated very close to their cutoff thickness [Nina Skivesen *et al.*, 2005] and, as shown in Figure 2.14, a given change in refractive index will lead to the largest change in reflected light intensity for the MCWG-TM1 because it is closest to cutoff. In the context of imaging, this characteristic of MCWG sensors is also very interesting and will be discussed in more detail in the next section.

Another important sensing characteristic of MCWGs is the penetration depth of the electric field into the dielectric above the core layer. The penetration depth determines how deep the sensor can "sense" into the dielectric above the surface. Above this penetration depth, changes in the dielectric will only marginally impact the signal and the sensor is effectively "blind". For classic

biomolecular assays (e.g. antibody-antigen), binding events occur within tens of nanometers of the surface and, for such an application, a shallow penetration depth is beneficial to strongly confine the electric field within the binding region as it is the case in SPR (see Figure 2.7B). The sensor's sensitivity to surface events is termed *adlayer sensitivity*. In contrast, when micrometer sized objects such as bacteria and cell are of interest, RI changes may occur much further away of the sensor's surface within the cell or bacteria. In such an application, it is important to penetrate as deeply as possible into the dielectric above the surface to maximize the sensitivity into the bulk (*bulk sensitivity*). Figure 2.15 shows the electric and magnetic field profiles throughout the MCWG sensor structure. A penetration depth into the water of around 50 nm is observed for the MCWG-TM0 compared to more than 400 nm for the MCWG-TM1 mode. Again, depending on how close the mode is to its cutoff determines the penetration depth, with the deepest penetration depth achievable closest to the cutoff (MCWG-TM1).

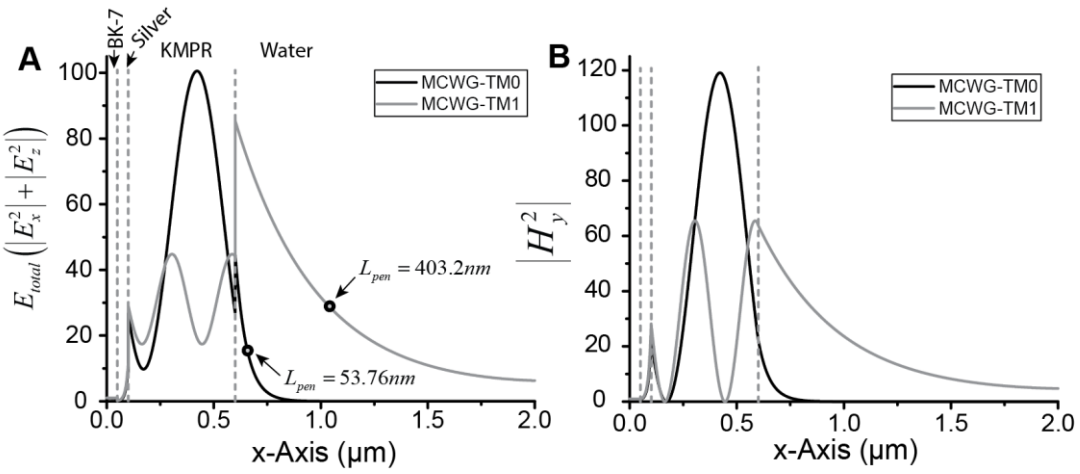

Figure 2.15: Simulated E and H-Field profiles through the MCWG structure. The field has a strongly asymmetrical shape with a larger portion of the field in the dielectric cladding compared to the metal. The closer the mode is to its cutoff, the deeper the penetration depth. Further, MCWG can be used as an additional enhancement of the electric field from the thin metal layer.

Interestingly, similar to SPR, in MCWG the field is greatly enhanced (Figure 2.15). In MCWG, however, the electric field enhancement due to the metal can further be enhanced. The field enhancement is around 30 times at the silver/KMPR interface for the MCWG-TM1 mode. These field enhancements have been utilized to excite different molecular probes and have been utilized for surface enhanced raman spectroscopy [Chen *et al.*, 1976; Nemetz & Knoll, 1996]

and surface enhanced fluorescence spectroscopy [Fort & Grésillon, 2008; Liebermann & Knoll, 2000; Yu *et al.*, 2003] with the latter being further discussed towards the end of this chapter.

Taken together, depending on the dielectric core material used and on the dielectric core thickness chosen, MCWGs can be tailored to achieve deep penetration depth, a high bulk sensitivity, and a significant electric field enhancement. When operated close to their cutoff, these capabilities make them well suited to study larger objects such as cells and bacteria.

2.3.3 Cell Based Biosensing with Metal Clad Waveguides

Initially MCWG sensors were applied to characterize artificial lipid bilayers and their improved sensitivity was demonstrated [Salamon *et al.*, 1997]. Interestingly, it was found that the use of both TM and TE modes is beneficial to characterize anisotropy and helps to reliably determine the optical parameters of complex biological samples [Salamon & Tollin, 2001]. Their capability for deep penetration depth was applied to the detection of bacteria and yeast cells [M Zourob *et al.*, 2005; Mohammed Zourob *et al.*, 2003] and a nearly threefold signal increase for these cells and a twofold increase in the corresponding fluorescence signal was observed when compared to SPR. MCWG have also been employed to study mammalian cells and their growth could reliably be followed using MCWGs operated in TM and TE modes [N. Skivesen *et al.*, 2007]. The TE mode was found to exhibit a slightly higher sensitivity compared to TM. Interestingly, more recently a study applied the concept of MCWG slightly differently and used a confluent epithelial cell monolayer as the dielectric core layer [Yashunsky *et al.*, 2012, 2013]. Since the cells themselves have a slightly higher refractive index than their surrounding media, and given they form a tightly interconnected monolayer, they were found to be capable of guiding light in the infrared. The authors demonstrate this by utilizing their technique to sense thickness variations within the monolayer and monolayer disruption due to bacteria.

Different groups demonstrated the label-free detection of cellular activity by both SPR and more recently by MCWGs. These studies provided insight into cellular activity and growth and could show the advantage of label-free evanescent field based biosensing to study large populations of living cells. Nevertheless, while cell populations are often assumed to respond homogeneously, there is growing body of evidence about phenotypic heterogeneity within cell

populations [Samadani *et al.*, 2006; Slack *et al.*, 2008]. To study such underlying heterogeneity within a cell population in a label-free modality, individual cells on top the sensor's surface must be resolved. Evanescent field based technologies have the advantage that they inherently support imaging. Thus, it is possible to utilize SPR and MCWG based sensors to study individual cells, a technique called *evanescent wave microscopy*.

2.4 Evanescent Wave Microscopy

If the photodetectors in the ATR coupling technique are cameras, and imaging optics are installed in the reflected light path, the 2D light intensity distribution of the coupled light can be determined. This allows one to spatially resolve the refractive index distribution at the sensor's surface. Depending on the underlying sensor's principle, this technique is termed *surface plasmon resonance imaging* (SPRI) or *metal clad waveguide imaging* (MCWGI). Different concepts have been proposed to achieve high resolution imaging of nanoparticles and biological samples or large field of view (FOV) for high throughput multiplexing. These concepts will now be introduced and discussed in terms of their resolution and imaging capabilities.

2.4.1 Principle and Concepts

The effective index of the guided mode and its wavevector will depend on the refractive index of the cladding. Thus, spatial variations in the cladding index (e.g. by biological media) will cause a corresponding spatial variation in the mode wavevector, which in turn will result in spatial variation of coupling conditions and reflected light intensity measured by the camera (Figure 2.16A). Figure 2.16B shows simulated reflected light intensities for the different regions (Water and PDMS). At a given angle of incidence (e.g. $\theta_{TM0/Water} = 82.1°$) critical coupling is achieved for water and the reflected light intensity drops in the regions where water is present on the sensor's surface (Figure 2.16B, black trace) and the image would appear dark in these regions. The reflected light intensity for regions with PDMS on the other hand does not show a drop in the reflected light intensity at this angle of incidence (Figure 2.16B, grey trace) because the incident light is not coupled to the mode and the image would appear bright in these regions.

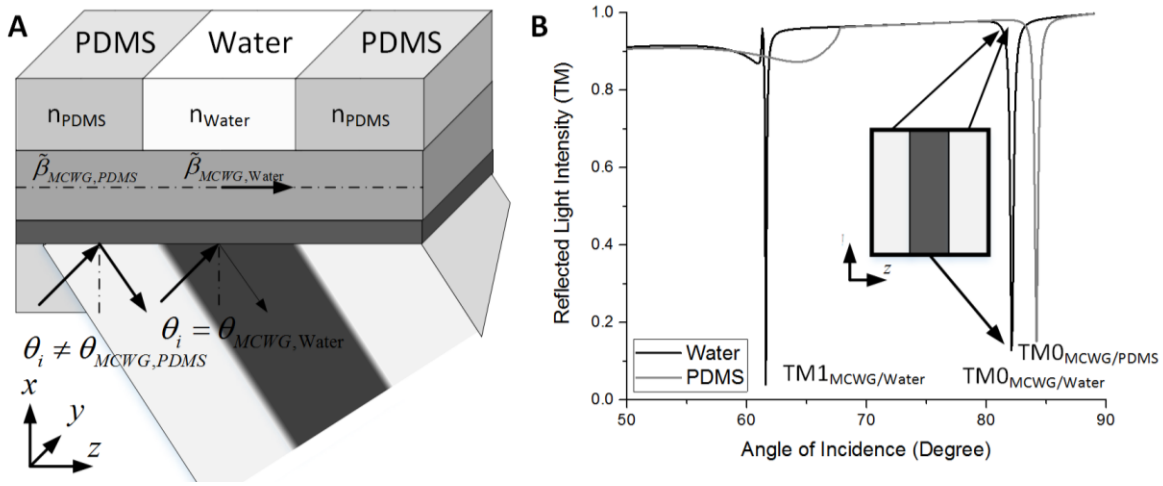

Figure 2.16: Principle of evanescent based microscopes A) Depending on the refractive index on top of the MCWG structure the guided mode changes. At a fixed angle of incidence, one is able to couple into either the mode in the MCWG/PDMS or the MCWG/Water structure which will appear as dark areas compared to uncoupled regions. B) Simulated reflectance curves for the MCWG/PDMS (grey) and MCWG/Water (black trace) as a function of the angle of incidence.

If the angle of incidence is increased, coupling in the PDMS regions would be achieved ($\theta_{TM0/PMDS}$ = 84.2°) and the pixel grayscale levels contrast would be reversed.

In order to resolve the spatial distribution of the reflected light, two main concepts have been demonstrated. The simplest form of an imaging setup can be achieved by using a CCD camera and was initially proposed by Rothenhäusler and Knoll in 1988 [Rothenhäusler & Knoll, 1988]. A schematic of such a system is shown in Figure 2.17A. A collimated light beam is coupled by a prism into the sensor structure. The reflected light beam is then focused through a long

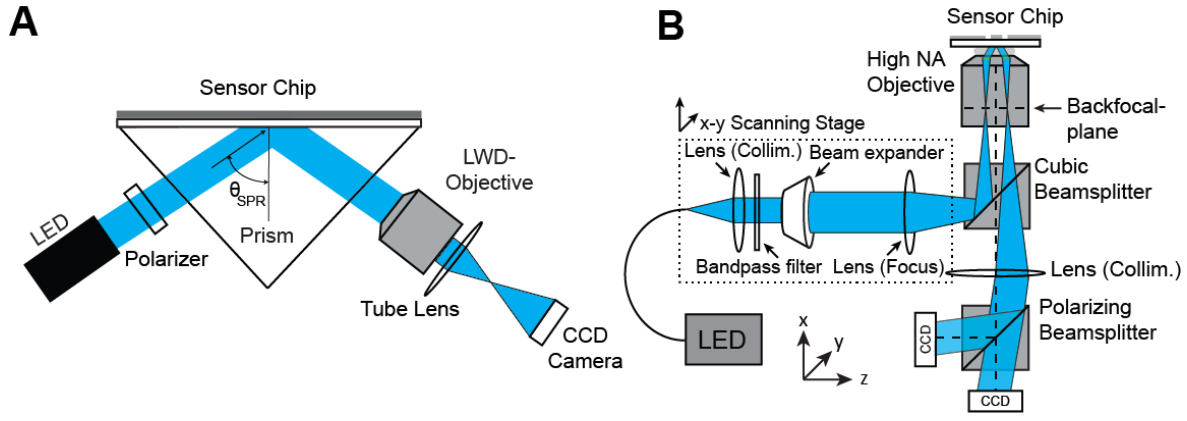

Figure 2.17: Imaging setups of evanescent based microscopes A) Prism based evanescent microscopy with a CCD camera. B) Evanescent wave microscopy based on a high numerical aperture objective as realized during this thesis.

working distance (LWD) objective or simply by a lens onto a CCD camera. The main advantage of this type of setup is the large field of view (FOV) and areas in the centimeter range can be imaged [Laplatine *et al.*, 2014]. This allowed prism based imaging systems to become a powerful tool to measure biomolecular binding event of DNA or proteins in the large microarray formats, following in parallel the kinetics of thousands of binding events in real-time and in a label-free fashion [Smith & Corn, 2003].

While large FOV are achievable using prism based imaging systems, the prism also constrains the imaging optics to low numerical aperture (NA) optics and magnification, along with optical distortions, thereby effectively limiting the maximum achievable spatial resolution [Laplatine *et al.*, 2014]. To overcome these constraints, Huang & Zare proposed the use of a high NA microscope objective as with TIRF microscopy [B. Huang *et al.*, 2007]. Briefly, light is focused at the backfocal plane of the high NA microscope objective and the offset of the light beam from the objective's central axis determines the angle of incidence of the excitation light at the sensor's surface (Figure 2.17B). The reflected light is then collected back through the same objective and visualized by a CCD camera. While the underlying coupling technique remains that of an ATR, the collection of the reflected light through the same lens allows for very low distortion imaging, potentially at a submicron resolution [B. Huang *et al.*, 2007]. Due to these advantages, such a system was realized in this thesis and is presented to a greater extend in the following chapter.

2.4.2Lateral Resolution and Penetration Depth

In evanescent field based microscopy, spatial variations in the guided mode properties are used to map the 2D refractive index distribution at the sensor's surface. After an abrupt change in refractive index and corresponding step change in coupling conditions, the reflected light requires a finite distance along the direction of mode propagation to reach a steady state in an exponential profile. The distance over which the light power decays to 1/e of the value at the step change is termed the *propagation distance* or *attenuation length*. This has been theoretically described by E. Yeatman for a plasmonics waveguide [Yeatman, 1996] and can also be applied to MCWG.

Figure 2.18 shows the simulated reflected light intensity profile for the MCWG sensor chip for a PDMS microchannel (d = 200 µm) when light is coupled into the TM0-Water mode of the MCWG. This structure has two refractive index steps, namely PDMS/Water and Water/PDMS which leads to a sudden change in the wave vector from non-coupled/coupled to coupled/non-coupled, respectively. As can be seen for the step at z = 0 µm (PDMS/Water), the field does not immediately equilibrate but rather shows an exponential decay until critical coupling is achieved and the reflected light intensity approaches its minimum value. Interestingly, on the other side of the microchannel (z = 200 µm, Water/PDMS) an overshoot is observed leading to an oscillation in the signal. Such "fringes" have first been reported experimentally by Rothenhäusler & Knoll shortly after the introduction of the first SPRI setup [Rothenhäusler & Knoll, 1988]. Depending on the wavelengths used, these fringes are either quickly damped for shorter wavelength (as shown in Figure 2.18 for λ = 470 nm) or can last several hundreds of microns for longer wavelengths (λ > 800 nm) and the damping is strongly dependent on the complex part of the mode propagation constant [Rothenhäusler & Knoll, 1988]. Ultimately, this effect has an important impact for imaging and will induce artifacts in the images, effectively

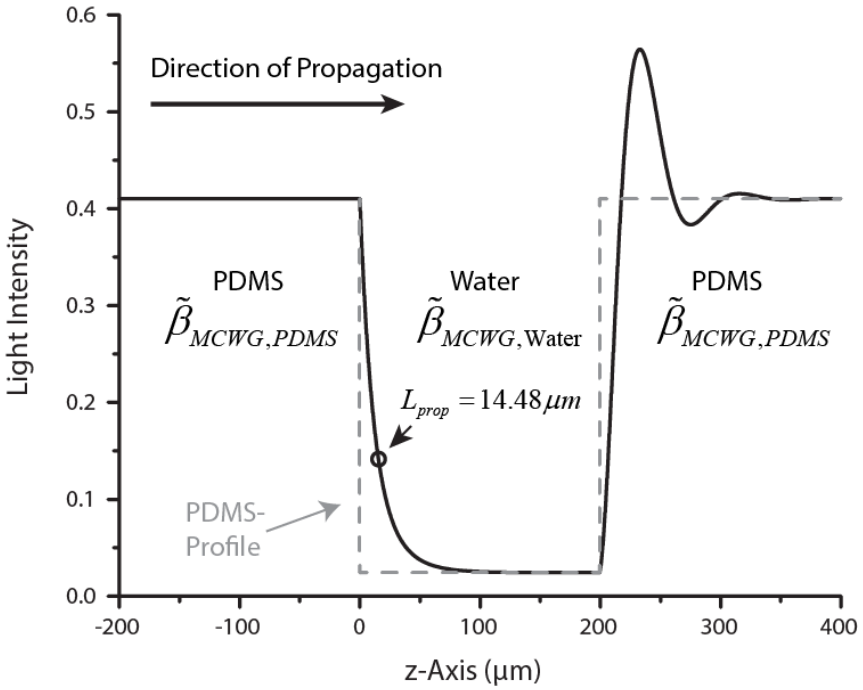

Figure 2.18: Impact of the finite propagation distance in evanescent based microscopy. Simulated reflected light intensity profile of a PDMS/Water/PDMS step on a MCWG sensor chip (BK7/3 nm Ni/23 nm Ag/5 nm Au/500 nm KMPR, TM0-Water, λ = 470 nm) based on the Yeatman model [Yeatman, 1996].

leading to blurring along the direction of propagation, limiting the maximal achievable resolution along that axis. It is therefore of great interest to study and optimize the MCWG sensor chip structure to achieve deep penetration depth while keeping the propagation distance at a minimum.

To optimize the MCWG structure, and compare against SPR, the penetration depth and attenuation distance for different dielectric thicknesses and wavelengths is calculated (Figure 2.19). In SPR, the penetration depth for Au and Ag metal films at a metal/water interface are shown on the bottom left for increasing wavelength with each marker indicating a wavelength step of $\Delta\lambda = 50$ nm. While very short attenuation distances are possible in SPR, as expected the penetration depth in these sensor structures is also very shallow. If the excitation wavelength is increased to $\lambda \geq 800$ nm penetration depths around 400 nm are possible but the attenuation distance quickly increases well beyond 10 μm limiting the usability for imaging applications. Further, most CCD chips rapidly drop in sensitivity around such long wavelengths.

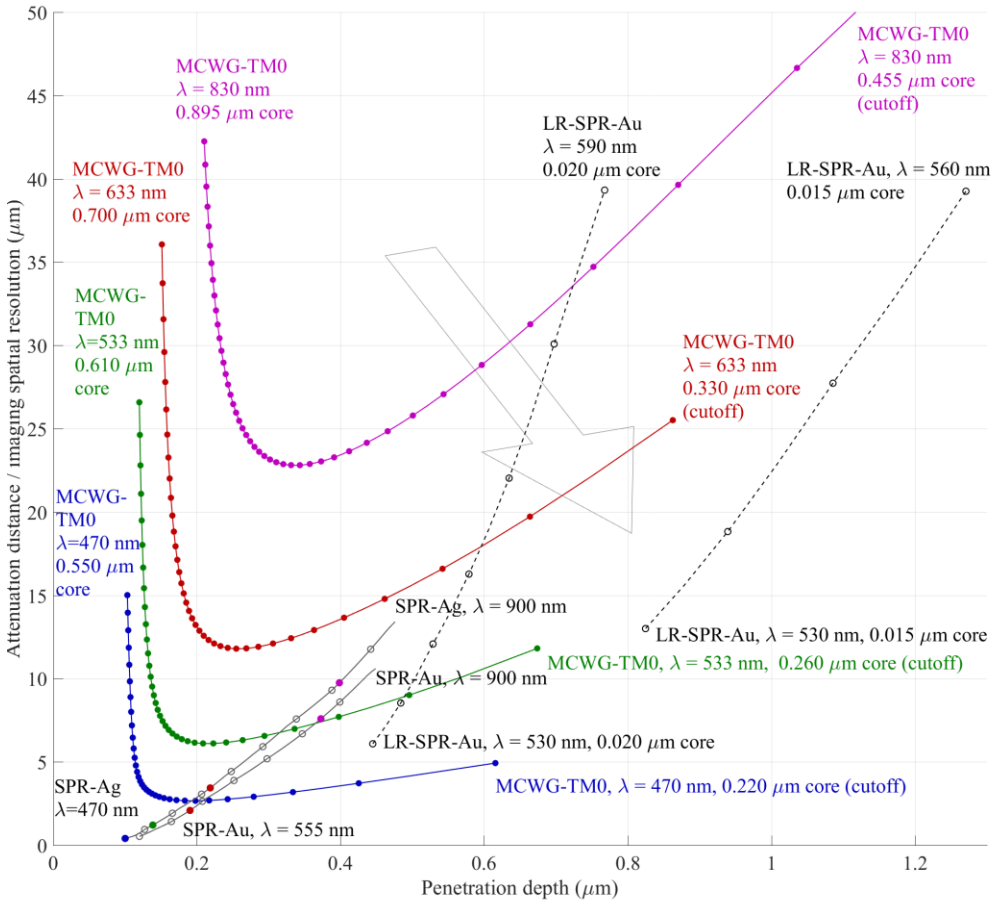

Figure 2.19: Tradeoff between penetration depth and attenuation length for MCWG, SPR and long range (LR) -SPR. Arrow indicates the better tradeoff (high-penetration and low attenuation). Wavelength range was limited to 850 nm since quantum efficiency for CCD-camera begins to be very low for such wavelength. There is an intrinsic tradeoff between the achievable penetration depth and the maximal achievable resolution. Reprint with permission from [Söllradl *et al.*, 2017]

In MCWG on the other hand, besides longer wavelengths, the dielectric core thickness is another parameter that can be used to tune the penetration depth. The penetration depths and attenuation distance for increasing dielectric core thicknesses starting at the cutoff thickness (right side of the traces) and steadily increasing towards the left ($\Delta d = 10$ nm, each marker) were calculated for different wavelengths for the fundamental MCWG TM0 mode (Figure 2.19). As with SPR, a tradeoff exists between the penetration depth and the attenuation distance. This tradeoff is, however, less severe. When approaching the cutoff thickness, much deeper penetration depths ($L_{pen} > 400$ nm) are achievable while keeping the attenuation distance well below 10 µm, when operating the sensor at shorter wavelengths ($\lambda = 470$ nm). As with SPR, at longer excitation wavelengths the penetration depth can be increased further with higher attenuation distances

well beyond 10 µm. Thus, when MCWG are operated with a dielectric core thickness close to the mode's cutoff, they offer a better tradeoff in terms of penetration depth and attenuation distance compared to SPR. This makes them a sensor structure that is well suited to study larger objects that are in the micrometer size range such as individual cells and bacteria.

2.4.3 Surface Plasmon Resonance Microscopy of Living Cells

Several studies have applied SPRI to living and fixed cells. The first system was a prism based system used to study the interaction of cells with their substrate in 1999 [Giebel *et al.*, 1999]. Figure 2.20 shows the visualization of the basal portion of the cells by which they establish contact with the substrate (focal adhesion sites and the lamellipodia, a structure that is formed by the cell to move along the surface). Due to the shallow penetration depth, a large portion of the cell body was effectively invisible with this SPRI setup. More recently, another group also used a SPRI prism-based systems to visualize cell attachment on the sensor's surface [Peterson *et al.*, 2009]. Due to the high adlayer sensitivity of SPR, they could quantify the deposition of proteins from the cell onto their surroundings. While these studies mainly focused on the structural aspects of cellular attachment, a prism based system was also applied to detect cellular activity by following refractive index changes within living mast cells when exposed to different specific and non-specific stimuli [Yanase *et al.*, 2010]. The authors could successfully study

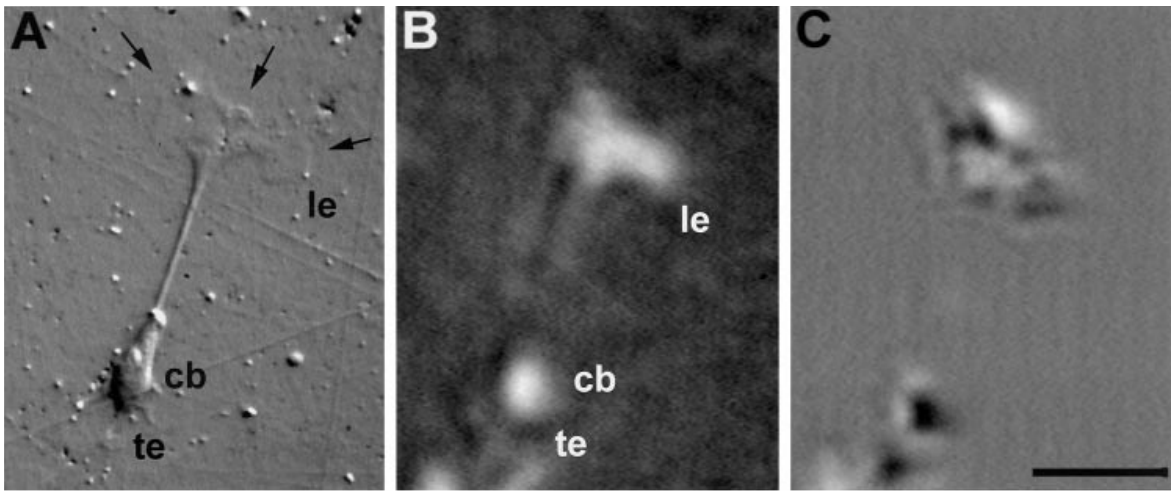

Figure 2.20: Surface plasmon microscopy of a goldfish glial cell. A: Brightfield image of the cell. B: SPRI image of the same cell showing the lamellopodium structure that is directly in contact with the substrate. C: Differential image illustrating the movement of the cell within two minutes. Scale bar is 100 µm. Reprint from [Giebel *et al.*, 1999].

morphological changes as well as changes of the refractive index within the basal portion of the cell upon stimulation.

The lateral resolution in these studies was, however, limited by the propagation distance and only larger cell types of sizes within the hundreds of microns were studied. In order to diminish the impact of the propagation on the images, one group used a different approach by maximizing the imaginary part of the complex propagation constant [S.-H. Kim *et al.*, 2011]. Gold becomes highly absorbing at shorter wavelengths ($\lambda < 600$ nm) and the authors could obtain high resolution images using a combination of a thin gold layer and an excitation at $\lambda = 532$ nm (Figure 2.21). The use of gold at such low wavelengths, however, greatly diminishes the system's sensitivity and achievable image contrast [Moreau *et al.*, 2014]. To overcome these issues and enhance the image contrast, a nulling ellipsometry setup was integrated into the light path to remove the background illumination that does not couple into/out of the plasmonic mode. Such a system proved extremely efficient in resolving cellular structures at the sensor's interface and diffraction limited resolution is possible in both axes. In this case, however, the prism and the long working distance low NA optics become the limiting factor in terms of imaging resolution as well as the low sensitivity due to the high losses in the gold film at such short wavelengths.

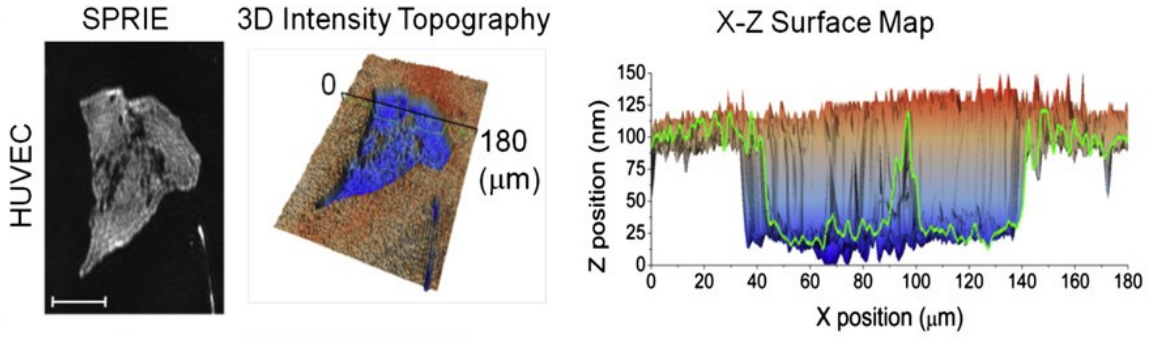

Figure 2.21: Cell-substrate interface imaged by SPRI ellipsometry. Using a gold substrate and short wavelengths the imaginary part of the complex propagation constant can be maximized and high-resolution imaging are possible. Reprint from [S.-H. Kim *et al.*, 2011].

To overcome these issues, high NA microscope objective based systems have been applied to visualize cellular structures and activity. In order to overcome the finite propagation distance

and achieve submicron resolution, a technique called wide field surface plasmon microscopy, initially demonstrated by Kano & Knoll in 2000 [Kano & Knoll, 2000] and later further developed by Stabler & See [Stabler *et al.*, 2004] was applied to cells [Jamil *et al.*, 2008]. By simultaneously injecting light into the back focal plane of a high numerical objective at two opposed positions, surface plasmons are excited with opposing propagation directions. Destructive interference results in a localized surface plasmon excited on the surface [Kano & Knoll, 2000]. This technique can then be used to pointwise scan the refractive index at the sensor's surface and a 2D image is reconstructed afterwards. Figure 2.22 shows high resolution images of the lamellopodia of a migrating cell as observed by Jamil *et al.*. This technique has the advantage of sub-micron resolution but imposes a severe time constraint (≈ 5 min/image) by the pointwise scanning of the surface, limiting its use to study dynamic events.

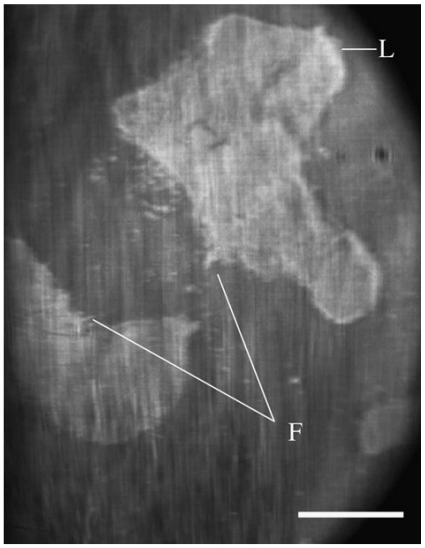

Figure 2.22: Wide field SPRI of HaCaT cells. This technique allows for high resolution imaging of the lamellopodia (L) and fillapodia (F) of the cell. Scale bar is 20 μm. Reprint from [Jamil *et al.*, 2008]

To follow cellular dynamics, high NA objective based systems have also been applied by N. Tao to study cell/substrate interactions. These studies could successfully identify individual cells on the sensor surface even at propagation distance limited resolution, and demonstrate, for example, the effect of osmotic stress on the adhesion of neuroblastoma cells [Wang *et al.*, 2012]. When combined with a epifluorescence microscope, the binding of certain membrane proteins could be visualized and changes within the cell/substrate contact of epithelial cells were

followed using SPRI [Wang *et al.*, 2012]. Further, the same group expanded the capability of their system by combining electrical impedance and SPRI and could follow the apoptosis and electroporation of individual human cervical cells [Wang *et al.*, 2011].

These studies demonstrate the suitability of SPRI to study structural as well as cellular dynamics down to the single cell level and different concepts have been proposed for high resolution or fast acquisition of cell/substrate interactions. Given the advantages of deep penetration depths at small propagation distances offered by MCWG, one could expect a MCWG based imaging system to be well suited to study individual cell activity within a cell population. To the best of my knowledge, their capabilities for visualization of single cell activity have not yet been demonstrated.

2.5 Other Label Free Cell Based Biosensors

In addition to SPR and MCWG, two other label-free transducer techniques have been demonstrated and extensively applied for cell based biosensing in the past decades, namely refractive waveguide grating (RWG) and electrical cell impedance sensing (ECIS). Both techniques have been commercialized (Corning Epic for RWG and ECIS by Applied Biophysics Inc.) and are now routinely applied to follow and quantify a wide spectrum of cell responses from G-protein coupled receptor (GPCR) signaling to endothelial cell monolayer integrity [Fang, 2011; Scott & Peters, 2010]. In the following, the basic concept for both RWG and ECIS will be presented and different aspects of each technique will be discussed, followed by a short overview of different applications with living cells.

2.5.1 Refractive Waveguide Grating (RWG)

The underlying principle of a RWG system is, similar to MCWG, a guided mode within a dielectric waveguide with an evanescent field penetrating into the top dialectic layer above the sensor chip. Instead of a high refractive index prism, a grating coupler is used to tune the incident's light wave vector and couple into the guided mode (Figure 2.23). The use of a grating coupler instead of a prism simplifies the coupling optics and these substrates are easy to fabricate on an industrial scale.

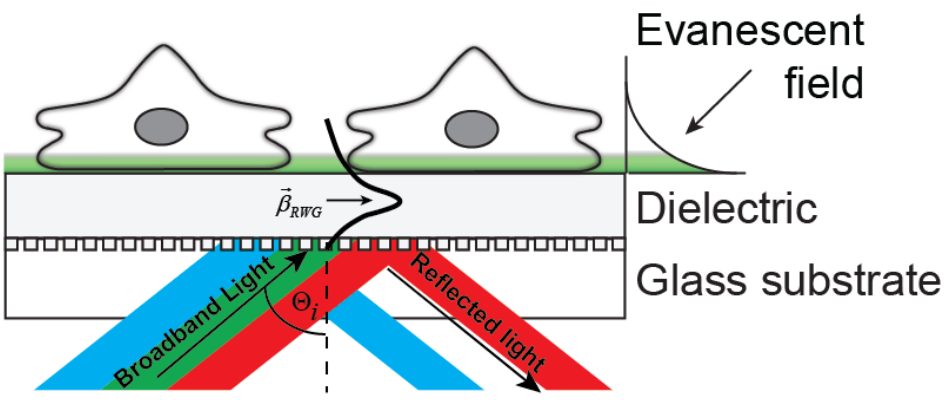

Figure 2.23:Basic principle of refractive waveguide grating (RWG). Polychromatic light is coupled via a grating coupler into the waveguide at a fixed angle of incidence. At one wavelength, the coupling conditions are fulfilled and light is guided along the waveguide. An intensity dip is observed at the coupling wavelength in the reflected light, quantified by a photo spectrometer.

The RWG system initially proposed consisted of an angular interrogation setup [Fang *et al.*, 2006] similar to the prism based systems introduced in Section 2.2.2. At a given excitation wavelength, grating periodicity, and angle of incidence, coupling conditions are fulfilled and the incident light can couple into the waveguide and a dip is observed in the reflected light intensity. Since angular interrogation requires a well-controlled movement of the underlying optical path, however, this optical setup is somewhat limited for fast readout in the high throughput format and more recently this system has been adapted and wavelength interrogation is now used [Fang, 2015; Schröder *et al.*, 2010]. By using a fixed angle of incidence, a shift in the resonant wavelength can be observed in the reflected light. This allowed a great enhancement in terms of readout time and high throughput (up to 1536-wells are now feasible) [Fang, 2015].

As with MCWG, RWG rely on an evanescent field for sensing thus the discussions from the earlier sections are also valid for sensing. Commonly, light around $\lambda = 830$ nm is used in RWG setups and the penetration depth in such a system is similar to SPR [Fang *et al.*, 2006]. Modes in RWG are also leaky modes with leakage towards the substrate of the waveguide due to the outcoupling via the grating. These losses are, however, much lower compared to the absorption losses in the metal layer of a MCWG or SPR leading to much longer propagation lengths in

these systems and a poor lateral resolution. As a consequence, instead of individual cells, only the responses of cell clusters can be studied using an RWG based imaging setup [Ferrie *et al.*, 2010, 2012].

Despite this limitation, and in particular due to its high throughput capability, RWG cell based biosensors have extensively been applied to study GPCR signaling in living cells [Fang *et al.*, 2007] and RWG could successfully identify the activation of certain families of GPCR and follow their kinetics in a dose-dependent manner [Fang *et al.*, 2007; Schröder *et al.*, 2010]. As expected, temporal signal profiles are also very similar to what our group could show with an SPR cell based assay [Cuerrier *et al.*, 2008].

2.5.2Electric Cell-Substrate Impedance Sensing (ECIS)

In addition to these optical transducer techniques, different electrical transducers have been proposed [Q. Liu *et al.*, 2014], with one of the most widely applied technique for cells being ECIS. ECIS was introduced in 1992 and was initially proposed as a tool to follow barrier function in a confluent endothelial monolayer [Tiruppathi *et al.*, 1992] and has been

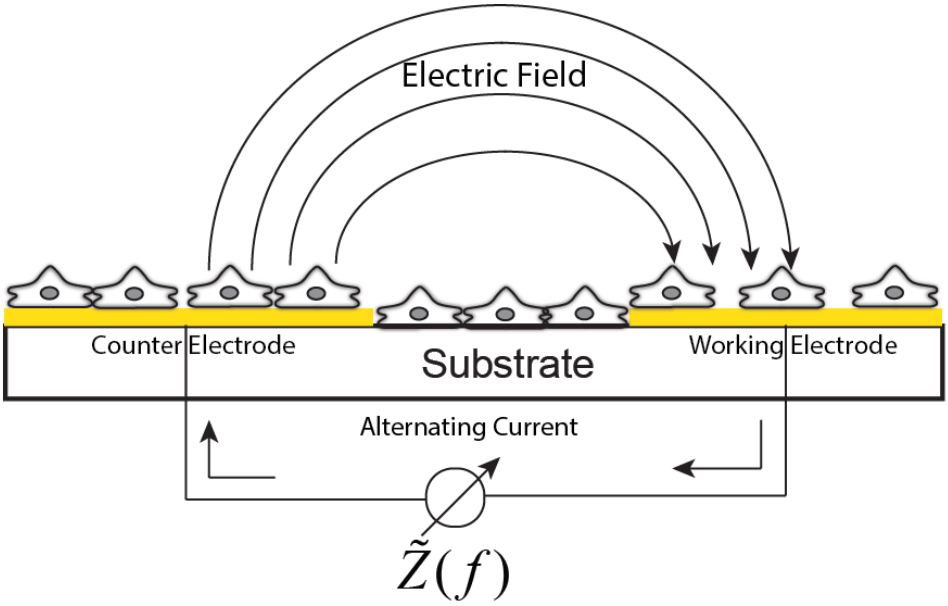

Figure 2.24:Schematic of a ECIS setup. Cells are cultured on top of planar gold electrodes and pose a resistance to an alternating high frequency (100 Hz – 100 kHz) voltage. The complex frequency dependent impedance $\tilde{Z}(f)$ is measured. Depending on the cell shape, density and cell/substrate adhesion, impedance changes.

commercialized by Applied Biophysics and other companies. A schematic of the underlying sensor design is shown in Figure 2.24. The sensor chip consists of two planar electrodes and a high frequency voltage is applied between them. When cells are cultured on top of the electrodes, the cell layer increases the electrical impedance between the electrodes, as quantified by the complex, frequency dependent impedance $\tilde{Z}(\omega)$ [Stolwijk *et al.*, 2015]:

$$\tilde{Z}(\omega) = R + iZ'' \text{ with } R = Z' \text{ and } C = \frac{1}{i\omega Z''} \tag{0.19}$$

where R is the resistance, C the capacitance and ω the angular frequency, where $\tilde{Z}$ is dependent on different properties of the cell layer. Low frequency impedance (< 4 kHz) is more sensitive to spaces in between the cells and the barrier function (permeability) is quantified. For higher frequencies (> 40 kHz), the sensor's signal is more sensitive to overall electrode coverage and can be used to quantify cell growth [Stolwijk *et al.*, 2015]. Initial works using ECIS were mostly focused on the quantification of endothelial and epithelial barrier functions. The fluorescence-based assays used for such permeability studies are based on the quantification of the transmembrane flux of a fluorescence dye through a cell monolayer cultured on top of a porous membrane [Wegener & Seebach, 2014]. ECIS, to some extent, mimics the same concept by

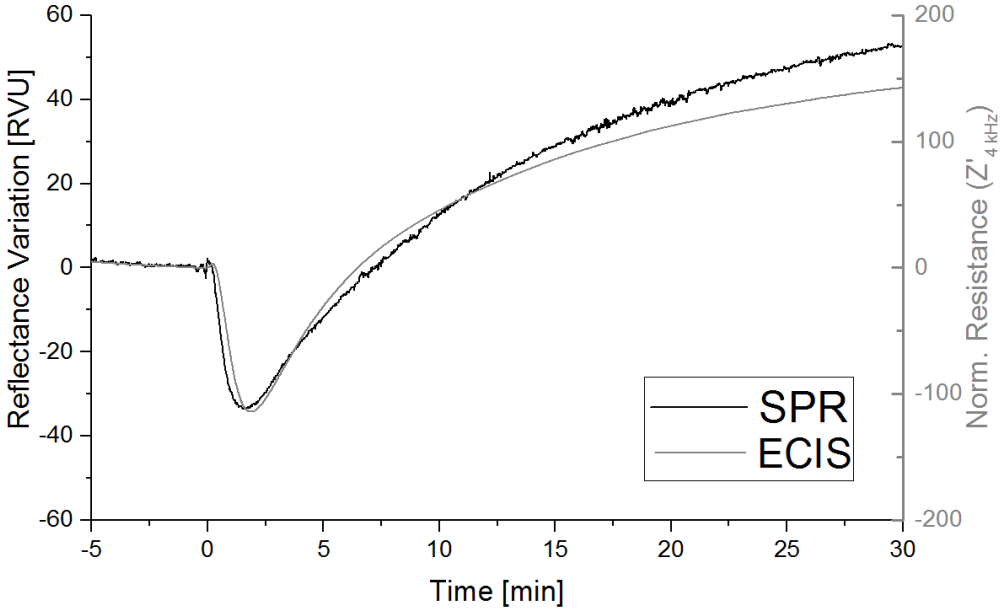

Figure 2.25: Experimental comparison of ECIS to SPR cell based assays done throughout this work. Human embryonic kidney 293 cells stably expressing the GPCR angiotensin 1 receptor stimulated with 100 nM Angiotensin II measured both by our custom build SPR system and ECIS from Applied Biophysics.

measuring the flow of charges across the monolayer with the advantage that it can greatly enhance the time resolution and the throughput and is now widely applied to study the effects of toxins and hormones on the barrier function of various cell types [Stolwijk *et al.*, 2015; Wegener & Seebach, 2014]. More recently, ECIS was also applied to study GPCR signaling, similarly to RWG and SPR [Stolwijk *et al.*, 2015]. Interestingly, despite the different sensing modalities (electric impedance instead of evanescent field), measured sensograms are very similar. Figure 2.25 shows the population response of confluent HEK-293 cells stably expressing the angiotensin 1 receptor (AT1R) activated by 100 nM Angiotensin II, measured by SPR and ECIS. There is a striking correlation between the trace profiles for both systems. An initial signal drop, associated with increased mechanical activity, is followed by a gradual increase in the signal indicating a spreading of the cells. The experimental details and the underlying (individual) cellular events leading to this signal are presented in much greater details in Chapter 4, with the focus here given on the similarity of the two signals. A group (Rudolf Robelek) combined both techniques for simultaneous assessment the cell response [Michaelis *et al.*, 2013]. They also reported a strong correlation between the two signals for the disruption of a confluent cell layer by toxins.

The ECIS signal represents an averaged signal from a large population of cells (2000 – 4000 cells) cultured on top of millimeter-sized electrodes. Attempts to shrink the electrodes could lower the number of cells contributing to the signal to approximately 50 – 100 cells and these electrodes where used to study the micro motion of cell clusters [Giaever & Keese, 1991]. Further shrinkage of the electrodes is, however, not practical due to parasitic impedance contributions arising from within the measuring equipment thereby preventing single cell resolution [Stolwijk *et al.*, 2015]. Attempts to obtain higher spatial resolution using impedance based sensing were done by mechanically scanning a microelectrode across a sample [Ballesteros Katemann *et al.*, 2002; Ervin *et al.*, 2005]. In this approach, however, the impedance of the microelectrode complicates the data interpretation [Ervin *et al.*, 2005] and the mechanical scanning is very time consuming, thus limiting the achievable temporal resolution of such an approach. To overcome these limitations and to achieve single cell resolution with impedance, a hybrid system composed of an objective based SPRI system simultaneously using the thin gold film for plasmon excitation and the working electrode for the impedance

measurement was built [Wang *et al.*, 2011]. The authors used the local perturbation of the electric field by SPR excitation and could successfully detect localized changes in the measured impedance. As expected, they also found a striking correlation between the two signals during single cell electroporation.

Both optical and non-optical label-free cell-based biosensing techniques have been successfully applied to study the impact of toxins, hormones and drugs on cell populations, cell clusters and down to a single cell level [Fang, 2011]. Among these techniques, MCWG was shown to exhibit the best tradeoff in terms of penetration depth and lateral resolution. While highly sensitive to cellular activity, the sensor's signal in all these label-free systems results from a complex cascade of molecular events within the cell and delineating the cellular events so that underlying structures contributing to the signal can be challenging. To overcome these challenges, evanescent field based technologies offer the possibility to excite fluorophores within the evanescent field, a technique called surface enhanced fluorescence. This opens the possibility to combine these two sensing modalities, namely MCWG imaging and surface enhance fluorescence imaging, with spatial resolution down to the single cell level to obtain complementary signals about intracellular signaling and the underlying structural components contributing to the sensor's signal.

2.6 Surface Plasmon Enhanced Fluorescence (SPEF)

Fluorescence is a luminescent phenomenon in which a fluorophore absorbs a photon of a certain energy and subsequently emits a photon of equal or lower energy. Fluorescence is, in its basic concept, a three-stage process and can be described by the Jablonski diagram (Figure 2.26A) [Lakowicz, 2006]. The first stage is the absorption of a photon of energy $h\nu_{ex}$ by the fluorophore, creating an excited singlet electronic state (S_1'). During the following stage, internal conversion take place within the fluorophore leading to a partial energy dissipation and yield a relaxed singlet excited state (S_1). In the final stage, a photon of energy $h\nu_{em}$ can be emitted (radiative decay channel, Figure 2.26A #3) or no photon is emitted due to collisional quenching (non-radiative decay channel, Figure 2.26A #4) and the fluorophore returns to its ground state S_0 and the whole process can be repeated. The ratio of the probability between radiative and non-radiative decay is referred to as the *quantum yield* and is, for commonly used organic

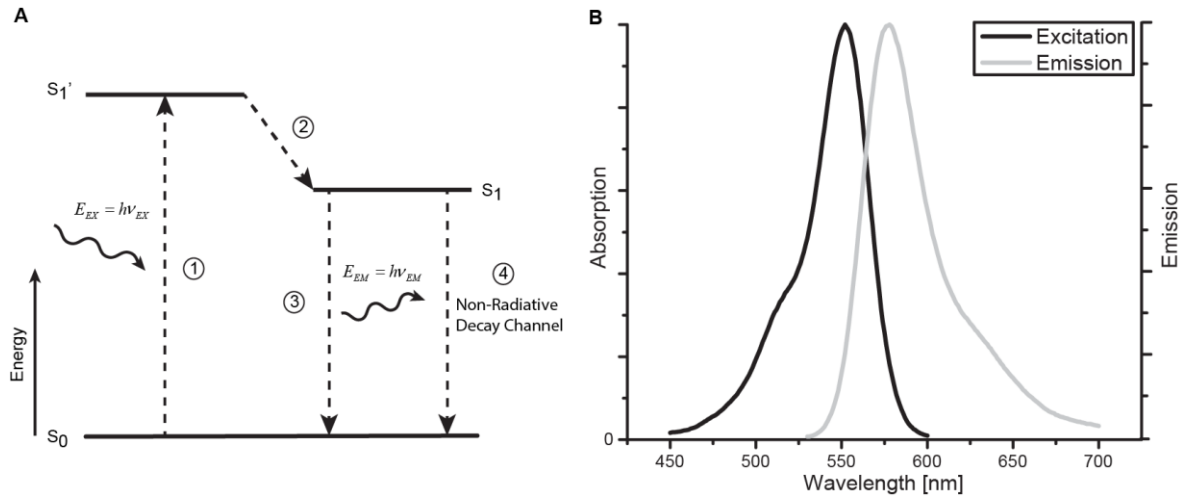

Figure 2.26: Basic Jablonski Diagram (A) and excitation and emission spectra for TRITC (B). (excitation and emission data from *life technologies*).

fluorophores, in the range of 0.5 – 0.9 [Dostálek & Knoll, 2008]. Different other mechanisms can take place such as a direct emission ($h\nu_{ex} = h\nu_{em}$) or intersystem crossings into relatively long lasting excited triplet states, a mechanism that is exploited in super resolution microscopy [Gustafsson, 2005].

Due to partial energy dissipation during the second stage, the emitted photon has a lower energy compared to the initially absorbed one ($h\nu_{ex} > h\nu_{em}$), which is known as the Stokes shift. This shift is fundamental, since it allows the instrumentation to discriminate between the photons emitted from the fluorophore from that of the light source using a bandpass filter. Each fluorophore has its specific excitation/emission spectra and Figure 2.26B shows an example of such a spectra for Tetramethylrhodamine (TRITC).

Fluorophores can also be excited using an evanescent field, allowing the selective excitation of fluorophores in close proximity to the surface and resulting in very low background fluorescence [Axelrod, 1981]. This technique has found numerous applications in biochemistry and cell biology and is known as total internal reflection fluorescence (TIRF) microscopy [Axelrod, 2001].

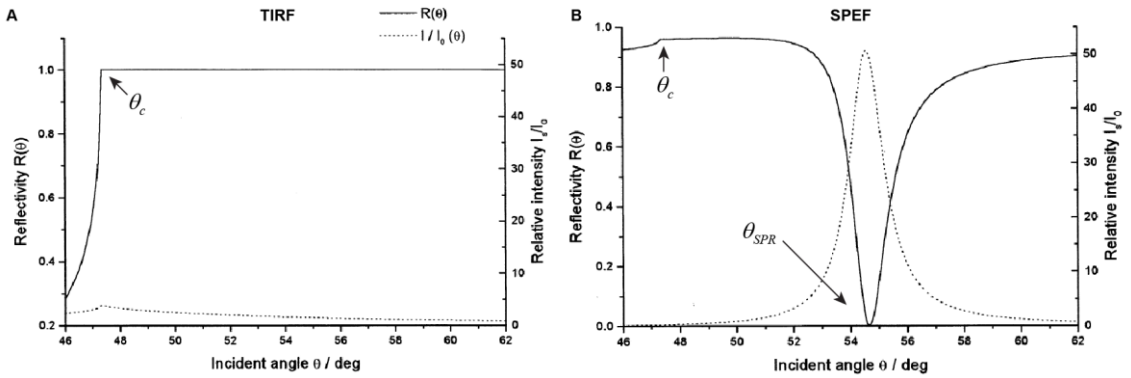

Figure 2.27: Reflectivity and relative surface field intensity in TIR (A) and SPEF (B) for a glass/water interface (TIR) and a silver/water interface (SPEF) for $\lambda = 633$ nm. Reprint with permission from [Liebermann & Knoll, 2000].

As demonstrated above, evanecent field based sensing techniques also produce a field reaching into the dielectric which can be used to excite fluorophores similarly to TIRF. In SPR, this technique is called surface plasmon-enhanced fluorescence (SPEF) or surface plasmon fluorescence spectroscopy, while for MCWG the term surface enhanced fluorescence (SEF) will be used. SPEF and SEF have the advantage that, compared to TIRF, a significant field enhancement is achieved resulting in a better signal to noise ratio [Fort & Grésillon, 2008; Liebermann & Knoll, 2000]. Figure 2.27 shows simulated reflectivity and field intensity enhancements for the case of TIR (glass-water interface, Figure 2.27A) and for SPR (silver-water interface, Figure 2.27B). The solid lines in Figure 2.27 represent the reflected light intensity as a function of the angle of incidence. In line with the discussions in Section 2.1.2, in the case of TIR when approaching the critical angle (θ_c), there is a steep increase in reflectivity reaching unity for $\theta \geq \theta_c$ and light is totally-internally reflected from the surface (Figure 2.27A). When a thin metal film is deposited on top of the glass, SPR can be excited at the silver/water interface and the characteristic dip in reflectance is observed around the coupling angle (θ_{SPR}, Figure 2.27B)).

The dotted traces in Figure 2.27 represent the field intensity at the surface scaled to the incoming field intensity (I_s/I_0). It should be noted that, even under TIR conditions, a moderate field enhancement of 4 times is possible (dotted trace, Figure 2.27A). Under SPR conditions, however, the surface field intensity increases dramatically resulting in enhancement of approx. 50 times for a thin silver film (dotted trace, Figure 2.27B)[Liebermann & Knoll, 2000]. In TIR

nearly all light gets reflected from the surface for $\theta \geq \theta_c$ and only a small portion of energy is available in the evanescent field. In SPR, on the other hand, the incoming light is coupled resonantly into the surface plasmon mode and confined strongly at the metal surface. As discussed above, in the case of MCWG (see Figure 2.15) field intensities can further be nearly tripled compared to SPR making a strong evanescent field available for fluorescence excitation at the sensor's surface.

2.6.1 Energy Transfer and Quenching Mechanisms in SPEF

The strong field enhancements in SPR and MCWG leads to an increased excitation rate of the fluorophores at the surface and to an enhanced fluorescence intensity (Figure 2.28A SPEF) [Dostálek & Knoll, 2008]. The thin metal layer, however, also introduces two new decay channels for chromophores in proximity to the metal surface. Within the *Förster distance* (typically around 10 nm), an energy transfer between the fluorophores and the electrons in the metal can take place (*Förster energy transfer,* Figure 2.28A). The energy then dissipates within the metal as heat, effectively quenching florescence within this distance. If the distance between the fluorophore and the metal surface is increased, the Förster energy transfer cannot take place. To prevent this non-radiative decay, a thin ($d > d_{Förster}$) dielectric spacer can be placed on top of the metal surface and thereby effectively prevent quenching [Murakami *et al.*, 2012]. It should be noted that this configuration corresponds already to the case for an MCWG sensor chip where a thick dielectric core prevents a Förster energy transfer.

For larger distances ($d_{Förster} \leq d \leq 2d_{Förster}$) a second decay channel opens and the emitted light can couple back into a plasmonics mode, termed *surface plasmon coupled emission* (SPEC, Figure 2.28B). In the case of a prism or grating coupler, the fluorescent light from the plasmonic mode can out-couple towards the substrate and is re-radiated at a specific angle towards the input side. Since the fluorescent light has a longer wavelength, its propagation constant differs from the plasmonics mode excited by the incident light beam used for SPR excitation. This results in a highly directional out-coupling at lower angles of incidence and can be used to separate the two signals [Calander, 2004].

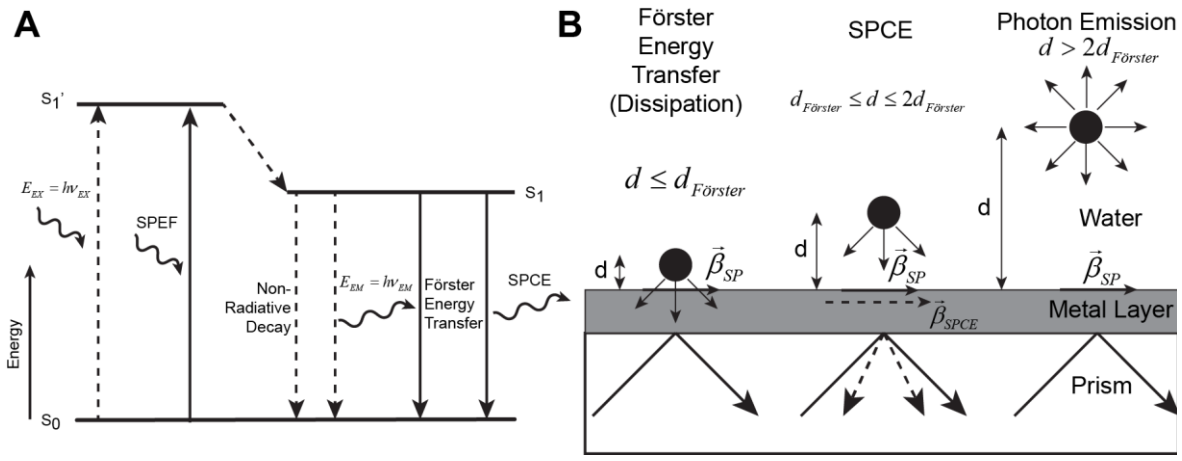

Figure 2.28: Modified Jablonski diagram for SPEF (A) and schematic of different coupling regimes (B). for a metal/water interface as a function of the distance from the fluorophore to the metal layer. Adaptation with permission from [Dostálek & Knoll, 2008; Liebermann & Knoll, 2000] .

For larger distances ($d > 2d_{Förster}$), the metal surface does not significantly impact the fluorescence emission. Since in SPEF and SEF an evanescent field is used to excite the fluorophores, the fluorescence intensity also decreases exponentially with increasing separation distance [Dostálek & Knoll, 2008]. Since in SPR the penetration depth is very shallow, only fluorophores within a very small volume are excited. By using sensor setups with deeper penetration depth, as it is the case for long range SPR (LRSPR) and MCWG, this volume can be increased and fluorophores at distances > 500 nm can be exited [Kasry & Knoll, 2006]. Thus, the increased penetration depth in MCWG and LRSPR can be particularly interesting for visualizing cellular structures that are inside the cell's body and often hundreds of nanometer away from the sensor's surface [Kanchanawong *et al.*, 2010].

2.6.2 Surface Enhanced Fluorescence of Living Cells

Multiple studies have already applied SPEF spectroscopy in different areas of biosensing [Dostálek & Knoll, 2008]. In the case of classical binding assays, the use of SPEF can enhance the limit of detection (LOD) by several orders of magnitude. For example, in DNA hybridization, the LOD was enhanced from 0.1 nM down to 100 fM [Vaisocherová *et al.*, 2006; Yao *et al.*, 2004] and even down to 80 fM in the case of antigen-antibody assays [Yu *et al.*, 2004]. SPEF based spectroscopy was also applied to detect whole organisms such as bacteria and while no shift in the SPR signal was observed for bacteria concentrations below 10^5 colony

forming units (cfu)/mL, the combination with SPEF allowed for LOD of under10 cfu/ml [C. J. Huang *et al.*, 2011].

In initial work applying SPEF to visualize cellular structures, the enhancement effect of SPEF compared to TIR microscopy was experimentally demonstrated and authors reported a signal increase of one order of magnitude for the visualization of green fluorescent protein (GFP) labeled membrane proteins in human melanoma cells [He *et al.*, 2006]. In later work, they expanded their imaging system capability and could successfully combine SPEF with two-photon fluorescence microscopy [He *et al.*, 2009], achieving a 30-fold enhancement by SPEF and greatly improving their signal-to-noise-ratio (SNR). While these applications demonstrated the advantages of SPEF for live cell fluorescence imaging, in these works the reflected excitation light (i.e. SPR signal) was not monitored to further gain information on cell processes.

To simultaneously monitor both the SPEF and SPR signals, the same group developed an objective based wide field surface plasmon phase microscope in combination with their SPEF setup that allowed them to study cellular structures in both modalities [He *et al.*, 2010]. Since the numerical aperture of this system was too low to excite surface plasmons on a silver coated chip, the authors had to effectively detuned the metal layer to achieve coupling into the plasmonics mode at lower angles of incidence. This had great consequences for the reflectivity spectrum (broadening of the dip and lower sensitivity), ultimately impairing the image contrast and sensitivity. In order to overcome these issues, they modified the reflected light path detection system and used phase measurements to generate an SPR image. Using this technique, they could successfully visualize clusters of intracellular proteins in a living fibroblast.

These initial applications of SPEF to living cells strongly focused on the imaging of static cellular structures and helped to demonstrate the advantages in terms of SNR of using a combined SPR and SPEF system. More recently, our group further quantified dynamic processes within living cells following GPCR signaling and toxin induced disruption of the actin cytoskeleton with a combination of SPEF imaging and SPR spectroscopy [Chabot *et al.*, 2013]. The combination of these two modalities could successfully show that the reorganization of intracellular actin structures following receptor activation plays a major role in the observed

SPR signal. While earlier studies had to rely on separate microscopy techniques to validate the SPR signal, this work demonstrated the advantages of simultaneously using label-free and label-based approaches to directly visualize and quantify the underlying structural mechanisms leading to the sensor's signal for a large population of cells.

2.7 Summary

In this chapter, different concepts from integrated optics were introduced and it was demonstrated how evanescent field based sensor chips can be designed. Different biosensing techniques were presented and two evanescent field based sensor designs, namely SPR and MCWG, were discussed in greater detail and presented in the context of live cell sensing. MCWG were found to exhibit a deeper penetration depth and a higher field enhancements compared to SPR while keeping the attenuation distance well below 10 μm. These advantages make MCWG based sensor chips well suited to study micrometer sized objects such as cells in both label-free and labeled biosensing modalities. Further, due to their native support for imaging and their sufficiently low attenuation distance, these sensor chips should be capable of resolving individual cells and enables the study of single cell behavior and activity and extract heterogeneities within the cellular response profiles. In the following chapter, the design, construction and characterization of an microscope objective-based MCWG imaging system will be described. In CHAPTER 4 this imaging system will then be applied to detect single cells and cell monolayer activity in a two different of applications. In the last chapter, the advantages of a combined MCWG imaging and SEF system are demonstrated. The information extracted by such a combination of label-free and labeled imaging modalities complement each other for an integral assessment of the signaling and structural origin of the sensor's response in complex samples such as living cells.

CHAPTER 3 Metal Clad Waveguide (MCWG) Based Imaging using a High Numerical Aperture Microscope Objective

3.1 Overview of Article

Authors and affiliations:

Thomas Söllradl: PhD student, Laboratoire Nanotechnologies Nanosystèmes (LN2)- CNRS UMI-3463, Institut Interdisciplinaire d'Innovation Technologique (3IT), Département de Pharmacologie et Physiologie, Université de Sherbrooke, Sherbrooke, Canada

Frederic A. Banville: PhD student, Laboratoire Nanotechnologies Nanosystèmes (LN2)- CNRS UMI-3463, Institut Interdisciplinaire d'Innovation Technologique (3IT), Université de Sherbrooke, Sherbrooke, Canada

Vincent Chabot: Laboratoire Nanotechnologies Nanosystèmes (LN2)- CNRS UMI-3463, Institut Interdisciplinaire d'Innovation Technologique (3IT), Université de Sherbrooke, Sherbrooke, Canada

Michael Canva: Professor, Laboratoire Nanotechnologies Nanosystèmes (LN2)- CNRS UMI-3463, Institut Interdisciplinaire d'Innovation Technologique (3IT), Université de Sherbrooke, Sherbrooke, Canada

Michel Grandbois: Professor, Laboratoire Nanotechnologies Nanosystèmes (LN2)- CNRS UMI-3463, Département de Pharmacologie et Physiologie, Institut de Pharmacologie de Sherbrooke, Université de Sherbrooke, Sherbrooke, Canada

Paul G. Charette: Professor, Laboratoire Nanotechnologies Nanosystèmes (LN2)- CNRS UMI-3463, Institut Interdisciplinaire d'Innovation Technologique (3IT), Université de Sherbrooke, Sherbrooke, Canada

Date of acceptance: 18.01.2017

State of the article: Published

Journal: Optics Express

Complete Reference: Söllradl, T., Banville, F. A., Chabot, V., Canva, M., Grandbois, M., & Charette, P. G. (2017). Metal clad waveguide (MCWG) based imaging using a high numerical aperture microscope objective. Optics Express, 25(3), 1666. http://doi.org/10.1364/OE.25.001666

Contribution of the manuscript

Evanescent-field based methods such as surface plasmon resonance (SPR) have been applied successfully to image cells and bacteria [Yanase *et al.*, 2010] While highly sensitive, the relatively shallow probing depth of SPR (typically < 200 nm) is not well suited to the study of such relatively large objects. In this manuscript, we demonstrate how metal-clad waveguides (MCWG) can be used for evanescent-field based imaging with much deeper probing depth, with high sensitivity and spatial resolution.

Originality of the work

Though MCWG have been used previously for biosensing by ourselves [Convert *et al.*, 2012] and others [N. Skivesen *et al.*, 2007], to our knowledge, this is the first time MCWG have been used for imaging. We initially present a detailed numerical study of MCWG imaging performance as a function of device geometry and wavelength, and compare these findings to the most commonly-used SPR and "long-range" LR-SPR structures. These theoretical findings are then validated by experimental results on synthetic targets and live cells. This quantitative comparative analysis of SPR, LR-SPR, and MCWG will enable readers to make an informed choice about which of the three techniques is best suited for a particular application. We believe our work will provide researchers in the fields of biosensing and biological microscopy with a new and more powerful tool to study bacteria and cells.

Contributions by author

Thomas Söllradl was responsible for the optical setup, fabrication of the sensor chips as well as all the experimental characterization. Further, he was involved in the theoretical work and with

simulations as well as with writing the manuscript. Frederic Banville helped with the simulations and Vincent Chabot with the initial optical setup. Michael Canva, Michel Grandbois and Paul Charette supervised this work, participated in discussions as well as in the review of the manuscript. Paul Charette further contributed to the manuscript with simulations.

3.2 French Title

Imagerie basée sur les guides d'ondes à gaine métallique utilisant un objectif de microscope à grande ouverture numérique.

3.3 Abstract (French)

Les méthodes basées sur les champs évanescents telles que la résonance des plasmons de surfaces (SPR) ont été employées efficacement dans le but de prendre des images, sans marqueur fluorescent, de matériel biologique situé à proximité d'une surface de détection. Toutefois, la faible profondeur de détection de la SPR (typiquement inférieure à ~ 200nm) peut être problématique lorsqu'il est nécessaire d'observer des objets biologiques relativement épais comme des cellules ou des bactéries. Dans cet article, nous démontrons comment les guides d'ondes à gaine métallique (MCWG) peuvent être utilisés afin d'obtenir une plus grande profondeur de détection, comparativement aux systèmes SPR, tout en maintenant une bonne résolution spatiale en imagerie. Des simulations numériques comparatives de la résolution spatiale en imagerie en fonction de la profondeur de mesure sont présentées pour un certain nombre de configurations usuelles en SPR, SPR longue portée et MCWG. Ces simulations démontrent que la MCWG offre le meilleur compromis entre la résolution et la profondeur de mesure pour l'observation d'objets biologiques plus épais. Les résultats expérimentaux d'imagerie sur des modèles synthétiques et des cellules vivantes valident valide les simulations effectuées et démontre les capacités de la méthode.

3.4 Abstract (English)

Evanescent-field based methods such as surface plasmon resonance (SPR) have been used very effectively for label-free imaging of microscopic biological material in close proximity to a sensing surface. However, the shallow probing depth of SPR (typically less than ~200 nm) can

be problematic when imaging relatively thick biological objects such as cells or bacteria. In this paper, we demonstrate how metal-clad waveguides (MCWG) can be used to achieve deeper probing depth compared to SPR while maintaining good imaging spatial resolution. Comparative numerical simulations of imaging spatial resolution versus probing depth are shown for a number of common SPR, long-range SPR, and MCWG configurations, demonstrating that MCWG offer the best compromise between resolution and depth for imaging thick biological objects. Experimental results of synthetic target and live cell imaging are shown that validate the numerical simulations and demonstrate the capabilities of the method.

3.5 Introduction

Ever since its experimental demonstration by Otto and Kretschmann [Kretschmann & Raether, 1968; Andreas Otto, 1968], surface plasmon resonance (SPR) has become a valuable label-free sensing approach with a broad range of applications in the fields of chemistry, engineering, and biology. The basis for SPR sensing is that TM-polarized light can be guided by a surface-bound mode at the interface between a metal and a dielectric, where the dielectric is the sensing medium (a gas or a liquid). Although there is a simple closed-form solution to determine the effective index for this guided "surface plasmon mode" [Homola, 2003], it can also be obtained by solving the transcendental equation for guided TM modes in a planar waveguide derived from Maxwell's equations with a null core thickness. As with guided modes in a conventional dielectric waveguide, light can be coupled to the surface plasmon mode in a number of ways, with prism-based systems being the most common (optical tunneling via total internal reflection). Since absorption of visible and near-IR light in most metals is high, the surface plasmon mode is highly lossy. Indeed, these losses in the metal are at the heart of the resonant nature of plasmonics-based sensors, where coupling conditions can be adjusted such that virtually all light injected into the system at the operating point is absorbed (critical coupling). As is typical for resonance-based guided-mode systems, critical coupling conditions are very sensitive to the waveguide physical parameters. As a result, minute chemical or physical changes that perturb the refractive index of the sensing media above the metal surface will detune the system from resonance and be observable either as intensity variations of the reflected light when operating at fixed incidence angle and wavelength, or as a change in incidence angle and/or wavelength of the critical coupling conditions [Sereda *et al.*, 2014]. Owing to the

evanescent profile of the electric field in the dielectric, SPR is sensitive to refractive index changes in close proximity to the metal surface. The distance from the interface (normal to the direction of mode propagation) over which the mode amplitude decreases by 1/e of its value at the interface is termed the "penetration depth", typically below 200 nm for visible wavelengths and noble metals [Homola, 2003], and is commonly used as a measure of effective sensing depth.

In surface plasmon resonance imaging (SPRI), a 2D photodetector such as a CCD camera is used to monitor changes in reflectivity so that refractive index perturbations in the dielectric medium can be spatially resolved in the plane of the metal/dielectric interface, with most systems using a prism for input/output light coupling. Due to the physical size of the prism, the imaging optics typically have modest resolving power as they are necessarily based on long working distance low numerical apertures objectives. In practice, however, spatial resolution in prims-based SPRI is normally well above the diffraction limit of the optics due to aberrations and distortion resulting from passage of light through the prism [Laplatine *et al.*, 2014], typically in the order of ten(s) of microns. To overcome these limitations, a high-numerical aperture microscope objective can be used instead to directly couple in/out of the surface plasmon mode [B. Huang *et al.*, 2007]. Such systems, however, reveal an additional impediment to spatial resolution in SPRI. The amplitude of the guided surface plasmon mode decreases exponentially in the direction of propagation due to losses in the metal, where the distance over which the mode energy decreases by 1/e is termed the "propagation distance" or "attenuation length". In high-resolution SPRI, this finite attenuation distance causes cross-talk between neighboring pixels along the direction of mode propagation, effectively blurring the images along that axis and resulting in a spatial resolution imbalance between the two orthogonal axes in the image plane. Though this effect can be slightly noticeable in prism-based systems, it is a significant problem in high magnification microscope objective-based systems. This effect can be reduced to some extent by using shorter wavelength excitation [B. Huang *et al.*, 2007], combining images acquired with distinct mode propagation directions [Banville *et al.*, 2015], or surface nanostructuring [D. J. Kim & Kim, 2010].

There is increasing interest in surface-based label-free imaging of relatively large microscopic objects such as bacteria and cells [Peterson *et al.*, 2014; Wang *et al.*, 2012; Yanase *et al.*, 2010b]. Conventional "short-range" SPRI systems are very effective for studying cell-substrate adhesion sites, structures that are located within the first hundred nanometers of the cell body above the sensor surface [Kanchanawong *et al.*, 2010]. There is, however, a demand to study other cytoskeletal components located higher up in the cell body such as actin (> 160 nm) and intracellular organelles (> 200 nm), requiring deeper probing depths into the dielectric medium than conventional "short-range" SPRI systems can deliver. To increase penetration depth, longer wavelengths in the near-IR can be used with SPRI. Alternatively, so-called "long-range" SPR (LR-SPR) can be used [Chabot *et al.*, 2012; Krupin *et al.*, 2013; Méjard *et al.*, 2013; Wark *et al.*, 2005], as discussed below. In both cases, however, imaging resolution along the direction of mode propagation deteriorates commensurately with penetration depth due to the increased attenuation distance.

As demonstrated in this paper, a third and very flexible approach to increase penetration depth while more effectively controlling attenuation distance involves the use of metal-clad waveguides (MCWG): dielectric core waveguides with metal film claddings on one or more sides) [Kaminow *et al.*, 1974; Nina Skivesen *et al.*, 2005]. In fact, unbeknownst to many in the plasmonics community, SPR is actually a special case of this broader class of waveguides: conventional propagating SPR devices based on a single metal/dielectric interface can be considered as MCWG waveguides that support a single TM surface mode, i.e. a MCWG with a null core thickness.

In this work, we present a MCWG-based imaging system based on a high numerical aperture objective. Numerical simulation results comparing the estimated performance of the MCWG-based system compared to SPR and LR-SPR are shown. The system's imaging capabilities are characterized using synthetic structures and living cells.

3.6 Metal-clad vs plasmonics waveguide modes: numerical simulations

This section compares the expected performance of sensor chip structures based on conventional (short-range) SPR, long-range SPR (LR-SPR), and metal-clad waveguides (MCWG) using four

performance metrics: refractive index measurement sensitivity and dynamic range, attenuation length (spatial resolution in the imaging plane), and penetration depth into the dielectric (imaging depth). Since the objective is to probe deeply into the dielectric, the "bulk" definition of sensitivity is used (maximum reflectivity change as a function of refractive index change in the dielectric volume) as opposed to sensitivity defined with respect to surface biolayer (adlayer) thickness or surface coverage.

These numerical analyses were conducted using modal analysis methods (also known as mode solvers or eigen mode expansion) based on solving Maxwell's equations with finite differences on a rectangular grid in the plane perpendicular to the direction of propagation, using the FIMMWAVE software package (Photon Design, UK). This type of analysis yields the complete

description of guided modes supported by the structure (complex effective index of each mode with its full 3D electromagnetic profile). The simulated structures are planar waveguides

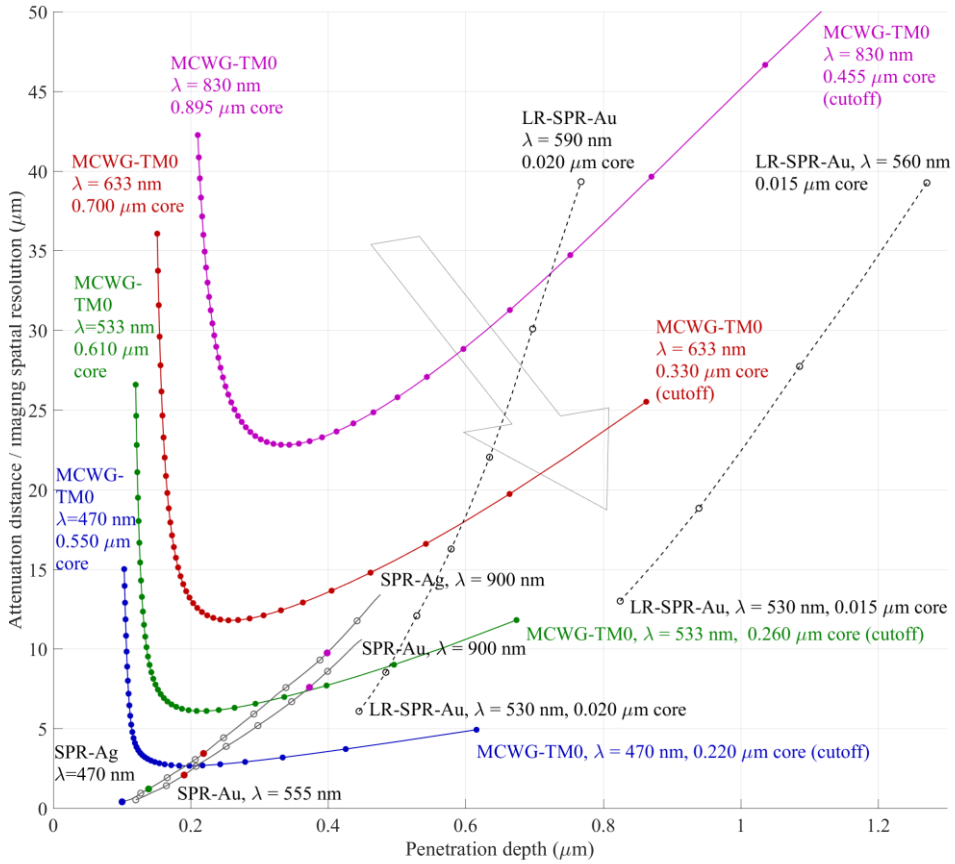

Figure 3.1: Mode attenuation distance (imaging spatial resolution) vs penetration depth in the dielectric for MCWG TM0 modes (solid colored lines), SPR (solid gray lines), and LR-SPR (hashed grey lines). The diagonal arrow in the background indicates the direction of improving performance for imaging of thick objects such as cells, i.e. decreasing attenuation distance (better resolution) and increasing penetration depth. Data calculated using FIMMWAVE.

• MCWG: TM0 modes (colored curves) at wavelengths of 470 nm, 533 nm, 633 nm, and 830 nm, over a range of KMPR core thicknesses. Markers indicate core thickness intervals of 10 nm, starting at cutoff (thinnest core supporting a guided mode, rightmost point on each plot);

• SPR: Au/water and Ag/water interface surface modes over a range of wavelengths (Au: 555 nm – 900 nm, Ag: 470 nm - 900 nm). Black markers indicate wavelength intervals of 50 nm, while colored markers indicate the wavelengths corresponding to the four MCWG curves (470 nm, 533 nm, 633 nm, 830 nm);

• LR-SPR: symmetric mode in a Teflon/Au/water stack over a range of relevant wavelengths (15 nm Au core: 530 nm to 560 nm, 20 nm Au core: 530 nm to 590 nm). Markers indicate wavelength intervals of 10 nm;

consisting of thin film stacks of infinite extend in the film plane, sandwiched between two semi-infinite volumes of BK7 glass (bottom) and distilled water (top) modeled by perfectly matched layers (PML). Note that though we measured the dielectric indices of the materials we used with an ellipsometer, the numerical simulations shown below are based on optical properties obtained from the literature and manufacturers so that our results may be reproducible by others. Since the refractive indices for the different materials, most notably metals, may vary significantly according to fabrication conditions, the simulations result shown below will likely differ from actual experimental results. However, the relative performance of the different cases illustrated will remain the same. Hence, these simulations based on materials data from the literature are useful in making informed choices when comparing the relative merits of the cases discussed.

MCWG devices have been shown by us [Convert *et al.*, 2012] and others [Nina Skivesen *et al.*, 2005] to have superior bulk sensitivity compared to SPR. Though LR-SPR can have slightly better bulk sensitivity than MCWG [Convert *et al.*, 2012], this comes at the expense of a much narrower dynamic range, which is an important parameter for cell imaging since the intra- and extra-cellular media can have significant refractive index differences ($n \approx 1.33$ vs. $n = 1.36$ - 1.39 [Choi *et al.*, 2007], respectively). Based on measurement sensitivity and dynamic range metrics, therefore, MCWG-based devices are strong candidates for cell imaging.

The attenuation distance (imaging spatial resolution in the plane) and penetration depth are two metrics that are in direct competition. Figure 3.1 illustrates this trade-off for three waveguide constructs (MCWG, SPR, LR-SPR) based on Au and Ag films, the most commonly used metals. Numerical simulation results of attenuation distance versus penetration depth are plotted for: (1) MCWG TM0 modes (colored lines) for a range of core thicknesses at four typical wavelengths (470 nm, 532 nm, 632 nm, and 830 nm). The dielectric core material of the MCWG is KMPR (MichroChem, USA), a photopolymer similar to SU8 having superior resistance to fissuring during thermal treatment making it a better choice for microfluidics systems [Convert *et al.*, 2008]. The metal stack between the BK7 substrate and the KMPR core consists of a 3 nm Ni adhesion layer, a 23 nm Ag “main” metal layer and a 5 nm Au passivation layer.

The data for an equivalent MCWG structure with Au as the main metal (Cr/Au metal stack) are not shown as the resulting sensitivity and attenuation distance vs penetration depth trade-off are less advantageous compared to an Ag-based metal stack [Moreau *et al.*, 2014]; (2) SPR modes (solid grey lines) for Au and Ag metal films (including a 3 nm Cr adhesion layer for Au and a 3 nm Ni adhesion layer for Ag); (3) LR-SPR symmetric modes (hashed grey lines) for 15 nm and 20 nm thickness Au cores (NB: simulation data for Ag films are not presented as the resulting much longer attenuation distances are not of practical value for imaging; simulation data for the asymmetric LR-SPR modes are not shown as they are very close to the single-interface SPR modes). The bottom cladding material for the LR-SPR waveguides is Teflon AF1300. In all cases, refractive indices for the metals were taken from Johnson & Christy [Johnson & Christy, 1972], the Sellmeier equation was used for the refractive index of water [Daimon & Masumura, 2007] and Teflon [M. K. Yang *et al.*, 2008], the Cauchy equation was used for the refractive index of KMPR (coefficients from the product datasheet available on the MicroChem website). The shortest wavelengths considered in the simulations were 450 nm for Ag and 530 nm for Au since losses in these metals at shorter wavelengths reduce measurement sensitivity and dynamic range to very low levels [Pyo *et al.*, 2005]. The longest wavelengths considered are in the near IR (900 nm) which is the practical limit for Si-based imaging devices.

For imaging thick objects such as cells, the optimal operating point is in the lower right area of the figure as indicated by the large diagonal arrow in the background: short attenuation distance (high spatial resolution) and deep penetration. In all cases, the spatial resolution vs penetration depth tradeoff is a function of wavelength: losses in the metals increase with decreasing wavelength thereby shortening the attenuation distance and improving spatial resolution, while penetration depth decreases accordingly. In the cases of LR-SPR and MCWG, the degree of mode confinement is also in play: a thinner core will decrease mode confinement, resulting in deeper probing depth but at the expense of a decrease in spatial resolution due to the accompanying increase in attenuation length (proportionately lower losses in the metal).

Clearly, SPR-based devices are capable of the highest spatial resolution but are limited to relatively shallow probing depths of ~0.4 µm (830 nm excitation wavelength). For deeper probing depths, the best compromise relative to attenuation distance is obtained for MCWG and LR-SPR at short wavelengths. In case of the LR-SPR, however, wavelengths below ~550 nm are close to the practical operating limit for plasmonics with Au where sensitivity is significantly

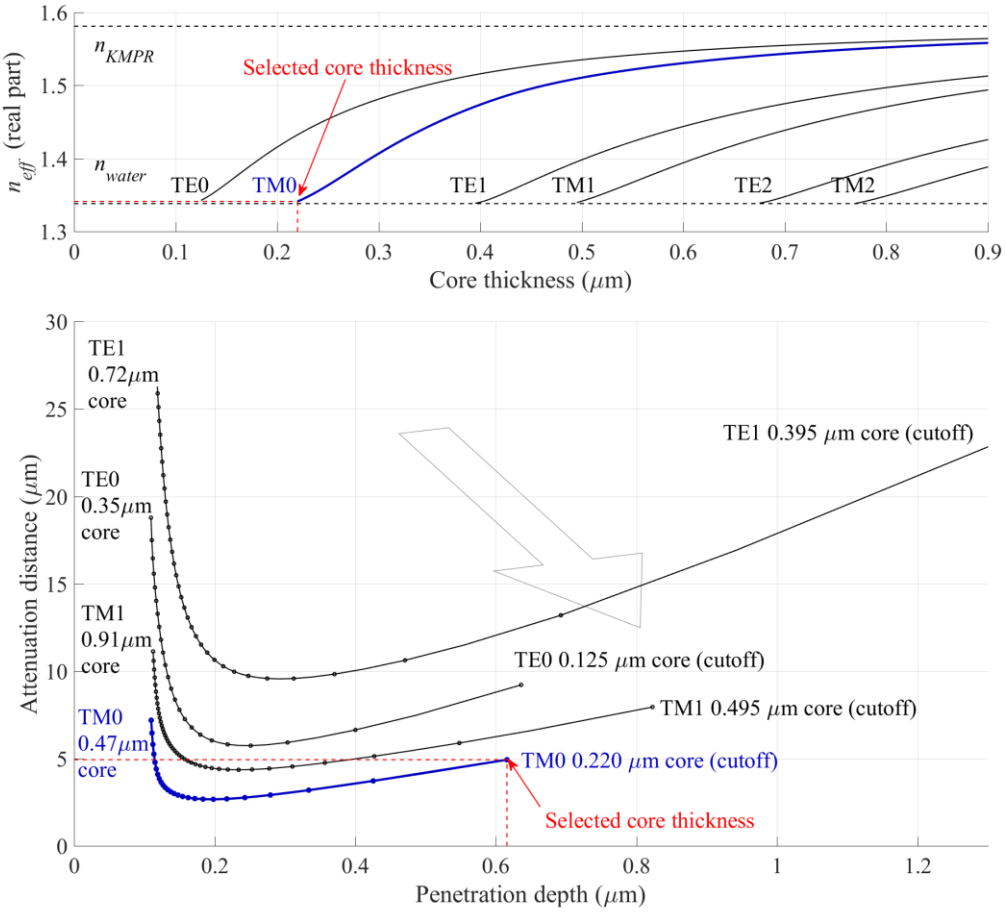

Figure 3.2: MCWG modal characteristics at λ = 0.470 nm as a function of core thickness and mode order, waveguide stack: BK7 – Ni(3 nm)/Ag(23 nm)/Au(5 nm) – KMPR - water. The dashed red line indicates the core thickness selected for the experiments (0.220 µm). Plots for the TM0 mode are shown in blue. Data calculated with FIMMWAVE. TOP: mode effective indices (neff, real part) as a function of core thickness, delimited by the indices of water (cladding with highest index, bottom horizontal dashed line) and KMPR (waveguide core, top horizontal dashed line), i.e.: $n_{water} < Re\{n_{eff}\} < n_{KMPR}$. BOTTOM: attenuation distance vs penetration depth in the dielectric (water) for modes TE0, TM0, TE1, and TM1 as a function of core thickness - markers indicate core thickness intervals of 0.010 µm. The large diagonal arrow in the background indicates the direction of improving performance for imaging of thick objects, i.e. decreasing attenuation distance (improving resolution) and increasing penetration depth.

reduced. Conversely, Ag-based devices operate very well at short wavelengths in the visible range. Hence, MCWG-based devices at short wavelengths (470 nm in our case) offer the better tradeoff between achievable resolution and penetration depth for imaging when operated close to the cutoff (thinnest waveguide core supporting a guided mode).

Figure 3.2 shows numerical simulation results at $\lambda = 470$ nm illustrating the dependence of the MCWG characteristics on the core layer thickness, starting from the cutoff thickness (thinnest core that will support a guided mode). Figure 3.2-TOP shows the mode effective indices as a function of core thickness for the first six modes: mode TE0 appears at a core thickness of ~0.13 μm and mode TM0 at a core thickness of ~0.22 μm, followed by the second TE and TM modes at core thicknesses of ~0.40 μm and ~0.50 μm, respectively, etc. Figure 3.2-BOTTOM shows the attenuation distance versus penetration depth trade-off for the different modes, where markers indicate increments of 10 nm core thickness. Here again, for imaging thick objects such as cells, the optimal operating point is in the lower right area of the figure as indicated by the large diagonal arrow in the background. Clearly, mode TM0 performs best for imaging, followed closely by mode TM1. The higher order TE and TM modes could provide both greater penetration depth and additional physical insight into properties such as optical anisotropy [Salamon & Tollin, 2001].

For the set of experiments presented in this paper, we chose to use mode TM0 in a MCWG with a core thickness of 0.22 μm to operate just above cutoff in order to minimize mode confinement and thereby maximize penetration depth of the electric field into the cladding (dotted line in Figure 3.2 graphs). The corresponding Ag layer thickness (23 nm) yielding minimum reflectivity at resonance was calculated using the Fresnel equations. According to these simulation results, imaging resolution is ~ 5 μm and penetration depth ~ 0.62 μm. The bulk sensitivity for this structure is estimated to be 96 RIU^{-1}.

Figure 3.3-TOP shows numerical simulations at $\lambda = 470$ nm of the normalized electric (LEFT) and magnetic (RIGHT) field intensity profiles, $(|E_z|^2+|E_y|^2)/|E_0|^2$ and $|H_x|^2/|H_0|^2$, for mode TM0 in the chosen MCWG structure as a function of distance along the z axis (normal to the film plane) from the core/fluid interface at $z = 0$ μm, where E_0 and H_0 are the incident electric and

magnetic field intensities, respectively. As expected for a TM mode, the magnetic field is C^0 continuous at the material boundaries while the electric field is not. Also indicated in the electric field intensity graph is the penetration depth, L_p = 0.62 μm. Since the intensity profiles are normalized with respect to the incident field values, the graphs also indicate the so-called "field enhancement factor" defined as the ratio between the incident field intensity and the maximum field intensity in the fluid occurring at the core/fluid interface (z = 0 μm).

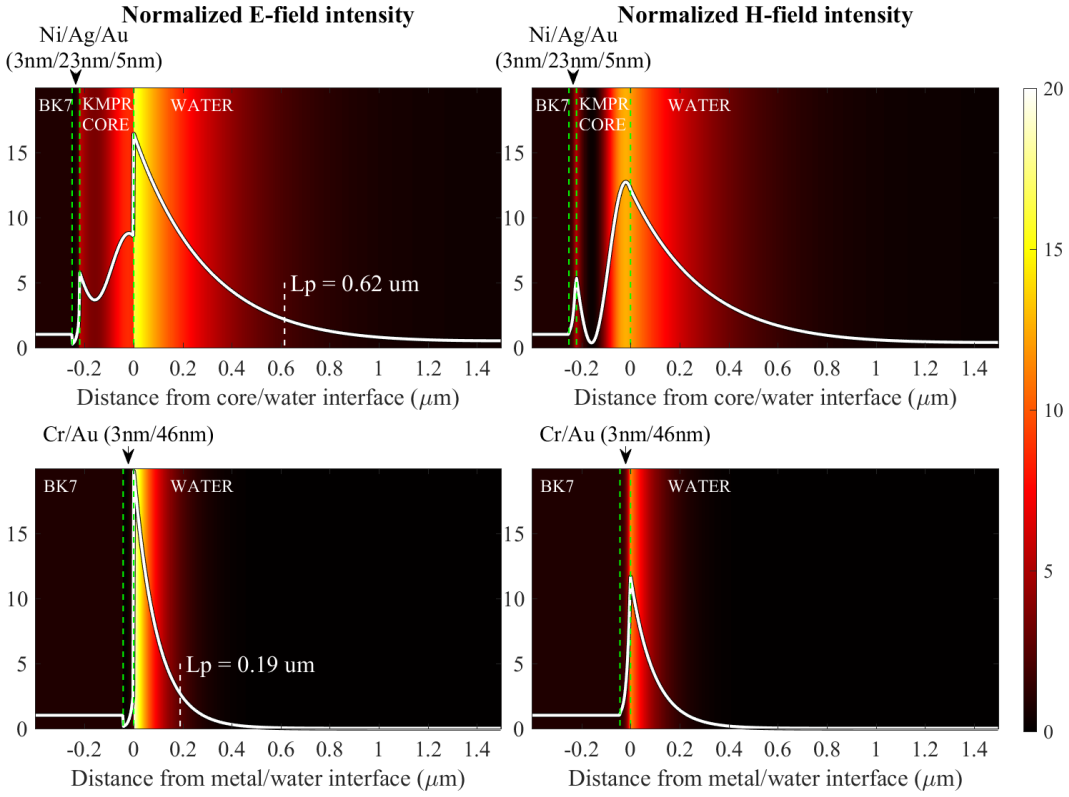

Figure 3.3: Electric (LEFT) and magnetic (RIGHT) field intensity profiles, $(|E_z|^2+|E_y|^2)/|E_0|^2$ and $|H_x|^2/|H_0|^2$, as a function of distance along the z axis (normal to the layer plane) from the fluid/solid interface (z = 0 μm) normalized with respect to the incident field intensities, E0 and H0. The Lp markers indicate the "penetration depth" into the fluid (distance from the interface over which the mode amplitude decreases by 1/e of its value at the interface). Background color indicates field intensity. TOP: TM0 mode in the chosen MCWG structure (220 nm KMPR core) at λ = 470 nm. The metal film stack, Ni(3 nm)/Ag(23 nm)/Au(5 nm), is located between the BK7 and KMPR layers. BOTTOM: SPR mode at a Au/water interface at λ = 633 nm. The metal film stack, Cr(3 nm)/Au(46 nm), is located between the BK7 and water layers. Data calculated with FIMMWAVE.

As seen in the figure, the electric field intensity enhancement factor is ~16×. Note that losses in the Au passivation layer slightly reduce this figure compared to MCWG based on bare Ag films, reported to achieve ~25× field enhancement [Salamon *et al.*, 1997]. The Ag/Au bimetallic

configuration, however, is stable in an aqueous solution (unlike bare Ag) and confers higher sensitivity than Au films alone [Ong *et al.*, 2006].

For comparison, Figure 3.3-BOTTOM shows the equivalent simulation results for an SPR mode at an Au/water interface at $\lambda = 633$ nm, one of the most common SPR sensing configurations. Relative to the MCWG TM0 mode (TOP), the penetration depth of the SPR mode is about 1/3 (shallower sensing depth), the propagation distance is about 1/2 (higher imaging spatial resolution, see Figure 3.1), while the field enhancement factor is of the same order. Note that for MCWG and "propagating" SPR modes (as opposed to localized plasmonic modes), the notion of "field enhancement" must be interpreted with care as it is highly dependent on the thickness of the metal layer. Indeed, by increasing/decreasing the metal layer thickness in the numerical simulations by a few nm, the field enhancement factor could be made to vary by as much as 50%. Hence, estimated values of field enhancement in this case must be interpreted somewhat qualitatively given practical layer deposition accuracy. Nevertheless, a high field enhancement factor is desirable as it leads to increased signal levels in surface plasmon enhanced fluorescence (SPEF) and surface-enhanced Raman spectroscopy (SERS) [Bryche *et al.*, 2016; Liebermann & Knoll, 2000].

3.7 Instrumentation setup

The optical setup used in our experiments is based on a design first proposed by Huang et al. [B. Huang *et al.*, 2007] for high-resolution SPRI. As shown in Figure 3.4, light from a 17.2 mW fiber-coupled LED centered at 470 nm (M470F3, Thorlabs, USA) passes through a collimating lens followed by a beam-expander (10X BE10M-A, Thorlabs, USA) and is focused into the back focal plane of a high numerical aperture objective (63x, NA = 1.46, Carl Zeiss, Germany). As a result, light incident onto, and reflected from, the backside of the MCWG chip is collimated. The low-coherence LED source reduces interference artifacts and its spectral bandwidth is restricted by a bandpass filter (FB470-10, FWHM = 10 nm, Chroma Technology, USA). The light reflected from the backside of the chip is collected back through the objective where the orthogonal polarizations are imaged by separate CCD cameras (Guppy F-146B, Allied Vision Tech., USA) via a polarizing beamsplitter.

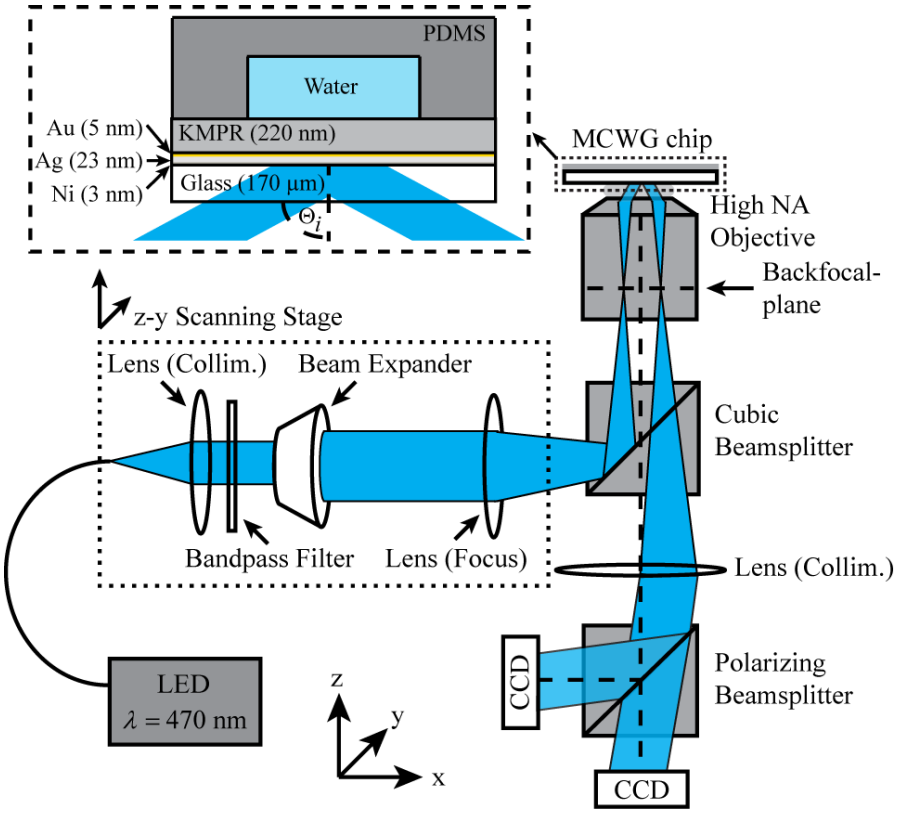

Figure 3.4: Schematic diagram of the imaging system based on a high numerical aperture objective. The inset shows the MCWG chip structure: BK7 glass – Ni(3 nm)/Ag(23 nm)/Au(5 nm) – KMPR(220 nm). A PDMS microfluidic channel is patterned atop the KMPR.

The lateral translation, d(x,y), of the focal spot from the origin in the back focal plane of the objective determines the angle of incidence, θi, of the light onto the back surface of the MCWG chip. For d(x,y) sufficiently large, light will be incident onto the sample at an angle greater than the angle of total internal reflection at the KMPR/fluid interface and guided modes in the waveguide on the topside of the chip can be excited by optical tunneling through the metal film, as with a conventional prism-based system. The collimating lens / beam expander / focusing lens subsystem is mounted on a linear scanning stage (17DRV114, CVI Melles-Griot, USA) which allows for arbitrary 2D positioning of the focused spot in the back focal plane of the objective. For example, by moving the spot in a circle of constant radius in the xy plane, guided modes of constant effective indices can be excited in the waveguide layer along any direction.

The MCWG chips (Figure 3.4 inset) were fabricated on 170 µm thick BK7 glass cover slips (Fisher Scientific, USA). After a solvent cleaning (2-propanol, acetone and water, 3 min

sonication per step), a 3 nm Ni adhesion layer was deposited by evaporation, followed by a 23 nm Ag layer and a 5 nm Au layer to passivate the silver for use in aqueous media. KMPR films (KMPR 1005, 15 % dilution with SU8 thinner, MicroChem, USA) were spin-coated on top of the metal layer. The epoxy-based photopolymer resin KMPR 1005 was chosen as the core material for its superior mechanical stability and moisture resistance compared to other commonly used resins such as SU8 [Blanco Carballo *et al.*, 2008; Ou *et al.*, 2008]. After a soft bake (100 °C, 2 min), samples were exposed to UV light (Model 200, OAI, USA) for 60 sec. (900 mJ/cm2, no filter), followed by an annealing on a hot plate (100 °C, 2 min) and hard-baked (180 °C, 3 hours) to stabilize the KMPR layer. KMPR thickness was verified by ellipsometry (Alpha_SE, J.A. Woollam Co.). PDMS fluid channels were patterned atop the KMPR. The experimental results presented in the next section were obtained using a typical sensor chip with a KMPR thickness of 219.4 ±0.3 nm.

3.8 Experimental Results and Discussion

3.8.1 Lateral imaging resolution

To experimentally characterize the lateral imaging resolution of our MCWG–based imaging system, the PDMS fluid channel wall boundaries were imaged at λ = 470 nm with the microscope system using two orthogonal light propagation directions, as shown in Figure 3.5. The light input/output coupling angle was selected for optimal coupling of the TM0 mode into water.

Figure 3.5 shows two typical reflectivity images acquired with light propagating along the y axis (TOP-LEFT) and x axis (TOP-RIGHT) in the film plane. As seen in the images, the water/PDMS boundary is sharp for light propagating parallel to the edge but blurred for light propagating perpendicular to the edge, as expected. Line profiles for both images are shown in Figure 3.5-BOTTOM. The exponential decay profile and oscillations at the PDMS/water

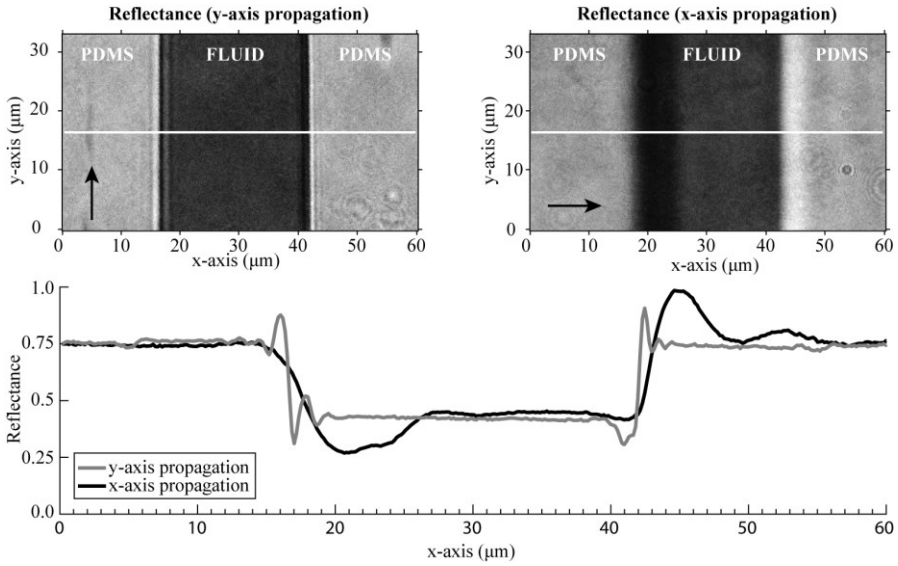

Figure 3.5: Typical pair of reflectivity images acquired with the microscope from two orthogonal directions of light propagation using the MCWG chip structure, where the back arrows indicate the direction of light propagation, clearly illustrating the resolution imbalance between the two axes in the plane. The angle of incidence was selected for maximum coupling of the TM0 mode into water at $\lambda = 470$ nm: the light grey zones in the images correspond to PDMS and the central dark grey zones to water. TOP-LEFT: image acquired with light propagating along the y axis. TOP-RIGHT: image acquired with light propagating along the x axis. BOTTOM: x-axis line profiles from both images (white horizontal lines across the top two images). The exponential profile and oscillations at the PDMS/water boundaries that are clearly seen in the x-axis propagation profile are due to the finite attenuation distance.

boundaries that are clearly seen in the x-axis propagation profile are due to the finite attenuation distance described earlier and have been observed by others [Rothenhäusler & Knoll, 1988]. The oscillation period (~7.4 μm) and attenuation distance (exponent of the exponential decay profile:~5 μm) calculated from the line profile are in close agreement with the theoretical predictions from our modeling results (6.8 μm and 4.9 μm, respectively) and similar work in the literature [Yeatman, 1996]. This phenomenon is the main resolution limitation along the axis of light propagation, whereas resolution along the axis perpendicular to light propagation is

ultimately limited by diffraction. Note that narrow fringes can also be seen in the y-axis propagation image parallel to the channel wall boundaries: they are most likely due to imperfect collimation by the light injection optics.

3.8.2Imaging depth

To experimentally confirm the deeper probing depth of MCWG-based imaging compared to conventional SPRI, 10 μm diameter polystyrene microbeads (Polysciences Inc., USA) were seeded on the surface of MCWG and SPR chips. Because the volume of the beads extends well beyond the penetration depths of the SPRI and MCWG modes and because of the high curvature of the bead shapes, the circular "shadow" cast by the beads on the surface will vary significantly according to penetration depth. As a result, the apparent bead size as measured by the two imaging modalities differ according to their respective penetration depths.

For proper sedimentation of the beads on the chip surfaces, a drop of bead dilution in water was first deposited on the surface with a micropipette followed by evaporation of the water using a hotplate. After evaporation, the chips were mounted in the microscope system and the chip surfaces were re-immersed in distilled water for imaging, with the beads remaining firmly adhered to the chip surface. Brightfield, SPRI (λ = 633 nm), and MCWG images (λ = 470 nm) from a typical experiment are shown in Figure 3.6.

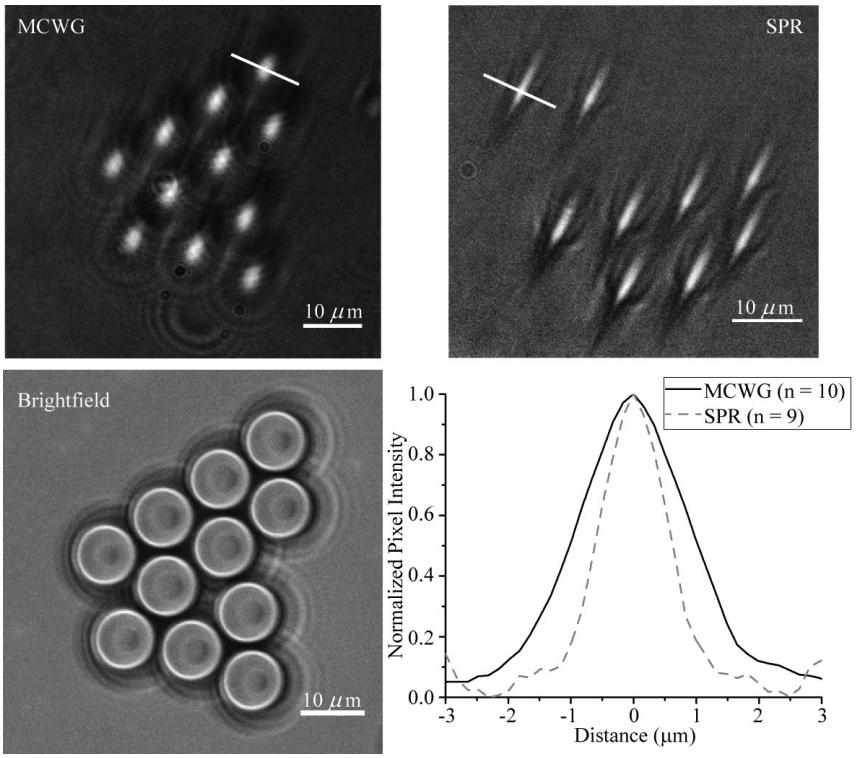

Figure 3.6: Images of 10 μm diameter polystyrene microbeads on the chip surface showing the effect of probing depth differences between MCWG and SPRI: TOP/LEFT: MCWG image (0.22 μm core, λ = 470 nm), TOP/RIGHT: SPRI (Au/water interface, λ = 633 nm), BOTTOM/LEFT: brightfield image. BOTTOM/RIGHT: plot of average bead image intensity profiles along the direction normal to light propagation (see example line overlays in two top images): the FWHM are 1.98±0.19 μm and 1.18±0.09 μm for the MCWG and SPRI bead images, respectively.

Because of the deeper penetration depth, the beads appear larger in the MCWG images compared to SPRI, as expected. Note that the "blurring artefact" caused by the finite attenuation distance in the direction of propagation is clearly visible in the two top images, as well as additional diffraction effects. To quantify the difference between the two imaging modalities, the average full widths at half maximum (FWHM) of the individual bead image profiles normal to the direction of light propagation were calculated across all imaged beads in both images (the example line overlays in the top images show the distance over which the individual bead image profiles were characterized). As seen in the plot of Figure 3.6-BOTTOM/RIGHT, the FWHM for the MCWG bead images (1.98±0.19 μm) is almost twice that for the SPRI bead images (1.18±0.09 μm), confirming the deeper probing depth of MCWG. Note that these values are

about half that predicted from a simple model based on the Fresnel equations evaluated at separate points in the plane of the surface according to the height of the bead/water interface at that location. The differences between the modeled and measured values are most likely due to the fact that the Fresnel equations model a stack of layers of infinite extent whereas the high curvature of the beads enables only a partial coupling of the excitation light to the guided modes at any point.

3.8.3Imaging of living cells

To demonstrate the performance of MCWG for live cell imaging, adherent human embryotic kidney cells (HEK-293) were cultured directly on the KMPR chip surfaces. The cells were visualized simultaneously in the system with brightfield microscopy from the topside and with MCWG-based microscopy from the underside. Typical results are shown in Figure 3.7. Since the cells are mostly transparent to visible light, little contrast is observed in the brightfield image (Figure 3.7-BOTTOM/LEFT) though the image shows that the cells are well adhered and spread out on the surface. The contours of the 4 cells in the field of view are indicated by dotted lines. A pair of corresponding MCWG images acquired using orthogonal directions of light propagation (Figure 3.7-TOP LEFT&RIGHT, arrows indicate directions of propagation) clearly show the 4 cells.

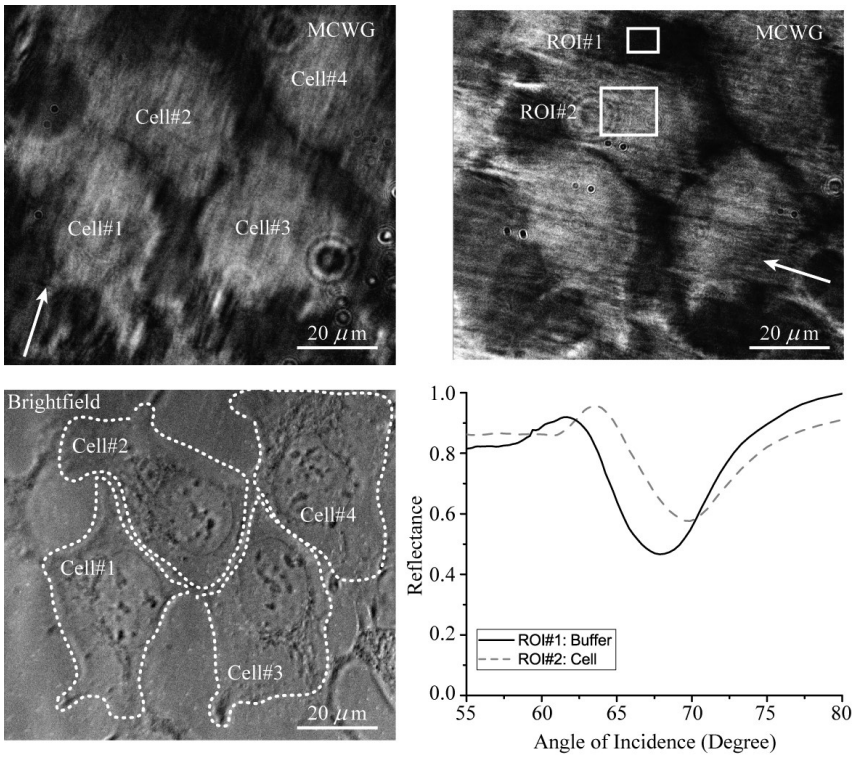

Figure 3.7: Simultaneous brightfield and MCWG-based imaging of live HEK-293 cells cultured directly on the KMPR surface of a MCWG chip. TOP: MCWG-based reflectivity images for orthogonal light propagation directions acquired at 67.55° incidence angle (propagation directions indicated by arrows). BOTTOM/LEFT: Brightfield image showing the contours of the 4 cells in the field of view. BOTTOM/RIGHT: average reflectivity as a function of incidence angle from the two ROIs shown in MCWG images. ROI#1: extra-cellular medium, ROI#2: intra-cellular medium.

Indeed, since the intracellular structures in the HEK-293 cells (membrane, cytoskeletal components, and organelles) have a higher refractive index than the intra- and extra-cellular fluid, the resulting heterogeneous refractive index distribution gives rise to high-contrast MCWG-based images. The HEK-293 cells express various fibrous cytoskeleton components (e.g. actin) to maintain shape and integrity. Some of these subcellular structures will randomly be aligned with the direction of light propagation in which case their diameter can be resolved while their overall length will appear blurred due to the finite attenuation distance (diagonal line artefacts in the MCWG images).

Two regions of interest (ROI) were selected in the MCWG images as outlined by rectangular overlays: one corresponding to an area of the surface exposed to a buffer solution only and one

encompassed by a cell body. Figure 3.7-BOTTOM/RIGHT shows measurements of average reflectivity as a function of incidence angle from both ROIs, where the optimal coupling angle differs between the two (ROI#1: 67.86°, ROI#2: 69.88°) due to the difference in average refractive index. Interestingly, the presence of the cell not only shifts the angular position of the minimum coupling angle but also increases the value of the reflectance minimum. This effect is due to the fact that the intra-cellular environment is electromagnetically "lossy" due to scattering of the evanescent-field by subcellular structures and organelles. Indeed, our group and others have shown that biological cells must be modeled as objects with complex refractive indices ($n = 1.38 + i0.011$ for ROI#2, determined by fitting to a Fresnel equations model) [Chabot *et al.*, 2012; Yashunsky *et al.*, 2010].

3.9 Conclusion

In this work, we have shown that MCWG-based microscopy is an effective and flexible method for high-resolution evanescent wave imaging. In particular, imaging using the MCWG TM0 mode at $\lambda = 470$ nm operating near cutoff (waveguide core thickness of 220 nm) is advantageous because of its deep probing depth (0.62 μm), good imaging spatial resolution (~5 μm), and high sensitivity (96 RIU^{-1}). While SPR is capable of higher spatial resolution at short wavelengths and LR-SPR can achieve deeper probing depth, MCWG-based microscopy offers the best compromise between spatial resolution and probing depth for imaging relatively thick biological objects such as cells or bacteria.

3.10 Acknowledgments

This work was supported by the Natural Sciences and Engineering Research Council of Canada (NSERC) (MG, PGC) and the Canadian Institutes of Health Research (CIHR) (MG, PGC). TS was supported by a doctoral scholarship from the Fonds de recherche du Québec – Nature et technologies (FRQNT).

CHAPTER 4 Label-free visualization and quantification of single cell activity using metal-clad waveguide (MCWG)-based microscopy

4.1 Overview of Article

Authors and affiliations:

Thomas Söllradl: PhD student, Laboratoire Nanotechnologies Nanosystèmes (LN2)- CNRS UMI-3463, Institut Interdisciplinaire d'Innovation Technologique (3IT), Département de Pharmacologie et Physiologie, Université de Sherbrooke, Sherbrooke, Canada
Carinthian Tech Research AG, Villach, Austria

Frederic A. Banville: PhD student, Laboratoire Nanotechnologies Nanosystèmes (LN2)- CNRS UMI-3463, Institut Interdisciplinaire d'Innovation Technologique (3IT), Université de Sherbrooke, Sherbrooke, Canada

Ulrike Fröhlich: Research Assistant, Département de Pharmacologie et Physiologie, Institut de Pharmacologie de Sherbrooke, Université de Sherbrooke, Sherbrooke, Canada

Michael Canva: Professor, Laboratoire Nanotechnologies Nanosystèmes (LN2)- CNRS UMI-3463, Institut Interdisciplinaire d'Innovation Technologique (3IT), Université de Sherbrooke, Sherbrooke, Canada

Paul G. Charette: Professor, Laboratoire Nanotechnologies Nanosystèmes (LN2)- CNRS UMI-3463, Institut Interdisciplinaire d'Innovation Technologique (3IT), Université de Sherbrooke, Sherbrooke, Canada

Michel Grandbois: Professor, Laboratoire Nanotechnologies Nanosystèmes (LN2)- CNRS UMI-3463, Département de Pharmacologie et Physiologie, Institut de Pharmacologie de Sherbrooke, Université de Sherbrooke, Sherbrooke, Canada

Date of publication: 15.02.2018

State of the article: Published

Journal: Biosensors and Bioelectronics

Complete Reference: T. Söllradl, F. A. Banville, U. Fröhlich, M. Canva, P. G. Charette, M. Grandbois; "*Label-free visualization and quantification of single cell signaling activity using metal-clad waveguide (MCWG)-based microscopy*"; Biosensors and Bioelectronics, Volume 100, 2018, Pages 429-436, https://doi.org/10.1016/j.bios.2017.09.002.

Contribution of the manuscript

In this work, we demonstrate for the first time how metal-clad waveguide (MCWG) based microscopy can successfully visualize and quantify individual cell signaling activity. We apply this technique to follow individual endothelial cells undergoing apoptosis following TRAIL stimulation as well as the formation of extracellular gaps within a confluent endothelial monolayer due to the exposure to Thrombin.

Originality of the work

Using MCWG microscopy, we could successfully visualize and quantify cell-cell heterogeneity within population of endothelial cells following TRAIL induced apoptosis. We demonstrate that cells have a distinct threshold level and show how a combined signal from the overall population might not reflect the correct kinetic parameters. Further, the additional spatial information is used to automatically assess endothelial cell layer integrity and link intercellular features to the sensor signal.

Contributions by author

T. Söllradl did all the experimental work, the data analysis as well as writing of the manuscript. F. Banville helped with the sensor chip optimization and U. Fröhlich helped with the cell culture during the experiments. M. Canva, P. G. Charette, and Michel Grandbois supervised this work and helped with the review of the manuscript.

4.2 French Title:

Visualisation et quantification, sans marqueurs, de l'activité de cellule individuelle par l'utilisation de la microscopie sur guides d'ondes à gaine métallique (MCWG).

4.3 Abstract (French)

Les méthodes de biodétection sans marqueurs sont très efficaces pour l'étude de l'activation des cascades de signaux cellulaires déclenchées par des stimuli externes. Généralement, les expériences impliquent un grand nombre de cellules et reposent sur la prémisse que la réponse cellulaire est uniforme au sein d'une population cellulaire. Cependant, un nombre croissant d'indices tend à montrer que le comportement cellulaire peut varier de façon significative même parmi des cellules génétiquement identiques. Dans cet article, nous démontrons l'utilisation de la microscopie basée sur les guides d'ondes à gaine métallique (MCWG) sans utilisation de marqueurs. Cette méthode, permet de mesurer en temps réel l'activité de signalisation et les changements de morphologie dans une petite population de cellules tout en maintenant la possibilité d'observer des cellules individuelles. Nous démontrerons le potentiel de cette approche en quantifiant l'activité intracellulaire de cellules en situation d'apoptose induite. Pour ce faire, une couche de cellules endothéliales a été exposée à la cytokine TRAIL (tumor necrosis factor-related apoptosis-inducing ligand) et puis les changements dans l'intégrité de la couche ont été visualisés et quantifiés à la suite de l'activation par la thrombine du récepteur activé par la protéinase (PAR1). Les résultats montrent que la moyenne des signaux obtenus à partir d'une population cellulaire peut sous-représenter la variation réelle des paramètres de morphologie et de cinétique d'une population cellulaire qui peut être significative.

4.4 Abstract (English)

Label-free biosensing methods are very effective for studying cell signaling cascade activation induced by external stimuli. Assays generally involve a large number of cells and rely on the underlying assumption that cell response is homogeneous within a cell population. However, there is an increasing body of evidence showing that cell behavior may vary significantly even among genetically identical cells. In this paper, we demonstrate the use of metal-clad waveguide (MCWG)-based microscopy for label-free real-time monitoring of signaling activity and

morphology changes in a small population of cells, with the ability to resolve individual cells. We demonstrate the potential of this approach by quantifying apoptosis-induced intracellular activity in individual cells following exposure to tumor necrosis factor-related apoptosis-inducing ligand (TRAIL) and by visualizing and quantifying extracellular changes in endothelial cell layer integrity following the activation of the proteinase-activated receptor 1 (PAR1) by thrombin. Results show that averaged signals obtained from a cell population may incorrectly reflect the actual distribution of morphology and kinetics parameters across a cell population by a significant margin.

4.5 Introduction

Eukaryotic cells express a large diversity of membrane-bound receptors to sense and react to external stimuli such as hormones, cytokines, pathogens and toxins. The activation of these receptors triggers intracellular signaling events regulating cell activities supporting normal tissue and organ functions. The sensitive and non-invasive quantification of cell signaling responses is important in cell biology and pharmacology, and is the basis for many novel developments in biomedical diagnostics, using both commercially available systems and advanced research platforms. Example applications include monitoring of G-protein coupled receptor (GPCR) signaling [Schröder *et al.*, 2010; Scott & Peters, 2010], changes in cell activity induced by toxins and antigens [Chabot *et al.*, 2009; Hide *et al.*, 2002], apoptosis [Arndt *et al.*, 2004; Maltais *et al.*, 2012] and endothelial cell layer integrity [Benson *et al.*, 2013; Tiruppathi *et al.*, 1992]. Electrical impedance spectroscopy [Tiruppathi *et al.*, 1992], diffraction gratings [Fang *et al.*, 2006] and surface plasmon resonance [Chabot *et al.*, 2009; Giebel *et al.*, 1999; Jamil *et al.*, 2007; Peterson *et al.*, 2014; Wang Wang *et al.*, 2012; Yanase *et al.*, 2007, 2010] have been used very successfully to monitor and quantify cellular activity in vitro. These label-free platforms do not require the use of exogenous labels that may bias or interfere with the molecular processes under investigation.

Experiments are typically conducted on cell populations ranging from 100 to 4000 cells. As such, measurements represent a statistical average of what may actually be a highly heterogeneous cell response, possibly including multiple cellular phenotypes [Stolwijk *et al.*, 2015]. While cell populations are often assumed to respond homogeneously to a specific

biochemical stimuli, there is an increasing body of evidence showing that cell behavior varies significantly even among genetically identical cells [Samadani *et al.*, 2006; Slack *et al.*, 2008]. Such cellular phenotypic heterogeneity is central to physiological processes relying on lineage selection from distinct clonal population of progenitor cells [Altschuler & Wu, 2010] and during development [Bahar *et al.*, 2006; Colman-Lerner *et al.*, 2005; Raser & O'Shea, 2005; Samadani *et al.*, 2006]. However, label-free methods for sensing cell response and signaling events are unable to resolve single cell activity within a population and therefore cannot detect heterogeneity.

Evanescent-field based methods such as surface plasmon resonance (SPR) and metal clad waveguides (MCWG) [Nina Skivesen *et al.*, 2005] are label-free and highly sensitive to events occurring within a discrete volume above the sensor surface. These methods, which were originally applied in biosensing to monitor binding kinetics between surface-bound receptors and ligands in solution [Homola, 2003], have since been applied very successfully to study phenomena in a wide range of biological objects. When probing relatively thick microscopic objects such as cells, MCWG-based systems are advantageous compared to SPR owing to their capability for deeper probing into the sample while maintaining relatively high spatial resolution [Söllradl *et al.*, 2017]. Indeed, certain cell structures of interest may be located higher up in the cell body (ex: actin cytoskeletal components, > 100 nm; intracellular organelles, > 200 nm) than the effective probing range of conventional SPR systems (~200 nm for visible light systems). In both cases, advanced imaging systems are capable of resolving single cells.

In this paper, we propose a MCWG-based microscopy system designed to make sensitive real-time quantitative measurements of cellular activity in vitro with the ability to resolve individual cells, without the need for fluorescent labeling. The potential of the proposed system is demonstrated in two sets of experiments: 1) quantification of intracellular activity following the activation of apoptotic pathways in an endothelial cell model (EA.hy926) exposed to the tumor necrosis factor-related apoptosis-inducing ligand (TRAIL), and 2) quantitation of the disruption of a confluent endothelial cell monolayer (EA.hy926) resulting from the activation of the protease activated receptor 1 (PAR1) by thrombin. Though the cell populations in the experiments are too small to extract meaningful statistics, the results nevertheless show

convincingly how averaged signals obtained from a cell population may not accurately reflect the actual distribution of cell behavior characteristics across a population.

4.6 Materials and Methods

4.6.1 Imaging instrumentation and sensor chip design

The sensor chip design and optical imaging setup based on a high numerical aperture microscope objective (Figure 4.1) are detailed elsewhere [Söllradl *et al.*, 2017]. Briefly, light from a fiber coupled LED source (center wavelength: 470 nm) is focused in the back focal plane of the objective and emerges as a collimated beam at the front of the objective, incident onto the backside of the MCWG sensor chip. The lateral offset of the focal spot from the center in the back focal plane of the objective determines the angle of incidence/reflection of the collimated light to/from the chip. A polarizing beamsplitter separates the reflected light into two perpendicular polarization components for recording by CCD cameras (1392x1040, 12 bit, gray-

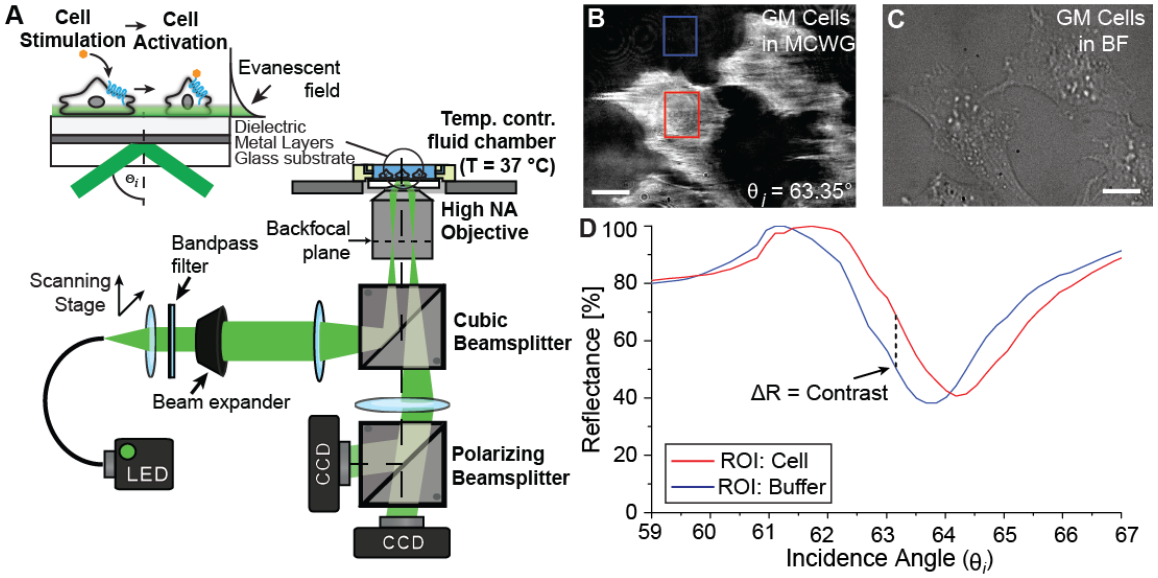

Figure 4.1: Metal clad waveguide imaging of individual cells. A) Schematic of the metal clad waveguide imaging (MCWG) setup based on a high numerical aperture microscope objective; B) Reflectance image of two glioblastoma cells (U251) cultured on top of the MCWG sensor chip (scale bar = 20 µm, LED center wavelength = 470 nm incidence angle of 63.35°); C) Brightfield image the same two cells (scale bar = 20 µm); D) Mean reflectance as a function of incidence angle for the two rectangular ROI shown in C). The vertical dotted line indicates the operating point (63.35°) for fixed-angle measurements.

scale), where TM images contain the reflectance-encoded refractive index map and TE images

correct for illumination field inhomogeneities. An LED was used as the light source instead of a laser to minimize coherence artifacts in the images and to prevent phototoxic effects.

Biosensing based on metal-clad waveguide (MCWG) is very similar to surface plasmon resonance (SPR). Indeed, SPR is actually a special case of this broader class of waveguides. MCWG and SPR sensors operate by resonant coupling of incident light to a lossy guided mode in a waveguide consisting of a thin film stack deposited on a glass substrate (the sensor chip), where the biological medium atop the chip acts as the topmost cladding layer of the waveguide. Cellular structures such as the membrane, cytoskeletal components, and organelles have higher refractive indices than the extracellular medium. As a result, when cells cultured atop a MCWG chip change either in morphology or in distribution of intracellular molecular content, the resulting local refractive index changes near the surface perturb the mode characteristics, thereby spatially modulating the reflected light intensity. Figure 4.1B shows a typical image of reflected light from a MCWG chip with two human glioblastoma cells (U251) on the top surface (brightfield microscopy image shown in (Figure 4.1C).

The exquisite depth discrimination in SPR and MCWG sensing/imaging results from the strong light confinement by the planar waveguide at the sensor surface. This waveguide-based nature, however, imposes a limit on the achievable imaging spatial resolution in the direction of mode propagation due to the finite decay length of the mode, which is generally greater than the diffraction limit. In the direction perpendicular to mode propagation, imaging spatial resolution is limited by diffraction as with conventional microscopy. There is a direct trade-off between spatial resolution and probing depth into the sample, where decreasing the probing depth will improve resolution and vice-versa [Söllradl *et al.*, 2017]. Though slightly more complex to fabricate, MCWG chips (dielectric core waveguides with a metal film acting as the bottom cladding at the waveguide/glass interface) yield greater design flexibility and range in the selection of an optimal resolution/depth trade-off operating point. In the present system, the optimal trade-off was determined to be a lateral resolution of ~5 μm in the direction of propagation and a 600 nm penetration depth into the sample volume.

In designing our system, our hypothesis was that an evanescent-field based method would be especially well-suited for label-free quantitative measurements of the reorganization of sub-cellular structures and signalling activities associated with cellular processes such as apoptosis. Indeed, the discrete volume above the sample surface probed by the evanescent-field which allows us to selectively image the cell/substrate interface together with a limited portion of the cytosol. This sensing region is assumed to be particularly rich in molecular events during cell signalling for it includes actin and focal adhesion remodelling, nuclear events such as chromatin decondensation and the reorganization of various organelles. As for spatial resolution in the plane of the sample surface, MCWG-based microscopy is capable of resolving information at the individual cell level, enabling us to study cell response heterogeneity across a small cell population. Though there is a slight decrease in spatial resolution along one axis in MCWG-based microscopy compared to conventional microscopy (bright field or phase-contrast) due to the finite decay length of the guided mode, this can be a worthwhile trade-off in the study of cell signaling activities. Indeed, in the case of apoptosis for example, the ability of MCWG-based microscopy to selectively image the cell/substrate interface with high contrast enables real-time monitoring of relevant signalling activities in individual cells, with direct cell-specific measurements of the duration of the latency phase and the rate of the reaction. In the case of phase-contrast microscopy, published works on apoptosis are mainly concerned with identifying cells undergoing apoptosis in a cell population [Haseyama *et al.*, 2006; Huh *et al.*, 2012]. Though phase-contrast yields high quality images showing extensive intracellular rearrangement, this method has not been applied so far to estimating kinetics parameters associated with cell signaling events such as the duration of the latency phase or the rate of the reaction.

Reflectance image sequences were acquired with the MCWG-based microscope at a fixed incidence angle, where the angular operating point was selected to maximize sensitivity and dynamic range (63.35°, as indicated by the vertical dotted line in Figure 4.1D). Reflectance values were averaged over regions-of-interest (ROI) in the images, as shown for example by the blue and red squares in Figure 4.1C for bare reference and cell-covered sensor areas, respectively. The corresponding curves of ROI mean reflectance as a function of incidence angle are shown in Figure 4.1D.

4.6.2Cell culture and reagents

Apoptosis and endothelium monolayer disruption were studied in an immortalized endothelial cell line (EA.hy926, kindly provided by Dr. CJ Edgell, University of North Carolina). Cells were maintained in DMEM supplemented with 10% temperature inactivated FBS and 60 U/ml penicillin in tissue culture petri dishes (100 mm diameter, Corning) and sub-cultured upon reaching 70 - 80% confluence using trypsin EDTA (0.25 %), typically within three days. Unless indicated otherwise, all cell culture supplements were purchased form Wisent (Canada). In the experiments, 5.75 x 10^5 cells were seeded onto uncoated ethanol-sterilized MCWG sensor chips and were either used at low density in the case of apoptosis experiments or grown to full confluence typically within two days for the monolayer disruption experiments. KMPR resin was used as the topmost waveguiding core layer of the MCWG sensor chips, forming a hydrophilic biocompatible protection layer above the silver metal layer. Silver, in contrast to the more commonly used gold layer in SPR, yields higher measurement sensitivity particularly at shorter wavelengths (< 500 nm) and offers a better trade-off between lateral resolution and penetration depth [Söllradl *et al.*, 2017]. Cells were found to have a similar growth rate and morphology on the sensor chips relative to conventional polystyrene culture dishes.

A typical experiment was performed as follows: cells were washed twice and culture media was replaced by warm CO_2-independent Leibovitz's L-15 medium supplemented with 60 U/ml penicillin. The MCWG chip was mounted in the imaging instrument fluid chamber (Vacucell, C&L Instruments) and maintained at 37 °C by a heating system (TC1, Bioscience Tools). Prior to stimulation, cells were left in the buffer solution for one hour to stabilize. At the start of each experiment, a full angular scan was performed to select the optimal angular operating point for maximum image contrast. Images were then acquired at this fixed incidence angle throughout the experiments.

Apoptosis was induced by injection of 10x TRAIL stock solution (Millipore, 250 ng/ml final concentration after dilution). Endothelium monolayer activation was induced by injection of 10x thrombin stock solution (Sigma-Aldrich, 10 U/ml final concentration after dilution). Control experiments were conducted in buffer solutions: HBSS with TWEEN for TRAIL and sterile DI water with 0.1% BSA for thrombin.

4.6.3Image analysis

During experiments, images were acquired for each polarization channel every 5 seconds for the shorter endothelium monolayer disruption experiments and every 15 seconds for the longer apoptosis experiments.

In the apoptosis experiments, kinetics parameters were estimated separately for each individual cell in the field of view. Region-of-interest (ROI) contours were drawn manually around individual cells to calculate mean reflectance time series on a cell-by-cell basis throughout an image sequence. To extract the kinetics parameters for a particular cell, its ROI reflectance time series were first fitted with a sigmoid function. A linear model was then fitted to the data near the mid-point of the sigmoid function to estimate the transition slope (maximum rate of the apoptosis execution phase). To estimate the duration of the pre-execution latency phase, a horizontal line was fitted to the initial (baseline) portion of the data, where the intersection between the two linear models identified the onset time of the execution phase.

In the endothelial cell layer integrity experiments, the disruption of the confluent monolayer was characterized by analysing the dynamics of the inter-cellular gaps. This analysis proceeded by automated segmentation of image pixels into intra- vs extra-cellular zones to quantify gap size changes throughout an image sequence. The analysis consisted of applying the following automated steps to each image in a sequence:

1. Background subtraction of the Gaussian-filtered (100x100 kernel, $\sigma = 4$) TE-polarized initial image.
2. Conversion of the image to binary using automatic clustering-based thresholding [Otsu, 1979] using the graythesh() Matlab function.
3. Morphological processing by a circular structuring element to coalesce fragmented intra- and extra-cellular zones into connected areas (erosion with radius = 8 pixels, followed by dilation/erosion with radius = 2 pixels) using the imerode() and imclose() Matlab functions.
4. Thresholding of spurious gaps based on minimum acceptable gap size (100 pixel area) using the bwareaopen(), bwconncomp(), and regionprops() Matlab functions.

4.6.4 Statistics

In the apoptosis experiments, results (TRAIL vs. control) were compared for equality of variances using a 2-sided F test and showed unequal variances. To draw reliable conclusions, an independent-samples t-test assuming unequal variances was used to test for significance. Mean values are expressed as standard deviation (SD) and p-values < 0.05 were considered significant.

4.7 Results and discussion

4.7.1 Monitoring of cell response heterogeneity to an extrinsic apoptotic stimulus

Visualization of single cell apoptosis by MCWG microscopy

Even in cells sharing an identical genetic background, individual response to physiological, pathophysiological or pharmacological stimuli is often assumed to be heterogeneous within a population [Lahav *et al.*, 2004]. While this response heterogeneity may simply reflect slight variations from the average phenotypic state of a given cell population, it can also be linked to an amalgam of phenotypically distinct subpopulations, where individual cells are characterized by a distinct sensitivity threshold to an external stimulus. This effect is often observed in cancer cell populations [Gascoigne & Taylor, 2008; Slack *et al.*, 2008] and is linked to the establishment of cell populations refractory to treatment. Such characteristics are particularly important when trying to assess the fate of a global cell population exposed to apoptotic stimuli inducing cell death.

Apoptosis is a two-stage process characterized by a sequence of specific intracellular molecular events ultimately leading to cell death. In its first stage, apoptosis involves the targeted activity of initiator caspases toward executioner caspase activation, which in turn are responsible for extensive cleavage of intracellular proteins and ultimately cell death [Melino & Vaux, 2010]. Since initiator caspases are not directly involved in protein cleavage, their activation is normally seen as a “latency phase” lasting up to several hours [Maltais *et al.*, 2012], typically showing little or no signal response in label-free monitoring systems. In contrast, the execution phase typically produces a robust sensor response resulting from the significant perturbation of the

cellular architecture due to the extensive cleavage of intracellular proteins, including collapse of the nucleus, extensive cytoskeleton reorganization and cleavage of focal adhesion sites [Häcker, 2000; Wen *et al.*, 1997]. Most current methods of studying apoptosis are based on fluorescence markers: these include the annexin-V assay to measure phosphatidylserine externalization [Koopman *et al.*, 1994] and the fluorescent TUNEL assays detecting DNA fragmentation [Gorczyca *et al.*, 1993]. Recently, we showed that label-free methods like SPR can also reliably quantify apoptosis in a cell population and provide results consistent with validated biochemical assays [Maltais *et al.*, 2012, 2016].

In the experiments presented here, the tumor necrosis factor-related apoptosis-inducing ligand (TRAIL) was used to stimulate cell death receptors 4-5 (DR4-5) in EA.hy926 endothelia cells. Figure 4.2A–D show an example time sequence of images acquired after stimulation of EA.hy926 cells with TRAIL, where individual cell ROIs are outlined in the images. Figure 2A shows the reference reflectance image at 0 min immediately following TRAIL injection, where the cells in the field of view are numbered 1 through 6. Figure 4.2B–D show color-coded maps of % reflectance differences with respect to the reference image. During the latency phase, localized reflectance variations can be observed within individual cells, both positive and negative Figure 4.2B at 105min). Since control experiments showed much lower and more homogeneous reflectance changes during this phase, these small signal variations could reflect intra-cellular activity such as initiator caspase activity. Reflectance images recorded at 150 min (Figure 4.2C) and 250 min (Figure 4.2D) show a gradual shift towards larger, negative reflectance changes with respect to the reference, at first in isolated areas and eventually extending throughout the entire cells. These large reflectance changes are consistent with executioner caspases activity associated with extensive cleavage of intracellular proteins, resulting in the collapse of intracellular structures and ultimately the loss of cell-substrate contact.

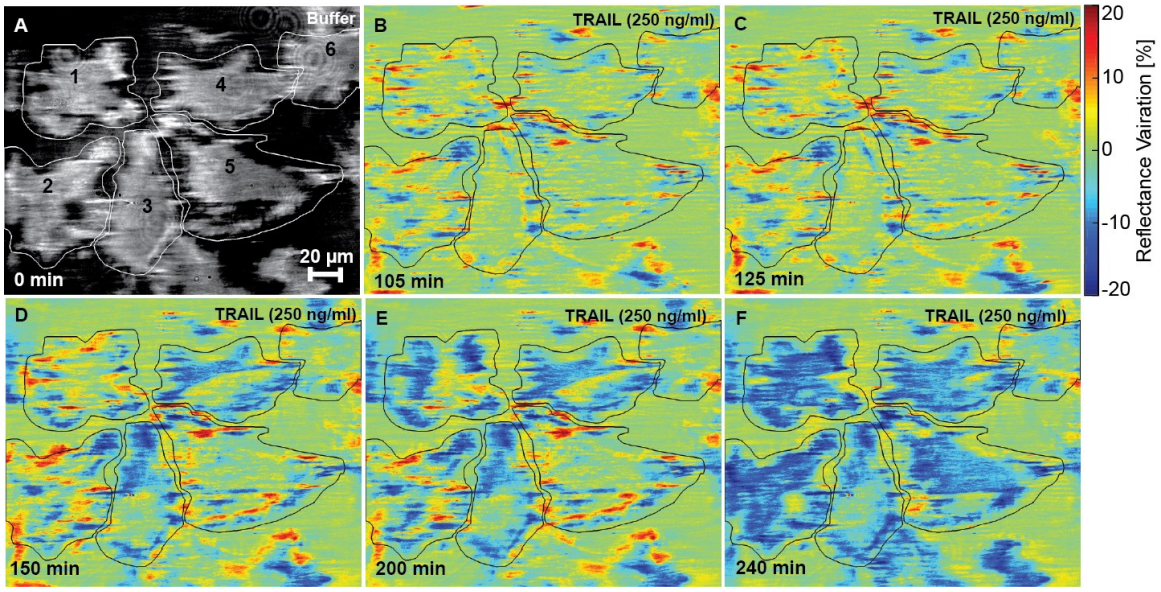

Figure 4.2: MCWG images of cell response heterogeneity to an extrinsic apoptotic stimulus (TRAIL). A) Reference reflectance image showing six EA.hy926 cells on the MCWG sensor surface ; B – D) Color-coded reflectance variation images showing localized changes in the cells at 105 min, 125 min, 150 min, 200 min, and 240 min. Reflectance variations expressed as % change with respect to reference reflectance levels (A).

Single cell apoptosis parameters

Plots of mean reflectance variations for each cell across the entire experiment are shown in Figure 4.3A. As expected for the latency phase, mean reflectance remains relatively constant. At approximately 125 min, cells #3 and #4 show a sharp drop in reflectance that is consistent with executioner caspases activity. This same drop appears at later times for cells #1, #2 and #5, and its onset is only just observable for cell #6. Figure 3B shows the results of the sigmoid-based fitting and parameter extraction described above applied to the cell reflectance data to estimate onset time and maximum rate of signal change for the execution phase. Both Figure 4.3A and B reveal marked differences in individual cell response and indicate heterogeneous cell sensitivity to TRAIL stimulation. Indeed, the onset of the execution phase ranged from 117.1 min to 205.3 min (average of 154.4 ± 34.5 min) and the rate of reflectance change ranged from -0.139 %/min to -0.487 %/min (average of -0.305 ± 0.138 %/min).

Figure 4.3C clearly illustrates how measurements averaged over a cell population (albeit a small one in this demonstration) yield quite different, possibly misleading, results. The figure shows

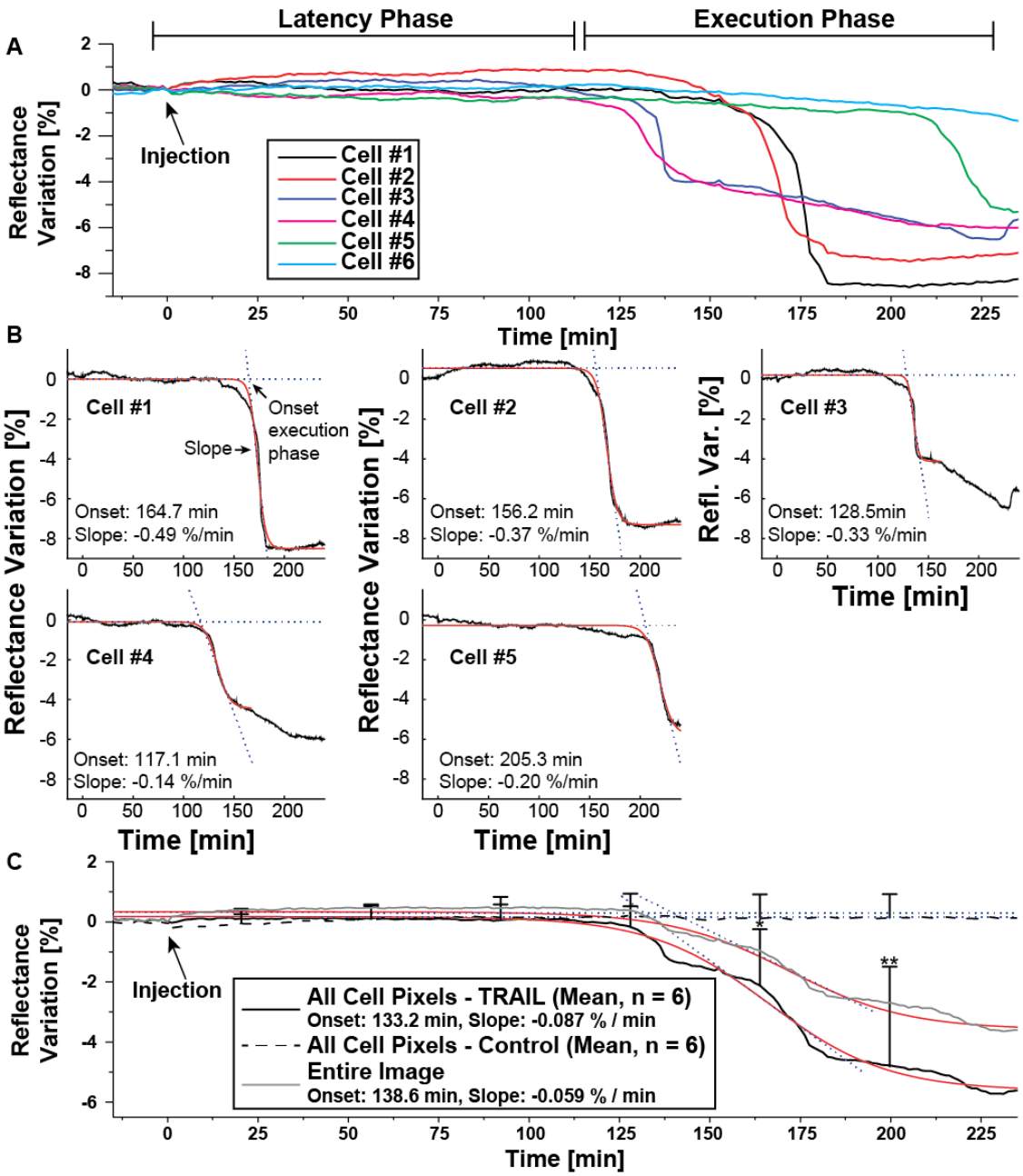

Figure 4.3: Apoptosis kinetics – mean reflectance variation time series. A) Mean reflectance variation for the individual cells outlined in Figure 4.2 as a function of time; B) Extraction of individual cell apoptosis kinetics parameters (onset time, slope) from the time series in A based on the sigmoid fit (red curve) and two linear fits (blue dotted lines); C) Plots of whole image averages compared with negative control (buffer without TRAIL), compared by an independent samples t-test assuming unequal variances (*: $p < 0.05$, **: $p < 0.01$). Error bars represent standard deviation (SD). Reflectance variation are expressed as % change with respect to reference reflectance levels at the start of the experiments.

a control (gray trace) and plots of average reflectance as a function of time calculated in two

ways: cell pixels only (solid black trace) and all image pixels (dashed trace). The average reflectance curves show a staircase structure resulting from the superposition of the asynchronous cell responses. In the case of cell pixel only averages (delimited by the ROI), the fitted onset (133.2 min) and rate (-0.087 %/min) parameters are markedly different from the true averages calculated above (154.4 min and -0.305 %/min). The discrepancy in the rate parameter is even greater when pixels from the entire image are averaged (-0.059 %/min). Such marked differences in rate and synchronicity show that these parameters may be poorly estimated from measurements averaged over a cell population.

Figure 4.4 shows a slightly different analysis of the cell-specific ROI reflectance changes across the image sequence compared to Figure 4.3A. In Figure 4.4, the mean of the absolute values of reflectance changes is plotted as a function of time for the individual cells, as opposed to the mean reflectance change shown in Figure 4.3A. Because the small reflectance changes during the latency phase inside the cells are both positive and negative (Figure 4.2B), the mean is close to zero. Interestingly, the absolute value of localized variations reveals a steady increase in cell activity until the executioner phase. Such behavior is consistent with initiator caspase enzymatic activity commonly monitored using selective fluorescent reporters which also show a steady signal increase until the sharp activation of the executioner caspase activity [Albeck *et al.*, 2008]. Overall, these results show that measurements obtained from conventional label-free assays without spatial distribution information in a cell population may not necessarily reflect the true characteristics of a given cellular process in individual cells.

Thus MCWG microscopy could be useful in identifying cell response heterogeneity to various apoptotic stimuli, such as in acquired resistance to pro-apoptotic drugs observed in cancer cells [Gascoigne & Taylor, 2008; Slack *et al.*, 2008] or under pathological conditions where small numbers of overly sensitive cells could be responsible for a general drift in cell phenotype [Bombeli *et al.*, 1997].

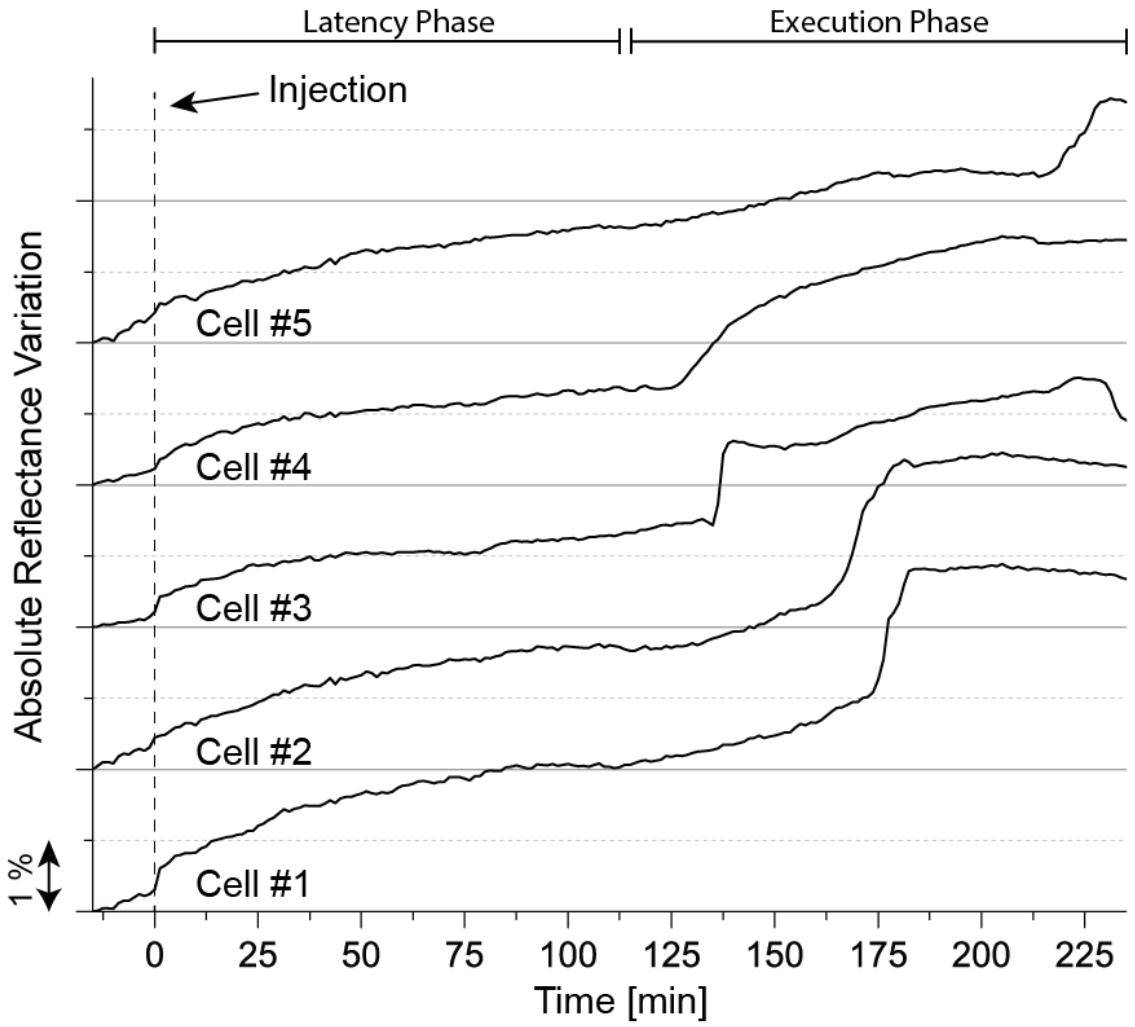

Figure 4.4: Apoptosis kinetics – mean absolute value of reflectance variation time series. Mean absolute value reflectance variation as a function of time over the course of the experiment for the individual cells outlined in Figure 4.2. In contrast to the previous figure, the plots show a visible signal change over time during the latency phase. Reflectance variation is expressed as % change with respect to reference reflectance levels at the beginning of the experiments.

4.7.2 Spatially-resolved monitoring of confluent endothelial cell monolayer integrity

Visualization of endothelial cell monolayer integrity following PAR1 activation

Endothelial cell monolayer integrity and the modulation of tight cellular interconnections are an important indicator of cell phenotype and function [Wegener & Seebach, 2014]. The current gold standard for label-free monitoring of endothelium cell monolayer integrity is based on

measurements of trans-endothelial electrical resistance (TEER) in response to both intercellular and intracellular cell activity [Birukova *et al.*, 2004; McLaughlin, 2005; Tiruppathi *et al.*, 1992; Wegener & Seebach, 2014]. TEER measurements, however, yield measurements averaged over an entire monolayer and the electrode requirement makes it virtually impossible to obtain the spatial resolution required to resolve individual gap formation within the monolayer. In order to obtain spatial distribution information on cell monolayer integrity, this technique must be supplemented with fluorescence microscopy measurements [Birukova *et al.*, 2004; McLaughlin, 2005].

To demonstrate the capability of our system to quantify and spatially-resolve monolayer integrity, an EA.hy 926 endothelial cell monolayer was grown to confluence on sensor chips. The cell proteinase-activated receptor 1 (PAR1) was stimulated with 10 U/ml thrombin to disrupt cell-cell contact and cell-substrate adhesion, resulting in intercellular gap formation [Coughlin, 2000]. Gap size changes were monitored over time throughout the experiments using the automated image processing procedure described above. Reflectance images at the start of an experiment (Figure 4.5A) show a near-confluent endothelial cell monolayer where gaps appear in black, outlined in white boundaries identified by the image-processing algorithm. At around 12.5 minutes after PAR1 activation (Figure 4.5B), intercellular gaps can be seen to increase in size due to localized disruptions in endothelial tight junctions. As the process continues (Figure 4.5C: 15 min, 5D: 17.5 min, 5E: 20 min, Figure 4.5F: 30 min), the overall monolayer morphology is extensively altered with large intracellular gaps appearing. Here again, significant heterogeneity in gap formation across the cell monolayer is evident.

Quantification of endothelial cell monolayer integrity

The image sequence data were analyzed to quantify both the evolution of individual gap size and total gap area over time. Figure 4.5G shows a plot (gray line) of total gap area over time, expressed as a percentage change from the total gap area in the initial near-confluent monolayer (Figure 4.5A). As seen in the plot, total gap area increases steadily from about 12.5 min onwards and reaches a maximum plateau close to 60% after about 25 minutes. These results, which are consistent with TEER measurements found in the literature for similar experiments, demonstrate how MCWG-based microscopy can be used to spatially resolve dynamics in gap formation and

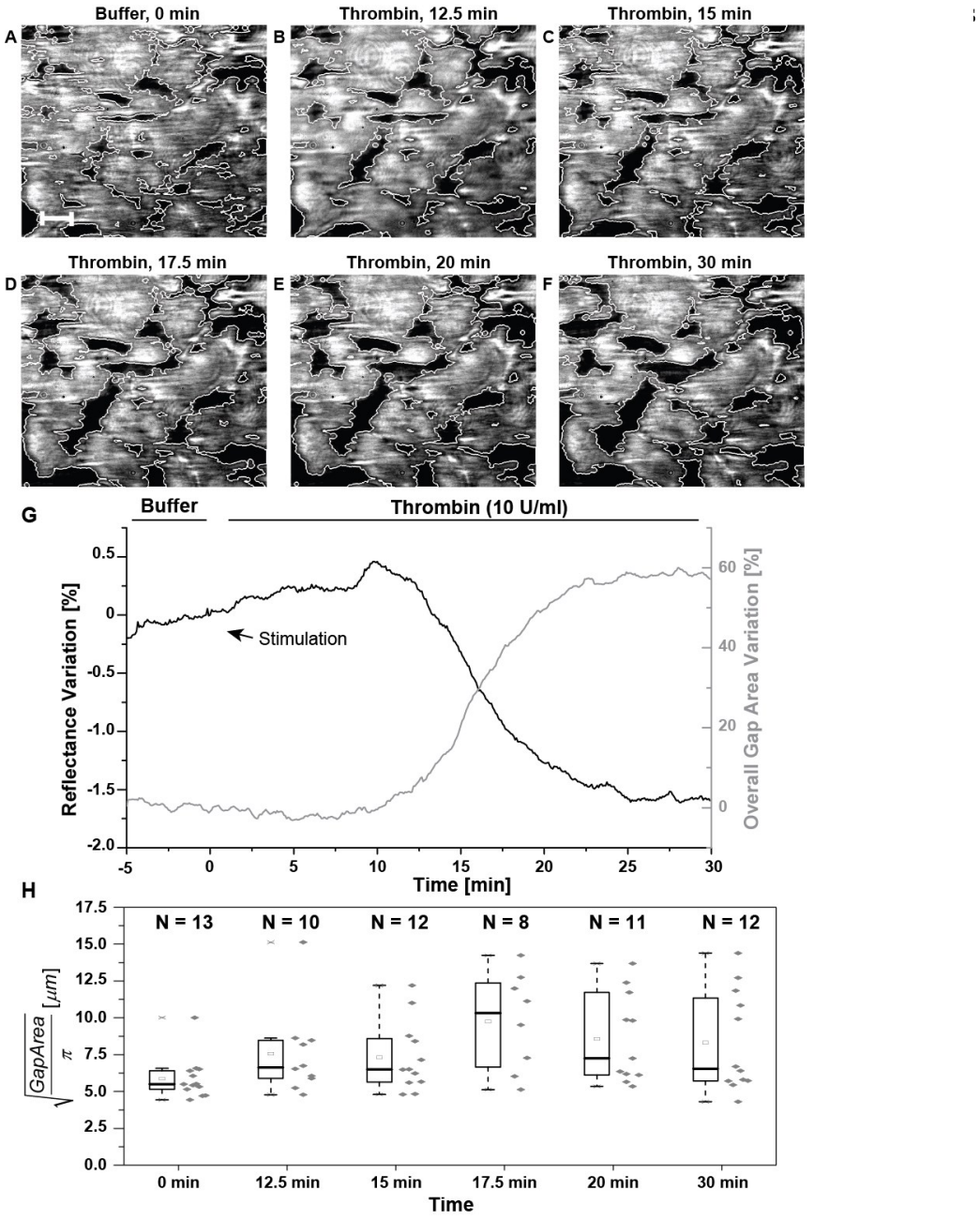

Figure 4.5: Spatially-resolved monitoring of confluent endothelial cell monolayer disruption. A) Reflectance image of near-confluent endothelium cell monolayer prior to the injection of thrombin (scale bar = 20 μm); B) – F) Reflectance images captured at 12.5 min, 15 min, 17.5 min, 20 min, and 30 min illustrating the evolution of intercellular gaps and cell morphology changes. The white outlines show gap areas detected automatically by image processing; G) Plot (dark gray line) of total gap area variation over time expressed as a percentage change from initial total gap area and plot of mean image reflectance over time (black line); H) Box plot and scatter plot showing the evolution of time of "large gap" size distribution (gaps having radii > 4 μm, assuming grossly circular shape, where N is the number of individual gaps tabulated in each vertical scatter plot). Whiskers represent 1.5x interquartile range.

biomarkers. Figure 4.5E also shows a plot of mean image reflectance variation over time (black line) that is inversely correlated with total gap size, as expected. Note that equivalent results of a negative control experiment from an EA.hy 926 cell monolayer of similar confluence stimulated with buffer solution only are given in Supplementary Figure 2, where the total gap size changes by around 1% over the course of the experiment.

Gap size geometry and dynamics are especially significant in the context of tracking changes in cell monolayer permeability. Most common permeability assays rely on the specific labeling of certain cell-cell and cell-substrate molecules and subsequent imaging by fluorescence microscopy [Seebach *et al.*, 2015] or rely on the diffusion of secondary molecules through the cell monolayer [Wegener & Seebach, 2014]. To the best of our knowledge, no label-free assay exists that allows for the direct visualization and quantification of endothelial cell monolayer integrity without the need for any secondary marker. To demonstrate these capabilities in MCWG-based microscopy for this application, we measured inter-cellular gap size statistics over time, focusing on larger gaps since they strongly impact monolayer permeability. The radius threshold for "large" gaps was set at 4 μm (assuming a roughly circular shape) to maximize the visibility of size distribution (the majority of gaps are small so that a lower threshold compressed and homogenized the scatter plots). Figure 4.5H shows large gap size distribution sampled at the image timestamps of Figure 4.5A-F, where N in each vertical scatter plot is the number of tabulated gaps. As seen in the figure, there is a marked heterogeneity in large gap size in the latter part of the experiment when the cell monolayer is significantly disrupted. These results indicate that an average gap measurement, on its own, may actually underestimate the size of particles that can make it through a disrupted monolayer, thus underestimating true permeability.

4.8 Conclusion

In this work, we demonstrated the use of MCWG microscopy as a label-free technique for spatially-resolved monitoring of signaling activity and morphological changes in individual cells in a small cell population. In a first series of experiments using an extrinsic apoptosis model, we showed the method's capabilities to: 1) highlight the heterogeneous response of a cell population, and 2) spatially resolve the intracellular mass redistribution associated with the

activation of apoptotic pathways in individual cells. In a second series of experiments monitoring endothelial layer integrity following stimulation by thrombin, we showed that: 1) the method produces label-free averaged signals consistent with established TEER permeability assays, 2) averaged signals are correlated with overall variations in intercellular gap size, and 3) size distribution for larger gaps may be significantly heterogeneous in a disrupted monolayer.

Though the cell populations in the experiments were too small to extract meaningful statistics, our results nevertheless convincingly demonstrate how averaged signals in a conventional assay may incorrectly reflect the actual distribution of kinetics parameters across a cell population by a significant margin. This effect is believed to be particularly important when dealing with primary cellular models that are often difficult to culture at high purity and density and are characterized by low proliferation rates and high phenotypic variability, such as neurons and stem cells. In this context, an obvious advantage procured by our system is the elimination of the dependence of the response profile on the degree of cell confluence when studying low density cell populations. We believe that this approach could be very useful in many applications such as drug screening to assess the heterogeneous sensitivity of a given cell phenotype or to assess the resistance of subpopulation of cells to drugs.

4.9 Acknowledgements

We wish to thank Prof. Jean-Bernard Denault for his support and helpful discussions with the apoptosis experiments. This work was made possible by the financial support of the Fonds de recherche du Québec – Nature et technologies (FRQNT: MG, PGC, TS) as well as the Natural sciences and engineering research council of Canada (NSERC: MG, PGC, MC) and the Canadian Institutes of Health Research (CIHR) under the Collaborative Health Research Program (MG, PGC). LN2 is an international research laboratory co-managed in Canada by University of Sherbrooke, and in France by CNRS, Université de Lyon (Centrale Lyon, INSA Lyon et CPE Lyon) as well as Université Grenoble-Alpes; it is also funded by Québec thought the FRQNT, Fonds de Recherche du Québec en Nature et Technologies. TS was also supported by the COMET K1 center Austrian Smart Systems Integration Research (ASSIC). The COMET Competence Centers for Excellent Technologies Program is supported by BMVIT, BMWFW and the federal provinces of Carinthia and Styria of Austria.

CHAPTER 5 Monitoring Individual Cell Signaling Activity Using Combined Metal-Clad Waveguide and Surface Enhanced Fluorescence Imaging

5.1 Overview of Article

Authors and affiliations:

Thomas Söllradl: PhD student, Laboratoire Nanotechnologies Nanosystèmes (LN2)- CNRS UMI-3463, Institut Interdisciplinaire d'Innovation Technologique (3IT), Département de Pharmacologie et Physiologie, Université de Sherbrooke, Sherbrooke, Canada

Kevin Chabot: MSc student, Laboratoire Nanotechnologies Nanosystèmes (LN2)- CNRS UMI-3463, Institut Interdisciplinaire d'Innovation Technologique (3IT), Université de Sherbrooke, Sherbrooke, Canada

Ulrike Fröhlich: Research Assistant, Département de Pharmacologie et Physiologie, Institut de Pharmacologie de Sherbrooke, Université de Sherbrooke, Sherbrooke, Canada

Michael Canva: Professor, Laboratoire Nanotechnologies Nanosystèmes (LN2)- CNRS UMI-3463, Institut Interdisciplinaire d'Innovation Technologique (3IT), Université de Sherbrooke, Sherbrooke, Canada

Paul G. Charette: Professor, Laboratoire Nanotechnologies Nanosystèmes (LN2)- CNRS UMI-3463, Institut Interdisciplinaire d'Innovation Technologique (3IT), Université de Sherbrooke, Sherbrooke, Canada

Michel Grandbois: Professor, Laboratoire Nanotechnologies Nanosystèmes (LN2)- CNRS UMI-3463, Département de Pharmacologie et Physiologie, Institut de Pharmacologie de Sherbrooke, Université de Sherbrooke, Sherbrooke, Canada

State of the article: Accepted Manuscript; Submitted on the 16.05.2018 to the journal *Analyst*
Complete Reference: T. Söllradl, K. Chabot, U. Fröhlich, M. Canva, P. G. Charette, M. Grandbois; "*Monitoring Individual Cell Signaling Activity using Combined Metal Clad Waveguide and Surface Enhanced Fluorescence Microscopy*";

Contribution of the manuscript

In this manuscript, a combined imaging platform is described that allows for simultaneous label-free and label-based monitoring down to the single cell level. The application of two distinct modalities, namely label-free MCWG and the label-based surface enhanced fluorescence microscopy, reveals the underlying molecular and structural contributions associated with label-free sensor signals. Using such an imaging approach enables the detection of cell-cell phenotypic variability within a cell population.

Originality of the work

This is, to the best of our knowledge, the first time that a combined MCWG and SEF imaging platform is described in the scientific literature. We demonstrate the capabilities of this platform in the context of cell based biosensing by the visualization of actin cytoskeleton components in vascular smooth muscle cells. In a second set of experiments, we use the system to monitor the response resulting from Angiotensin 1 receptor (AT1R) activation by its agonist Angiotensin II in HEK293 cells. In this application, the SEF signal allows us to reliably extract the intracellular calcium signal following AT1R activation while the MCWG signal yields the overall functional cell response. Using a specific pharmacological inhibitor, we can inhibit intracellular signaling pathways associated with AT1R activation and our results suggest that $G_{12/13}$ signaling activity is needed for the initial phase of the MCWG signal.

Contributions by author

T. Söllradl did all the experimental work, the data analysis as well as writing of the manuscript. K. Chabot helped with the optical setup as well as with the fabrication of the sensor chips. U. Fröhlich helped with the cell culture during the experiments. M. Canva, P. G. Charette and Michel Grandbois supervised this work and helped with the review of the manuscript.

5.2 French Title:

Suivi individuel de l'activité de signalisation cellulaire par une utilisation combinée de guides d'ondes à gaine métallique et de microscopie à fluorescence exaltée en surface

5.3 Abstract (French)

Les systèmes de biocapteurs à champs évanescents basés sur la résonance des plasmons de surface (SPR), les réseaux de diffraction ou les guides d'ondes à gaine métallique (MCWG) sont des outils puissants pour suivre en temps réel l'activité de signalisation de cellules vivantes exposées à des hormones, agents pharmacologiques ou toxines. Comparativement à la SPR, l'imagerie basée sur les MCWG est particulièrement bien adaptée à l'étude d'objets relativement épais, tel une cellule, en raison de sa plus grande profondeur de pénétration dans le milieu d'analyse. Les méthodes dites « sans marqueurs » fournissent toutefois une mesure indirecte puisque le signal mesuré est issu d'un changement local des propriétés physiques du milieu plutôt que de la présence d'une cible moléculaire spécifique. Dans le cas d'une cellule, la situation est particulièrement complexe car la mesure du signal sans marqueur peut provenir d'une combinaison de sources variées, par exemple, des changements morphologiques, une réorganisation intra-cellulaire, des évènements moléculaires en cascades, l'expression de protéines, etc. Par conséquent, la déconvolution des contributions individuelle d'évènements spécifiques du profil de réponse cellulaire global peut être difficile. Nous présentons une plateforme d'imagerie cellulaire combinant deux modes de détection distincts, à savoir l'imagerie MCWG (sans marqueur) et la fluorescence exaltée en surface (SEF) à base de marqueurs fluorescents. La plateforme a été conçue afin de faciliter l'identification des contributions moléculaires et structurelles sous-jacentes observées en imagerie MCWG. Nous démontrons les capacités bimodales de cette plateforme d'imagerie par des expériences conçues pour visualiser l'organisation du cytosquelette d'actine dans les cellules musculaires lisses vasculaires. Nous avons ensuite suivi, en temps réel, la réponse des cellules HEK293 exprimant le récepteur de l'angiotensine 1 (AT1R), lorsqu'il est stimulé par l'agoniste du récepteur angiotensine II (AngII). Le signal sans marqueur obtenu en imagerie MCWG et le signal de calcium intracellulaire résultant de l'activation de AT1R mesuré par SEF ont été obtenus simultanément. L'analyse de ces signaux simultanés permet de relier des éléments du signal sans marqueur aux structures spécifiques liés à l'activation du récepteur. Nos résultats montrent

que les taux de calcium intracellulaire, normalement observés suite à l'activation de AT1R, ne sont pas requis par l'activité cellulaire subite observée dans le signal MCWG, mais indiquent plutôt une activité de signalisation impliquant la kinase intracellulaire ROCK.

5.4 Abstract (English)

Evanescent field based biosensing systems based on surface plasmon resonance (SPR), diffraction gratings, or metal-clad waveguides (MCWG) are powerful tools for label-free real-time monitoring of signaling activity of living cells exposed to hormones, pharmacological agents, and toxins. In particular, MCWG-based imaging is well suited for studying relatively thick objects such as cells due to its greater depth of penetration into the sensing medium, compared to SPR. Label-free methods, however, provide only indirect measurements in that the measured signal arises from local changes in material properties rather than from specific biomolecular targets. In the case of cells, the situation is especially complex as the measured label-free signal may result from a combination of very diverse sources: morphological changes, intra-cellular reorganization, cascaded molecular events, proteins expression etc. Consequently, deconvolving the contributions of specific sources to a particular cell response profile can be challenging. In the following, we present a cell imaging platform that combines two distinct sensing modalities, namely label-free MCWG imaging and label-based surface enhanced fluorescence (SEF), designed to greatly facilitate the identification of the underlying molecular and structural contributions to the label-free MCWG images. We demonstrate the bimodal capabilities of this imaging platform in experiments designed to visualize actin cytoskeleton organization in vascular smooth muscle cells. We then monitored the real-time response of HEK293 cells expressing the Angiotensin 1 receptor (AT1R), when stimulated by the receptor agonist Angiotensin II (AngII). The analysis of the simultaneous label-free signal obtained by MCWG and the intracellular calcium signal resulting form AT1R activation, measured by SEF, allows relating label-free signal features to specific markers of receptor activation. Our results show that the intracellular calcium levels normally observed following AT1R activation are not required for the initial burst of cellular activity observed in the MCWG signal but rather indicates signaling activity involving the intracellular kinase ROCK.

5.5 Introduction

Eukaryotic cells express a wide variety of structural and functional components to fulfill their tasks and maintain tissue and organ functions. For example, the cytoskeleton of smooth muscle cells generates and maintains forces to regulate vascular tone or engage in rhythmic, synchronized contractions [G K Owens, 1995]. To sustain individual cell activity associated with physiological functions, cells express a wide variety of membrane-bound receptors that respond to a wide variety of external biochemical stimuli. The largest class of such receptors is the G-protein-coupled receptor (GPCRs), which control a variety physiological processes including cell-cell communication, vascular tone, hormonal signaling, and neuronal transmission [Palczewski *et al.*, 2000]. The reliable detection aFnd quantification of GPCR activity is of great interest in the fields of cellular biology and pharmacology.

Cell-based assays using a variety of label-free transduction methods such as diffraction gratings [Fang *et al.*, 2006], electrical impedance [Tiruppathi *et al.*, 1992], and surface plasmon resonance [Chabot *et al.*, 2009; Giebel *et al.*, 1999; Jamil *et al.*, 2007; Peterson *et al.*, 2014; Wang *et al.*, 2012; Yanase *et al.*, 2007, 2010b] have been proposed to study cell-signaling with no need for exogenous markers. More recently, a more flexible type of evanescent field biosensor based on metal clad waveguides (MCWG) has been used in sensing applications with cells and bacteria to probe deeper into the cell body [Nina Skivesen *et al.*, 2005; Söllradl *et al.*, 2017] than is possible with SPR (typically 200 nm or less for visible and near-IR systems). Using appropriate optics, SPR and MCWG can be used for imaging and advanced systems are capable of resolving intracellular structures. Our group and others have demonstrated this capability in a variety of cell-substrate interaction experiments [S.-H. Kim *et al.*, 2011; Peterson *et al.*, 2014; Söllradl *et al.*, 2018], in particular to provide insight into the heterogeneous response of a cell population undergoing apoptosis [Söllradl *et al.*, 2018]. Note that spatial resolution in SPR and MCWG images is limited along the direction of light propagation by the finite mode attenuation length, rather than by diffraction [Banville *et al.*, 2015; Yeatman, 1996]. Furthermore, there is an intrinsic trade-off between mode attenuation length and penetration depth into the sensing medium such that any increase in penetration depth comes at the expense of a commensurate decrease in imaging spatial resolution. Compared to SPR, MCWG offers the better compromise between spatial resolution and penetration depth [Söllradl *et al.*, 2017].

Hence, when imaging relatively thick objects such as eukaryotic cells or bacteria, this tradeoff is especially relevant and MCWG-based imaging is preferred.

Since SPR and MCWG are label-free methods, they yield direct information on local changes in material properties (in this case the refractive index), rather than on specific molecular targets. As with all label-free methods, however, it can sometimes be challenging to unambiguously identify molecular targets or cell structures from the image data. Indeed, though various SPR-based imaging experiments have been applied to study cellular structure and functional activity, few studies have attempted to identify the particular subcellular structures involved [Chabot *et al.*, 2013; Cuerrier *et al.*, 2008; He *et al.*, 2010; Peterson *et al.*, 2009, 2014]. Some of the most successful attempts involve separate corroborating experimental measurements with conventional fluorescence microscopy to identify a-posteriori the cellular features in the label-free micrographs [Peterson *et al.*, 2009, 2014].

Image fusion methods attempt to provide the best of both worlds by combining distinct imaging modalities, ideally in a single instrument, such as with simultaneous atomic force microscope and confocal fluorescence microscopy. Evanescent field based methods such as MCWG and SPR are capable of simultaneous label-free and fluorescence imaging, where the evanescent field in the dielectric can be used to excite fluorescent markers near the surface in a manner similar to total internal reflection fluorescence (TIRF) microscopy. Furthermore, the resonant coupling to the guided surface mode in MCWG and SPR produces a significant field enhancement in the sensing medium compared to TIRF, as demonstrated with surface plasmon enhanced fluorescence (SPEF) [Liebermann & Knoll, 2000]. Indeed, SPEF has been shown to increase detection sensitivity in classic fluorescence-based biomolecular assays by orders of magnitude [Yao *et al.*, 2004]. More recently, our group and others applied SPEF in cell sensing to identify the specific cellular processes underlying an SPR response [Chabot *et al.*, 2013; He *et al.*, 2006, 2009].

In this work, we introduce the first microscopy platform to combine MCWG and surface-enhanced fluorescence (SEF) imaging, a method we term “MCWG-SEF microscopy”. Relative to SPR, the enhanced probing depth of MCWG enables simultaneous label-free and

fluorescently-labeled imaging of cellular structures further up into the cell body, while the improved trade-off between resolution and probing depth maximizes the achievable spatial resolution. A first series of validation experiments are presented where actin stress fibers are simultaneously imaged by MCWG and SEF in vascular smooth muscle cells (VSMC). A second series of experiments is presented showing intracellular signaling associated with the activation of AT1R by its agonist AngII in a stably transfected cell model. Intracellular calcium levels, a robust marker of AT1R signaling, are recorded by SEF with the fluorescent probe Fluo8, while simultaneously capturing the whole cell response with MCWG imaging. Use of a pharmacological inhibitor made it possible to correlate specific downstream signaling pathways and heterogeneity in the AngII-dependent cell response with the information in the MCWG images.

5.6 Material and Methods

5.6.1 MCWG-SEF microscopy platform

The MCWG-SEF microscopy platform is an expansion on a custom-built MCWG imaging system based on a high-numerical-aperture objective described in detail elsewhere [Söllradl *et al.*, 2017]. The sensor chips (MCWG substrate) with the cells under study are placed in a fluid sample chamber (QR-43C, Harvard Apparatus). As shown in Figure 5.1, the light sources are collimated low-coherence fiber-coupled LEDs (λ_{nom} = 470 nm from Thorlabs or λ_{nom} = 530 nm from Mightex Systems) chosen to minimize diffraction artifacts and phototoxicity. Input light passes through a bandpass filter (530/10 or 470/20, Chroma Tech) and is focused at the back focal plane of a high-numerical-aperture microscope objective (63x, NA = 1.46, Zeiss). The offset of the focused spot from the objective's optical axis determines the incidence angle of the collimated input light at the backside of the MCWG substrate. The reflected light is collected back through the objective where a polarizing beam-splitter separates each component for visualization by a pair of CCD camera (1392x1040, 12 bit, gray-scale, Allied Vision). The transverse magnetic (TM) component contains the refractive index information for MCWG label-free imaging, while the transverse electric (TE) component is used to remove source-dependent spatial and temporal intensity variations from the images. Fluorescence light is collected simultaneously through the top window of the sample chamber using a long-working-

distance microscope objective (50x, 0.55, Mitutoyo Inc.), passes through an emission filter (HQ525/50 from Chroma Tech or LP615 from Zeiss), and is imaged by a cooled CCD camera (1392x1040, 16 bit, Qimaging). Note that while fluorescence imaging is diffraction-limited, spatial resolution in the MCWG images is anisotropic: resolution is limited along the direction normal to light propagation in the image plane by diffraction and by the finite mode attenuation length in direction of propagation. As stated above, MCWG provides a lower level of anisotropy compared to SPR at deeper probing depths [Söllradl *et al.*, 2017].

The MCWG substrates are in fact planar optical waveguides fabricated on BK7 microscope slides consisting of a thin metal layer as the bottom cladding, a dielectric core, and a liquid sensing medium with the cells as the topmost cladding [Söllradl *et al.*, 2017]. Refractive index variations at the sensor surface caused by changes in cell morphology and/or internal cell reorganizations locally change the guided mode properties, which in turn result in reflected intensity changes recorded by the TM-component CCD camera. The relatively large refractive index differences ($1.355 < n < 1.60$) between the cellular organelles and the cytosol, as well as between the organelles themselves [Y. Liu *et al.*, 2015], are easily resolvable in the MCWG images. Finally, the evanescent field in the liquid sensing medium excites fluorophores near the sensor surface, similarly to TIRF microscopy, yielding simultaneous MCWG and SEF imaging.

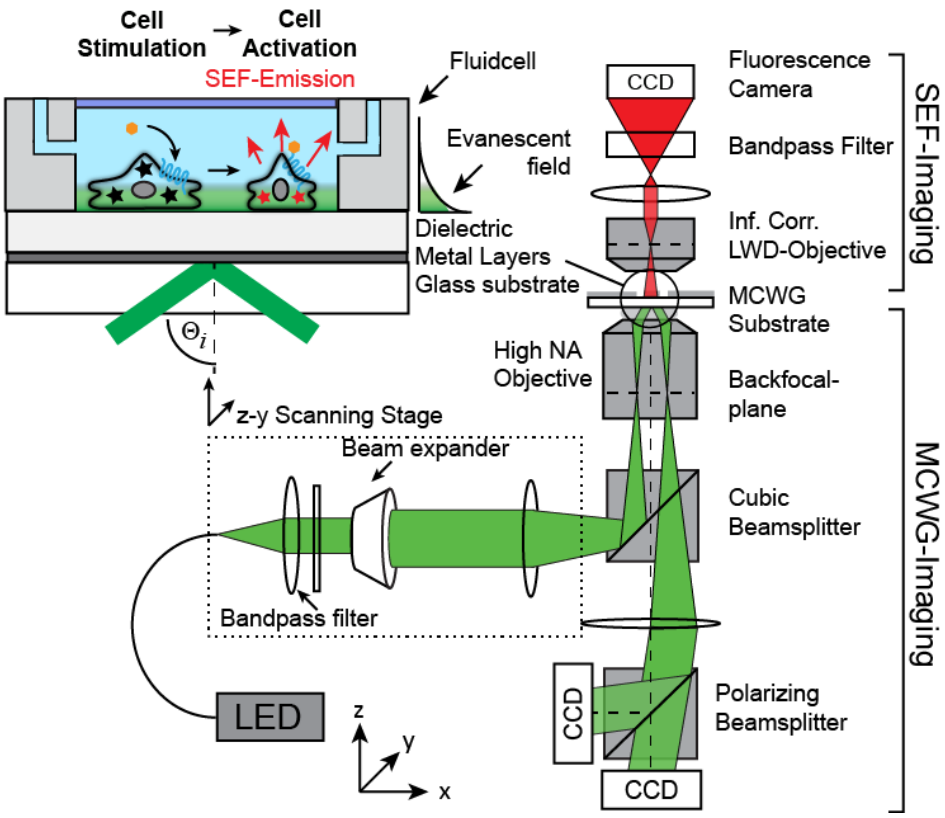

Figure 5.1: Combined MCWG and SEF imaging platform.. MCWG imaging is based on a high-numerical-aperture objective. SEF fluorescence emission is collected from the top by a long working distance objective.

5.6.2Cell culture and fluorescence staining

In a first series of experiments, an immortalized rat aortic vascular smooth muscle cell line (A7r5, ATCC, USA) was used to image the actin cytoskeleton components, where the cells were seeded on ethanol-sterilized MCWG substrates and F-actin was labeled with Alexa Fluor 532-phalloidin. Cells were maintained within selective Dulbecco's Modified Eagle's Medium (DMEM) supplemented with 10% heat-inactivated fetal bovine serum (FBS), 2.5 µg/ml amphotericin B, 50 IU/ml penicillin, 50 µg/ml streptomycin and supplemented with 1% non-essential amino acids. Post-fixation in 4% paraformaldehyde (Sigma-Aldrich) for 10 min, cells were washed twice with phosphate-buffered saline (PBS, Sigma-Aldrich) and incubated in tris-buffered saline (TBS, pH 8.1, Sigma-Aldrich) for 5 min. After additional washing with PBS, the cell membrane was permeabilized using a 0.1% triton solution (Sigma-Aldrich) for 1 min followed by a thorough wash using PBS. Actin was stained by incubating the samples with

Alexa Fluor 532-phalloidin (1:20 Thermo Fisher Scientific) for 20 min. Samples were then washed and used immediately for imaging.

In a second series of experiments, intracellular GPCR signaling activity was studied in human embryonic kidney 293 (HEK 293) cells, stably transfected to express the AT1R as described previously [Auger-Messier *et al.*, 2004]. Cells were maintained within selective DMEM supplemented with 10% heat-inactivated FBS, 0.4 mg/ml G-418, 2.5 µg/ml amphotericin B, 50 IU/ml penicillin and 50 µg/ml streptomycin. To observe intracellular calcium levels, HEK-AT1R cells were seeded at a density of 5.75 x 10^5 on poly-L-lysine-coated sensor chips and grown to 60% confluence. Cells were washed twice with warm Hank's balanced salt solution (HBSS) and incubated with the calcium indicator Fluo-8 (5 µM, Thermo Fisher Scientific) for 1 h at room temperature, washed twice and left for another 30 min in HBSS for de-esterification prior to an experiment. AT1R-activation was performed by exchanging the media in the sample chamber using a syringe pump (100 µl/min for 8 min) with HBSS buffer containing 100 nM Angiotensin II (American Peptide). ROCK kinase activity was inhibited by pre-incubating the cells with Y27632 for 30 min (10 µM, Sigma-Aldrich) and the inhibitor was present throughout the experiment.

5.7 Results and Discussion

5.7.1 Actin cytoskeleton imaging by MCWG-SEF microscopy

VSMCs exhibit a densely structured network of actin filaments [Gary K Owens *et al.*, 2004] and are the mechanically active cell layer responsible for regulating vascular muscle tone and blood pressure. Figure 5.2A shows a series of MCWG micrographs of a single VSMC adhered to the sensor surface taken at increasing angles of incidence (Θ_i) to resonantly couple to a range of refractive indices in the sensing medium. At 64.17° (Figure 5.2A), resonant coupling to the fluid medium is achieved (darkest background indicating lowest reflectivity) and evanescent field intensity is maximized, where the dominant features in the MCWG micrograph are filamentous structures aligned with the long cellular axis. The greater probing depth provided by MCWG enables the visualization of structures in these cells that are consistent with actin filaments [Kanchanawong *et al.*, 2010]. To confirm that these structures are indeed actin fibers,

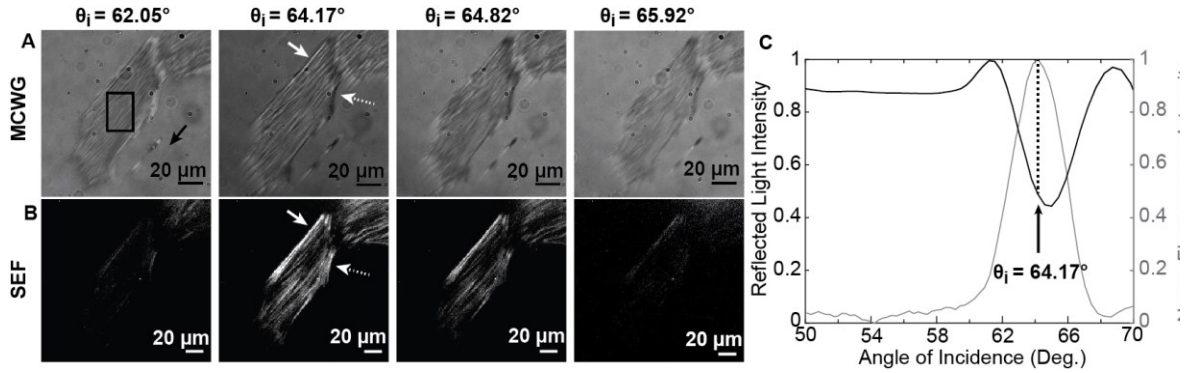

Figure 5.2: Vascular smooth muscle cell simultaneously imaged by MCWG and SEF.. A) MCWG micrographs of a single VSMC taken at different angles of incidence. The black square in the leftmost image represents the location of ROI used to calculate average reflected intensity, while the black arrow indicates the direction of mode propagation; B) SEF micrographs simultaneously taken at the same angles of incidence, F-actin was labeled with Alexa Fluor 532 Phalloidin; C) Plots of normalized average reflected light intensity within the ROIs in A and overall average SEF intensity in B as a function of incidence angle

the high-affinity F-actin probe phalloidin-Alexa Fluor 532 was used to label the cell cytoskeleton and SEF micrographs were simultaneously recorded (Figure 5.2B). As expected, the highest SEF signal intensity is achieved at 64.17°, an angle at which a good correlation between the elongated structures in the MCWG and SEF micrographs is observed. As explained above, spatial resolution in the imaging plane is anisotropic for label-free imaging modality. In our MCWG-SEF microscope, spatial resolution in the MCWG images is limited by diffraction limit of ~0.18 μm in the direction normal to mode propagation and to ~5.0 μm in the direction of mode propagation (black arrow in leftmost image in Figure 5.2A) due to the finite attenuation length of the mode [Söllradl *et al.*, 2017]. This effect can also be seen in the second image from the left in Figure 5.2A (64.17°) where the fibers aligned in the direction of propagation are clearly resolved (white arrow) while structures that are slightly off-axis appear partly blurred (white dotted arrow). Note since the fluorescent labels acts as point sources of light, the SEF signal is not subject to this effect (spatial resolution in the SEF images is isotropic and diffraction-limited in both axes). In addition, as observed by others with SPR [Nakkach *et al.*, 2008], the presence of fluorophores with an absorption band that overlaps the excitation light spectrum locally modulates the (complex) refractive index in the sensing medium, acting as a contrast enhancement agent in the MCWG images.

Figure 5.2C shows plots of normalized average reflected light intensity within the ROI in (Figure 5.2A, black square at 62.05°) and simultaneous overall average SEF intensity, as a function of incidence angle. A minimum in reflected light intensity occurs at critical coupling to the guided surface mode corresponding to the fluid medium as the upper cladding (black trace, $\theta_i = 64.82°$). At this angle, the electric field intensity at the sensor surface is maximized, yielding high fluorescence intensity (grey trace), as previously observed by our group and others for SPR [Liebermann & Knoll, 2000; Söllradl *et al.*, 2017]. Interestingly, maximum fluorescence intensity ($\theta_i = 64.17°$) is slightly shifted from the minimum in reflected light intensity due to metal-induced damping losses [Liebermann & Knoll, 2000].

5.7.2 AT1-induced cell activity analyzed by MCWG-SEF microscopy

Cell-based, label-free technologies are now routinely used to monitor cellular responses associated with the activation of signaling pathways in cell populations to provide insight into their complex mechanisms and functions [Schröder *et al.*, 2010; Scott & Peters, 2010]. While GPCR signaling is often assumed to be homogeneous within a cell population, receptor expression levels and variations in individual cell phenotypes can alter their overall response profile and lead to heterogeneous population responses [Nickenig *et al.*, 1997; Wechsler *et al.*, 2006]. To demonstrate the possibility of assessing such population-dependent behavior, we used a HEK293 cell model stably transfected with AT1R [Kaufman *et al.*, 2008]. In this cell model, two major signaling cascades are involved following receptor activation by AngII, namely the G_q-protein dependent signaling cascade leading to intracellular calcium mobilization and the $G_{12/13}$/Rho/ROCK pathways. These pathways are known to be involved in both the regulation of the cytoskeleton organization and actin-myosin-dependent contractile activity [Emmert *et al.*, 2003; Park *et al.*, 2002].

We used the MCWG-SEF microscopy system to follow intracellular calcium levels with the fluorescent probe Fluo8 (SEF imaging) while simultaneously monitoring the overall cellular morphological response (MCWG imaging) resulting from AT1 receptor activation by AngII. Figure 5.3 shows a time series sample of eight individual cells imaged with MCWG (left image column) and SEF (right image column). MCWG micrographs B-E are color-coded maps of percentage reflectance difference relative to the reference (Figure 5.3A), where the blue end of

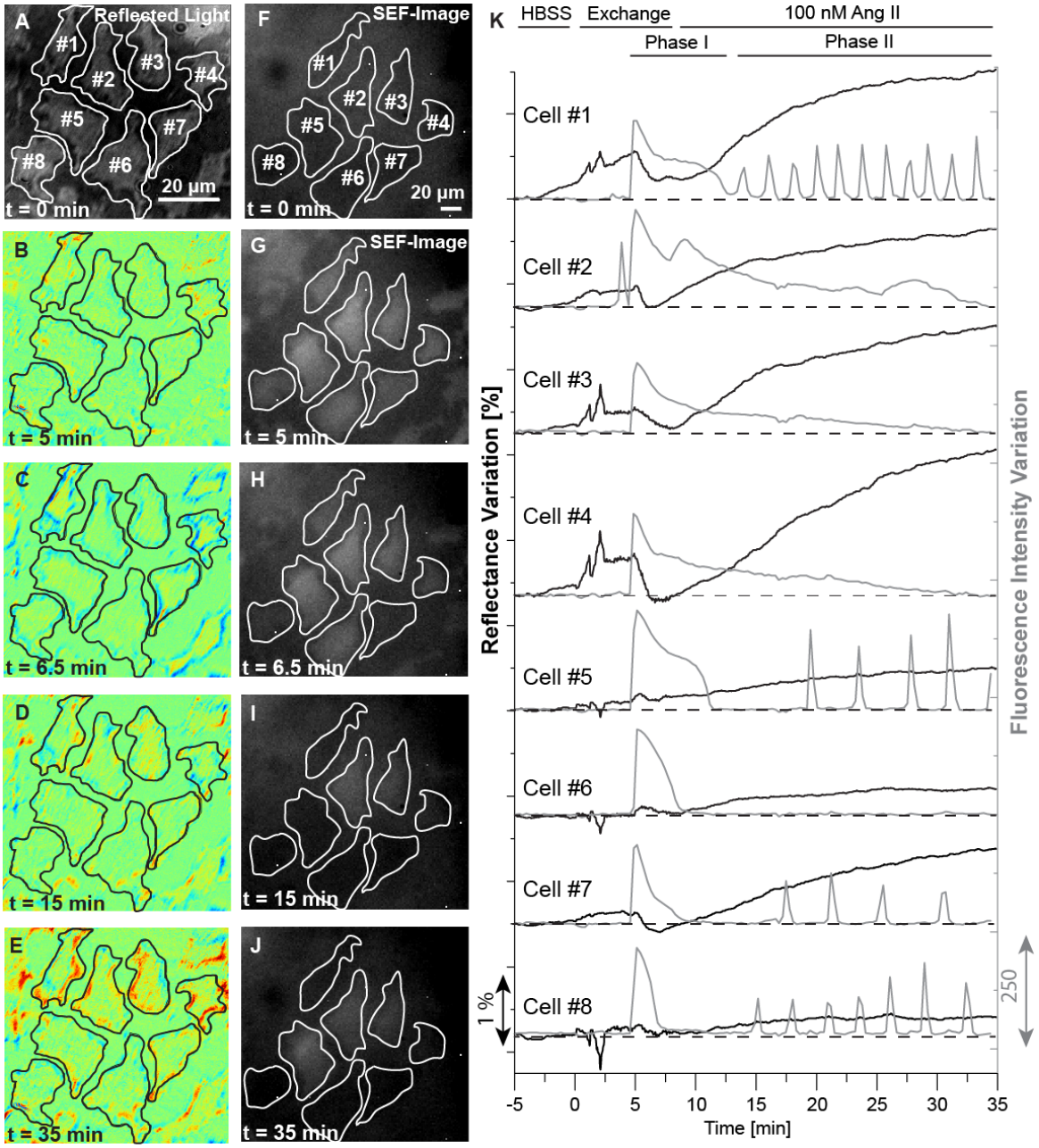

Figure 5.3: Simultaneous monitoring of intracellular calcium by SEF imaging and cellular morphological response by MCWG imaging. A) Reflectance micrograph of 8 individual HEK-AT1 cells; B-E) Reflectance variation micrographs showing local changes in reflectance following stimulation with 100 nM AngII at t = 0 min (blue end of the spectrum indicates a decrease, red end of the spectrum indicates an increase, green indicates no change); F-J) Simultaneous SEF micrographs, where cells were loaded with calcium indicator Fluo-8; K) Plots of the full-time sequence of average MCWG reflected intensity and SEF average intensity, normalized by cell surface area.

the spectrum indicates a decrease, the red end of the spectrum indicates an increase, and green indicates no change. Following AngII stimulation at 0 min, a burst of intracellular calcium is

observed at 5 min in the SEF images and quantified in the average fluorescence intensity plots, confirming receptor activation and functionality of the signaling pathway in this cell model. The burst of intracellular calcium is followed by the appearance of localized decreases in MCWG reflectance (blue regions) attributable to a reduction in cellular mass density within the effective sensing range of the evanescent field, consistent with increased acto-myosin contractile activity in this cell model [Auger-Messier *et al.*, 2004; Cuerrier *et al.*, 2008], where the minimum MCWG average signal intensity occurs at ~6.5 min. The appearance of blue regions detected by MCWG microscopy could previously be attributed by our group to a localized reorganization of cellular components at the sensor surface [Söllradl *et al.*, 2018], as expected from an increased contractile activity. The initial burst in intracellular calcium level is then followed by a recovery phase were calcium levels return to near basal levels after 15 min to 35 min for most cells (Figure 5.3I and J), as generally observed for receptor coupled to the calcium pathway. In contrast, the MCWG micrographs (Figure 5.3D and E) show a distinctly heterogeneous behavior within the cells with both localized increases and decreases in signal levels, indicating a re-modeling of intracellular structures associated with cell activation [Söllradl *et al.*, 2018] and possibly as a result of AT1 receptor-signaling activity [Cuerrier *et al.*, 2008, 2009].

The plots in Figure 5.3K show the time sequences of averaged MCWG reflected intensity and SEF average intensity, with both signals normalized by cell surface area as presented in Figure 3A and F. The plots show a biphasic response in both the SEF and the MCWG time profiles. Phase I is associated with the initial burst of intracellular calcium following stimulation of the cells with AngII (5 min), confirming the receptor activation and subsequent G_q signaling known to mobilize calcium from the endoplasmic reticulum [Auger-Messier *et al.*, 2004]. Phase II of the reflectance signal is associated in time to the recovery of the intracellular calcium levels for all cells. Intriguingly, these oscillations in calcium levels were not found to be associated to the MCWG signal, indicating that they do not induce significant morphological changes or cell boby contraction in this cell model. It should be noted here that oscillating calcium signals are a well-known phenomenon and provide a digital signal to downstream effectors, involved in the regulation of gene expression, a process that normally occurs over several hours [Dolmetsch *et al.*, 1998].

As expected, the SEF and MCWG data are strongly correlated, confirming the receptor-dependent cell signaling response origin of the MCWG label-free signal. However, significant differences can also be observed when comparing individual responses. During phase I, though all cells showed an intracellular calcium burst (indication of AT1R functionality), only cells #1-4 and 7 showed a subsequent marked decrease in average MCWG reflectance. During phase II, cells #1, #5, #7 and #8 exhibited oscillations in their intracellular calcium levels with varying periodicity (116 sec, 230 sec, 265 sec and 173 sec, respectively), while cells #2, #3 and #4 showed sustained elevated calcium levels. The absence of such distinct features within the MCWG signal further demonstrates that changes in the intracellular calcium levels do not interfere with the observed MCWG signal, which has also been demonstrated for other label-free detection modalities [Cuerrier *et al.*, 2008]. These observations indicate that the G_q-dependent calcium signal alone might be insufficient to explain the first phase of the MCWG signal, indicating that other pathways may be required for the phase I of the MCWG signal.

5.7.3 Role of ROCK and $G_{12/13}$ during AT1 signaling and its link to cellular activity

In addition to the calcium-dependent G_q signaling cascade, AT1R is also coupled to a calcium-independent $G_{12/13}$ signaling pathway [Emmert *et al.*, 2003]. The activation of this pathway ultimately leads to activation of ROCK, which is a ubiquitous intracellular kinase [Park *et al.*, 2002] involved in actin remodeling and the regulation of actomyosin contractile activity via myosin light chain (MLC) phosphorylation and inhibition of the myosin light chain phosphatase (MLCP). To test the involvement of $G_{12/13}$ signaling and thus the involvement of ROCK in the measured cellular response, HEK293-AT1R cells were treated with the ROCK inhibitor Y-27632 prior to activation with AngII.

Figure 5.4A-J show MCWG (A: reference, B-E: differences) and SEF micrographs from the experiment, alongside plots of cell-specific average MCWG and SEF responses for the time series normalized by cell area (Figure 5.4K). As expected, the MCWG data do not show a signal decrease (phase I) following AT1 activation, confirming the robust suppression of cell signaling activity through ROCK inhibition (Figure 5.4C). The phase II in the MCWG signal response nevertheless appears not to be impacted as indicated by the appearance of large yellow and red

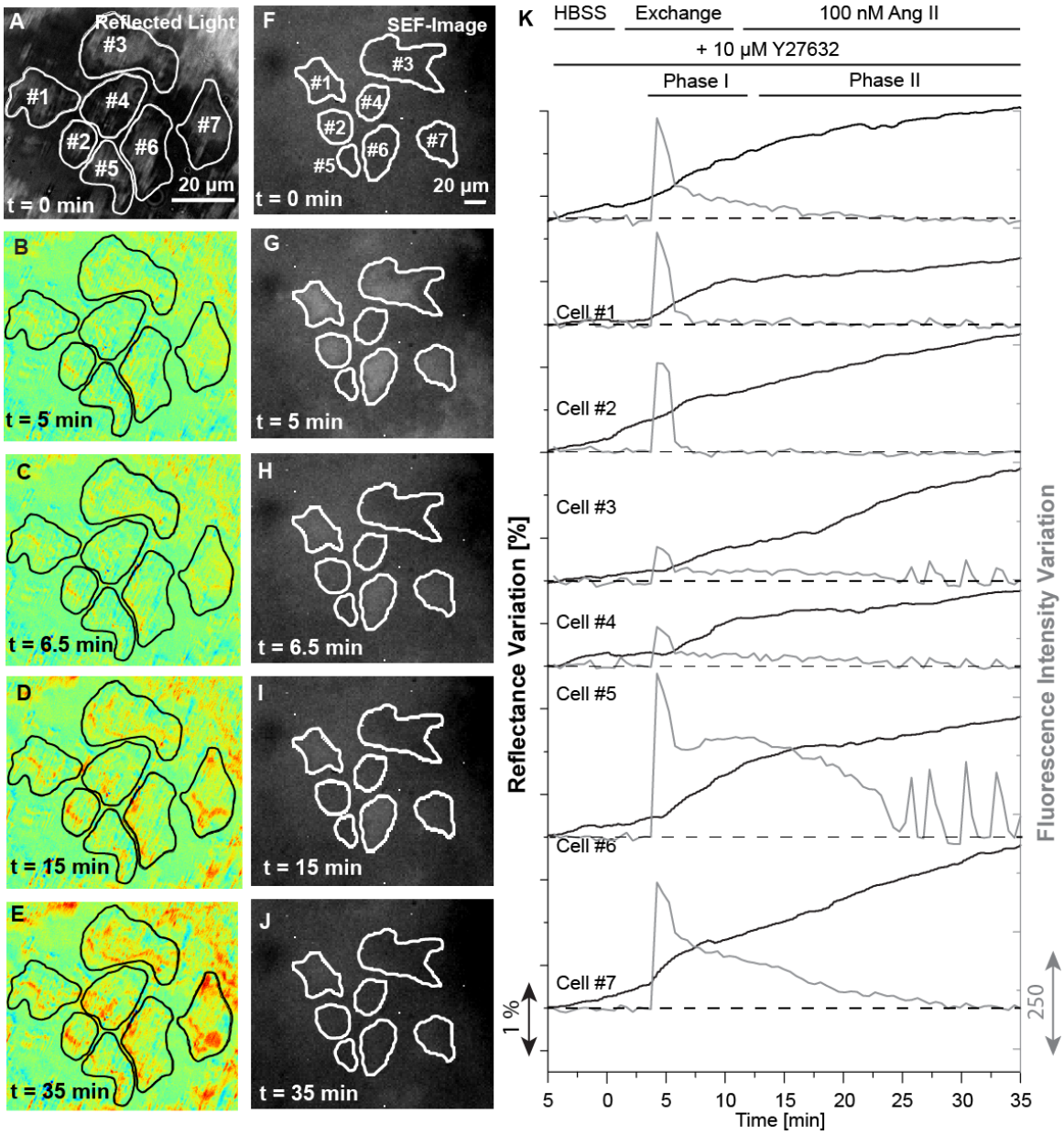

Figure 5.4: Impact on ROCK inhibition during AT1 analyzed by MCWG and SEF microscopy.. A) Reflectance micrograph of individual HEK-AT1R cells; B-E) Reflectance variation micrographs showing local changes in reflectance after pretreatment with Y-27632 and stimulation with 100 nM AngII; F-J) SEF micrographs of the same cells, loaded with calcium indicator Fluo-8; K) Plots of cell-specific average MCWG and SEF responses for the full time series normalized by cell area.

areas in the MCWG micrographs (Figure 5.4D and E). The SEF data again shows a robust release of intracellular calcium, as expected from AT1 activation (Figure 5.4G-J). When comparing the experimental time series (Figure 4K), interestingly despite the absence of a Phase I response in the MCWG data, all cells nevertheless show a steady increase in average

MCWG response during Phase II suggesting a distinct $G_{12/13}$-independent signaling mechanism for Phase II compared to the previous experiment due to additional unidentified component. The SEF time series shows again a biphasic response profile where all cells respond with a transient release of intracellular calcium shortly after AngII stimulation as expected from AT1 activation. Overall, these results indicate that $G_{12/13}$ signaling may be the major signaling pathway responsible for Phase I and is consistent with previous population-based findings using SPR spectroscopy in which ROCK inhibition, but not MLCK inhibition, associated with G_q signaling could successfully suppress Phase I contractile response [Cuerrier *et al.*, 2008].

5.8 Conclusion

In this work, we demonstrated a combined MCWG and SEF microscopy system for dual mode imaging and signal analysis of receptor-dependent cell signaling activity. We demonstrated the capabilities of this system in experiments designed to 1) identify the specific structural components of the cytoskeleton imaged by MCWG and SEF, and 2) provide insight into intracellular signaling following GPCR activation in living cells. In the latter case, SEF imaging revealed the intracellular G_q-dependent calcium mobilization while simultaneous MCWG imaging showed the distinct individual cell response profiles to AngII-mediated AT1R activation. A strong temporal correlation was observed between the MCWG label-free signal and the labelled calcium signal from individual cells, confirming the origin of the MCWG label-free signal as a receptor-dependent cell signaling response. Interestingly, a discrepancy between the two signals observed for some cells suggests that cell signaling activity is not necessarily dependent on calcium mobilization. This type of observation is only possible through a comparative analysis of individual cell heterogeneity present in the two distinct response profiles. Using a selective $G_{12/13}$/Rho/ROCK signaling inhibitor, we determined that this pathway is required for the phase I response observed with MCWG imaging. Interestingly, the second phase of the response profile was not impacted by $G_{12/13}$/Rho/ROCK signaling inhibition, suggesting that a G_q-dependent pathway may be required for this later phase. While other signaling cascades could also be involved in AT1 signaling, this work shows how individual cell assessment using MCWG and SEF together with pharmacological tools and fluorescent probes targeting specific cell signaling pathways can enables the identification of

key contributors to a given cellular response. Thus, this system should find applications in drug screening, signaling cascade profiling, and in the study of fundamental cellular mechanisms.

5.9 Acknowledgements

This work was supported by the Fonds de recherche du Québec – Nature et technologies (FRQNT: MG, PGC, TS), the Natural sciences and engineering research council of Canada (NSERC: MG, PGC, MC), and the Canadian Institutes of Health Research (CIHR) under the Collaborative Health Research Program (MG, PGC). LN2 is an international research laboratory co-managed in Canada by University of Sherbrooke and in France by CNRS, Université de Lyon (Centrale Lyon, INSA Lyon et CPE Lyon), and Université Grenoble-Alpes; LN2 is funded in Québec by the FRQNT. TS was also supported by the COMET K1 center Austrian Smart Systems Integration Research (ASSIC). The COMET Competence Centers for Excellent Technologies Program is supported by BMVIT, BMWFW and the federal provinces of Carinthia and Styria of Austria.

CHAPTER 6 Discussion

This thesis describes a combined imaging platform using two distinct imaging modalities: label-free MCWG and label-based SEF. In CHAPTER 3, a detailed description of the label-free microscopy system and optimization of the MCWG sensor chips is given. CHAPTER 4 applies MCWG microscopy to detect heterogeneity within a cell population undergoing apoptosis and demonstrates how extracellular features can help explain the underlying sensor response profile. These two chapters demonstrate the benefits of having a high-resolution, deep probe system for live cell imaging and how MCWG-based sensor chips are capable of overcoming certain issues associated with SPR microscopy in the context of cell-based biosensing.

CHAPTER 5 describes an integral sensing approach combining MCWG and SEF microscopy to quantify cell-signaling activity and investigate the underlying structural components contributing to the observed label-free sensor signal. This allows the observer to delineate the intracellular signaling pathways by SEF and link it to the observed functional response of the cells in MCWG microscopy. As both techniques have sufficient resolution to detect single cell activity, this approach was able to reveal heterogeneity within the cell population under study. Furthermore, by using specific pharmacological inhibitors, we altered the cellular response profile to enable us to draw conclusions about signaling molecules involved in the observed cellular activity and function.

This chapter is separated into two parts. The first part discusses different aspects of MCWG-based microscopy for cellular biosensing. The intrinsic tradeoff in lateral resolution and penetration depth for evanescent field-based methods is discussed. Furthermore, the application of MCWGs to SEF is discussed, and certain advantages and potential applications using both, TM and TE modes are discussed. The second part focuses on the biological aspect and how MCWG sensor chips can be tailored to extract additional structural information from cells. At the end of the chapter, some system modifications are discussed to increase the throughput.

6.1 MCWG and SEF Microscopy

While SPR-based spectroscopy has been extensively used for the quantification of intracellular signaling activity [Chabot *et al.*, 2009; Hide *et al.*, 2002; Maltais *et al.*, 2012], MCWG-based spectroscopy has been less frequently applied in the field [N. Skivesen *et al.*, 2007]. Similarly, when applied to the study of cells, SPRI has mainly been applied to study cell-substrate interactions and subcellular features near the sensor surface, such as focal adhesion sites [Peterson *et al.*, 2009]. In contrast, to the best of my knowledge, MCWG sensor chips have yet to be used for live-cell imaging by other groups.

In evanescence-based label-free microscopy, the sensor chip setup must be adapted to the application at hand. As shown in CHAPTER 3 Section 3.6, there is an intrinsic tradeoff between the penetration depth and the maximum achievable resolution with SPR- and MCWG-based sensors. SPRI-based imaging, for example, due to the strong confinement of the evanescent field and the resulting high losses within the thin metal layer, can clearly achieve the highest possible lateral resolution. The tradeoff, however, is very shallow probe depth and only structures within the first few hundred nanometers being observable with SPRI. Thus, SPRI is well suited for the investigation of cell-substrate interactions and has been extensively applied to visualize cell surface attachments, focal adhesion sites, and adlayer deposition surrounding the cell [Peterson *et al.*, 2009].

If, for example, changes in cellular activity due to receptor-mediated signaling [Schröder *et al.*, 2010; Scott & Peters, 2010], changes in cell activity induced by toxins and antigens [Chabot *et al.*, 2009; Hide *et al.*, 2002] or apoptosis [Arndt *et al.*, 2004; Maltais *et al.*, 2012] are of interest, the cell response is not necessarily confined to the basal portion of the cell. Greater probe depth is achieved with either a symmetric chip structure in a technique referred to as long range SPR (LR-SPR), or with MCWG-based devices. While the advantages of such deep-probe devices have already been demonstrated for live cell studies [Chabot *et al.*, 2012; N. Skivesen *et al.*, 2007], to-date, they have only been used in population averaged studies. Based on the results presented in this work, MCWG performs best at short wavelength in the visible range (CHAPTER 3 Section 3.6) as a deep-probe sensor chip while maintaining the high lateral resolution necessary for single cell resolution.

The evanescent field of the propagating mode in an MCWG-based system can be used to excite fluorophores in a similar way to TIRF- and SPEF-based systems. Compared to TIRF, a strong field enhancement is achievable in SPEF and MCWG (CHAPTER 3, Section 3.6) due to the resonant coupling of light. However, the thin metal film needed for SPEF also introduces two additional distance-dependent non-radiative decay mechanisms effectively quenching fluorescence emission within tens of nanometers of the metal surface [Dostálek & Knoll, 2008; Liebermann & Knoll, 2000]. Thus, a dielectric spacer layer is often placed between the metal surface and the fluorophore to overcome these issues [Bauch *et al.*, 2013]. MCWG also shows a significant field enhancement. However, MCWG intrinsically involves a dielectric core above the metal cladding, which prevents Förster energy transfer and thus protects against quenching. Furthermore, due to the Stokes' shift of the emitted fluorescent light, the required dielectric core thickness for a MCWG mode to exists must be larger. When designed to operate at the cut-off thickness of the mode for the excitation wavelength back coupling of the fluorescent light can be prevented.

Unlike SPR, MCWG supports both TM and TE modes (CHAPTER 2, Section 2.3.2), which are beneficial for the characterization of anisotropic optical parameters of lipid bilayers [Salamon *et al.*, 1997]. When applied to SEF, the orientation of a dipolar fluorophore relative to the electric field can improve fluorescence efficiency [Axelrod, 2001]. In living cells, membrane reorientation occurs during cellular activities such as endocytosis or cell surface ruffling. Due to the limited spatial resolution in MCWG microscopy, the sole label-free visualization of such membrane regions can be challenging. A combined approach relying on SEF and sensor chip supporting both modes in TM and TE enables the selective excitation of different fluorophores and imaging of the respective regions in SEF, similar to a polarized TIRF approach [Sund *et al.*, 1999].

6.2 Individual Cell-Based Biosensing

A high spatial-resolution imaging system is required to reliably extract sensor signals from individual cells following activation by different stimuli such as pro-apoptotic drugs or hormones. In addition, such an imaging system could further help to discriminate the underlying

structural features associated with the sensor signal. In this thesis, such a system was developed and advantages of a combined label-free and label-based approach was demonstrated.

6.2.1 Multimodal Sensing for Selective Structural Imaging

Cells utilize different intra- and extracellular structures to adhere to and migrate along their microenvironment. Such structures occur at different heights ranging from being in direct contact with the extracellular matrix (integrins < 20 nm) via the cell membrane and an interim signaling layer (20-40 nm) to the force transduction layer (vinculin 40-60 nm) and the actin cytoskeleton (> 100 nm) [Kanchanawong *et al.*, 2010]. MCWG offers the ability to specifically tailor the imaging penetration depth by tuning the dielectric core thickness and/or the excitation wavelength. Such an approach allows the tailoring of a sensor chip to probe different depths, thereby probing specific intracellular region in a similar fashion to TIRF microscopy [Olveczky *et al.*, 1997].

6.2.2 Extracting Heterogeneity Within a Larger Cell Population

For the detection of phenotypic heterogeneity within a cell population, cell-based biosensing techniques need a sufficiently high spatial resolution to extract signals from a single cell level. If, for example, a pro-apoptotic drug is tested on cancer cells, the results obtained from a population-based study might not reflect individual cell-to-cell sensitivity or provide information about subpopulations refractory to the treatment [Gascoigne & Taylor, 2008; Slack *et al.*, 2008]. To detect such subpopulations, however, a large number of cells need to be studied to draw statistically reliable conclusions. The high-resolution system developed during this thesis currently offers a relatively small FOV for such investigations. The system could be equipped with an automated y-z stage mapping multiple ROIs to enlarge the number of cells studied during a single experiment and expand the throughput capabilities.

CHAPTER 7 Conclusion (French)

Les techniques de détection sans marquage telles que la résonance des plasmons de surface, les réseau de diffraction et la spectroscopie d'impédance sont maintenant communément utilisées afin de suivre l'activité cellulaire lorsqu'exposé à des hormones, agents pharmacologiques ou toxine. Le signal mesuré est souvent issu de nombreuses cellules, supposant ainsi que le profil de réponse cellulaire sous-jacent est homogène au sein d'une population. Il y a cependant un nombre croissant de démonstrations qui illustrent qu'il existe un haut niveau d'hétérogénéité entres les cellules d'une même population.

Bien qu'ils soient très sensibles, ces systèmes n'ont souvent pas une résolution spatiale suffisante pour détecter une activité de signalisation cellulaire individuelle, empêchant ainsi la détection de l'hétérogénéité cellulaire. De plus, puisque les réponses cellulaires impliquent l'intégration d'événements de signalisation intracellulaires complexes, il peut être difficile de d'extraire la contribution individuelle des différents composantes dans le signal mesuré.

Dans ce projet de recherche, une plate-forme d'imagerie combinée a été développée avec comme objectif l'observation et la quantification simultanées d'activité de signalisation cellulaire individuelle par une technique de microscopie avec et sans marquage.

Les résultats numériques ont montré que les capteurs basés sur les MCWG offrent le compromis optimal entre la résolution latérale et la profondeur d'observation dans l'échantillon. Dans cette thèse, les avantages et les capacités du système développé sont démontrés par la détection de la variabilité comportementale d'une cellule à l'autre au sein d'une population subissant une apoptose. Lorsque appliqué à une monocouche cellulaire, le système a permis d'observer de façon fiable les variations de taille de l'espace intercellulaire, des distributions d'interstices des espaces extraites et l'hétérogénéité au sein d'une monocouche altérée après stimulation par la thrombine.

Le travail présenté dans cette thèse a également démontré comment les signaux de microscopie SEF et MCWG se complètent et aident à déconvoluer le profil de réponse fonctionnelle des cellules vivantes. En utilisant des marqueurs spécifiques, le signal de fluorescence peut être

utilisé afin d'observer des composantes structurelles spécifiques visibles dans les micrographies MCWG. Il devient donc possible de clarifier la contribution de différentes composantes intracellulaires dans le signal observé. De plus, le signal SEF peut être utilisé pour détecter une activité de signalisation intracellulaire résultant de l'activation d'un récepteur. Les résultats présentés dans ce travail démontrent les avantages d'une étude cellulaire intégrée et montrent comment les agents pharmacologiques peuvent être utilisés afin de d'isoler les voies de signalisation intracellulaires complexes impliquées dans une réponse cellulaire.

CHAPTER 8 Conclusion

The main objective of this research project was to *develop a high resolution, deep probing evanescent field-based imaging platform for simultaneous label-free and label-based characterization of individual cells*. Each chapter describes the different steps to achieve this goal. The first part of this work focused on the optimization and characterization of the underlying label-free sensing technique (MCWG), comparing it to other techniques commonly used for cell-based biosensing such as SPR and LR-SPR. Based on these results, an informed choice about the optimal sensor chip setup was made. As MCWG microscopy has, to the best of my knowledge, never been applied to live cell sensing, the second part showcases the novelty and the expected performance of the approach. The third part demonstrates the combination of SEF and MCWG microscopy and how this approach provides insight into intracellular signaling activities.

8.1 Summary and Overview of Achieved Goals

The following objectives have been realized in this work:

1) Development of a high-magnification surface-based imaging platform capable of discriminating individual cellular activity in both label-free and labeled-based imaging modalities.

As presented in CHAPTER 3, a label-free MCWG-based microscope was realized using a high-NA microscope objective. The performance of this system was characterized using synthetic and biological samples. In CHAPTER 5, the system's capabilities are expanded for simultaneous acquisition of fluorescence and MCWG micrographs. SEF micrographs were acquired using an long working-distance objective at the top of the sensor chip while the MCWG sensor chip was used to excite the fluorophores.

2) Optimization, fabrication, and characterization of deep-probe evanescent field-based sensor chips. Such sensor chips must be operated at visible wavelengths for fluorescence

excitation while maintaining a deep sensing depth and a high spatial resolution to discern individual cells.

Simulation results are presented in CHAPTER 3 where MCWG-based sensitivity is compared to other evanescent wave-based sensing techniques such as SPR and LR-SPR. While SPR can achieve the highest spatial resolution and LR-SPR is capable of reaching deeper penetration depths MCWG was found to offer the best compromise between spatial resolution and probe depth. Our results show that this system can probe deeply (620 nm) therefore penetrating a significantly larger portion of the cell compared to SPR, while maintaining sufficient spatial resolution (5 μm) to visualize and quantify individual cell activity.

3) Application to a cell population to quantify cell-cell heterogeneity and characterize the impact of cellular features on the signal.

As presented in CHAPTER 4, MCWG microscopy was used for spatially resolved monitoring of cell signaling activity in a small population of cells. The system's capabilities were demonstrated by two sets of experiments. The first experiments highlight the system's capabilities to monitor a heterogeneous cell population response by following the intracellular mass redistribution associated with exposure of the cells to the pro-apoptotic drug TRAIL. Depending on the stimulus, apoptosis is often a highly heterogeneous process and quantification of such heterogeneity within certain subpopulations of cells can be challenging. Our results show that MCWG microscopy allows for such analysis and reliable quantification of important kinetic parameters within the population. In the second set of experiments, the integrity of an endothelial monolayer was monitored following thrombin stimulation. The high spatial resolution of the system allowed the sensor signal to be correlated with variations in intercellular gap size and the extraction of gap size distribution and heterogeneity within the disrupted monolayer. Thrombin stimulation was associated with a marked increase in gap size and the obtained signals were comparable to established permeability assays such as TEER.

4) Demonstrate the benefits of a combined label-free and label-based sensing approach for simultaneous visualization and quantification of cellular activity to delineate the specific

underlying signaling events and cellular structure responsible for the MCWG signal at a single cell level.

As presented in CHAPTER 5, the advantages of the approach were demonstrated through a set of two experiments. In the first experiment, the system was used to visualize components of the actin cytoskeleton in vascular smooth muscle cells. In this experiment, the system enabled the cell structural features visible by MCWG microscopy to be identified. In the second set of experiments, the SEF signal was used to reliably quantify intracellular G_q-dependent calcium mobilization following AngII-mediated AT1R activation. A strong temporal correlation was observed between the label-free MCWG signal and the calcium signal, thereby directly relating the label-free signal to AT1R activity. The initial phase of the MCWG signal was successfully suppressed by the use of specific pharmacological inhibitors, while the intracellular calcium signal remained detectable by SEF. These experiments show the advantages of using a combined MCWG and SEF imaging system for individual cell assessment and how a combination of pharmacological tools and fluorescent probes can be used identify key signaling pathway contributors to the functional cellular response.

8.2 Contribution of this Work

Label-free sensing techniques such as surface plasmon resonance, diffraction gratings, and electrical impedance spectroscopy are now routinely used for monitoring cell-signaling activity when exposed to hormones, pharmacological agents, and toxins. The signal of these assays is often derived from many cells, thereby assuming that the underlying cell response profile is homogeneous within the population. There is, however, an increasing body of evidence demonstrating a high level of cell-to-cell heterogeneity within a population. While highly sensitive, these systems often lack sufficient spatial resolution to detect individual cell signaling activity thus hindering the detection of cell heterogeneity. Furthermore, since cellular responses involve the integration of complex intracellular signaling events, delineating the contribution of the different components can be challenging.

In this research project, a combined imaging platform was developed for the simultaneous visualization and quantification of individual cell signaling activity by a label-free and label-

based microscopy technique. Numerical results showed that MCWG-based sensor offer the optimal tradeoff between lateral-resolution and probing depth. In this thesis the advantages and capabilities of the developed system are presented by the detection of cell-to-cell variability within a population undergoing apoptosis. When applied to a cell monolayer, the system reliably followed variations in intercellular gap size, extracted gap size distributions and heterogeneity within the disrupted monolayer following thrombin stimulation.

This work further demonstrated how the signals from both SEF and MCWG microscopy complement each other and help to deconvolve the functional response profile of living cells. Using specific markers, the fluorescence signal can be used to visualize specific structural components visible in the MCWG micrographs and clarify the contribution of different intracellular components to the observed signal. In addition, the SEF signal can be used to detect intracellular signaling activity resulting from receptor activation. The results presented in this work demonstrate the advantages of integrated cell assessment and show how pharmacological agents can be used to delineate the complex intracellular signaling pathways involved in a cellular response.

8.3 Outlook

The system was developed in close collaboration with the Institut de Pharmacologie at the Université de Sherbrooke. As such, it is well adapted for live cell imaging and the requirements of the pharmacology and cell biology fields. The scope of this work was to develop the combined imaging platform and demonstrate its capabilities in selected cell models. Following this initial characterization step, the system can now be widely applied.

In the context of apoptosis, for example, it would be possible to utilize fluorescent dyes reporting the specific activation of different components of the apoptosis pathway. Such an approach could be used to detect the origin of heterogeneous signaling activity within a cell population undergoing apoptosis, identify subpopulations within a cancer cell line refractory to treatment and develop specific drugs to treat these phenotypes.

In another application, the system could help overcome certain issues associated with slow-growing cell lines such as neurons or primary cells. These cells are difficult to culture in sufficient numbers for conventional non-imaging-based label-free sensing. The imaging platform herein is capable of overcoming this issue by selecting only ROIs where a cell is present, thus suppressing the background signal and extracting a single-cell signal. Furthermore, the use of fluorescent dyes could help determine the current phenotypical state of the cell under study, thereby maximizing the information extracted. As such, this system will provide researchers with a new and more powerful tool for live cell biosensing.

Bibliography

Abbas, A., Linman, M. J., & Cheng, Q. (2011). Sensitivity Comparison of Surface Plasmon Resonance and Plasmon-Waveguide Resonance Biosensors. *Sensors and Actuators. B, Chemical*, *156*(1), 169–175. https://doi.org/10.1016/j.snb.2011.04.008

Abelès, F. (1950). La théorie générale des couches minces. *Journal de Physique et Le Radium*, *11*(7), 307–309. https://doi.org/10.1051/jphysrad:01950001107030700

Aizawa, H., Sameshima, M., & Yahara, I. (1997). A Green Fluorescent Protein-actin Fusion Protein Dominantly Inhibits Cytokinesis, Cell Spreading, and Locomotion in Dictyostelium. *Cell Structure and Function*, *22*(3), 335–345. https://doi.org/10.1247/csf.22.335

Albeck, J. G., Burke, J. M., Aldridge, B. B., Zhang, M., Lauffenburger, D. A., & Sorger, P. K. (2008). Quantitative analysis of pathways controlling extrinsic apoptosis in single cells. *Molecular Cell*, *30*(1), 11–25. https://doi.org/10.1016/j.molcel.2008.02.012

Altschuler, S. J., & Wu, L. F. (2010). Cellular Heterogeneity: Do Differences Make a Difference? *Cell*, *141*(4), 559–563. https://doi.org/10.1016/j.cell.2010.04.033

Anderson, J. C., Clarke, E. J., Arkin, A. P., & Voigt, C. A. (2006). Environmentally Controlled Invasion of Cancer Cells by Engineered Bacteria. *Journal of Molecular Biology*, *355*(4), 619–627. https://doi.org/https://doi.org/10.1016/j.jmb.2005.10.076

Arndt, S., Seebach, J., Psathaki, K., Galla, H. J., & Wegener, J. (2004). Bioelectrical impedance assay to monitor changes in cell shape during apoptosis. *Biosensors and Bioelectronics*, *19*(6), 583–594. https://doi.org/10.1016/S0956-5663(03)00269-0

Auger-Messier, M., Arguin, G., Chaloux, B., Leduc, R., Escher, E., & Guillemette, G. (2004). Down-Regulation of Inositol 1,4,5-Trisphosphate Receptor in Cells Stably Expressing the Constitutively Active Angiotensin II N111G-AT $_1$ Receptor. *Molecular Endocrinology*, *18*(12), 2967–2980. https://doi.org/10.1210/me.2003-0488

Axelrod, D. (1981). Cell-substrate contacts illuminated by total internal reflection fluorescence. *Journal of Cell Biology*, *89*(1), 141–145. https://doi.org/10.1083/jcb.89.1.141

Axelrod, D. (2001). Total internal reflection fluorescence microscopy in cell biology. *Traffic*, *2*, 764–774. Retrieved from

http://www.ncbi.nlm.nih.gov/entrez/query.fcgi?cmd=Retrieve&db=PubMed&dopt=Citation&list_uids=12624904

Bahar, R., Hartmann, C. H., Rodriguez, K. a., Denny, A. D., Busuttil, R. a., Dollé, M. E. T., … Vijg, J. (2006). Increased cell-to-cell variation in gene expression in ageing mouse heart. *Nature*, *441*(7096), 1011–1014. https://doi.org/10.1038/nature04844

Balasubramanian, S., Sorokulova, I. B., Vodyanoy, V. J., & Simonian, A. L. (2007). Lytic phage as a specific and selective probe for detection of Staphylococcus aureus—A surface plasmon resonance spectroscopic study. *Biosensors and Bioelectronics*, *22*(6), 948–955. https://doi.org/10.1016/j.bios.2006.04.003

Ballesteros Katemann, B., Schulte, A., Calvo, E. J., Koudelka-Hep, M., & Schuhmann, W. (2002). *Localised electrochemical impedance spectroscopy with high lateral resolution by means of alternating current scanning electrochemical microscopy*. *Electrochemistry Communications* (Vol. 4). https://doi.org/10.1016/S1388-2481(01)00294-6

Banerjee, P., & Bhunia, A. K. (2009). Mammalian cell-based biosensors for pathogens and toxins. *Trends in Biotechnology*, *27*(3), 179–188. https://doi.org/10.1016/j.tibtech.2008.11.006

Banerjee, P., Lenz, D., Robinson, J. P., Rickus, J. L., & Bhunia, A. K. (2008). A novel and simple cell-based detection system with a collagen-encapsulated B-lymphocyte cell line as a biosensor for rapid detection of pathogens and toxins. *Laboratory Investigation*, *88*(2), 196–206. https://doi.org/10.1038/labinvest.3700703

Banville, F., Söllradl, T., Zermatten, P.-J., Grandbois, M., & Charette, P. G. (2015). Improved resolution in SPR and MCWG microscopy by combining images acquired with distinct mode propagation directions. *Optics Letters*, *40*(7), 1165–8. https://doi.org/10.1364/OL.40.001165

Barnes, W. L., Dereux, A., & Ebbesen, T. W. (2003). Surface plamons subwavelength optics. *Nature*, *424*(August), 824–830.

Bauch, M., Toma, K., Toma, M., Zhang, Q., & Dostalek, J. (2013). Plasmon-Enhanced Fluorescence Biosensors: a Review. *Plasmonics*, *9*(4), 781–799. https://doi.org/10.1007/s11468-013-9660-5

Benson, K., Cramer, S., & Galla, H.-J. (2013). Impedance-based cell monitoring: barrier properties and beyond. *Fluids and Barriers of the CNS*, *10*(1), 5.

https://doi.org/10.1186/2045-8118-10-5

Bernard, G. R., Francois, B., Mira, J.-P., Vincent, J.-L., Dellinger, R. P., Russell, J. a., … Wittebole, X. (2014). Evaluating the Efficacy and Safety of Two Doses of the Polyclonal Anti-Tumor Necrosis Factor-α Fragment Antibody AZD9773 in Adult Patients With Severe Sepsis and/or Septic Shock. *Critical Care Medicine*, *42*(3), 504–511. https://doi.org/10.1097/CCM.0000000000000043

Birukova, A. a, Smurova, K., Birukov, K. G., Kaibuchi, K., Garcia, J. G. ., & Verin, A. D. (2004). Role of Rho GTPases in thrombin-induced lung vascular endothelial cells barrier dysfunction. *Microvascular Research*, *67*(1), 64–77. https://doi.org/10.1016/j.mvr.2003.09.007

Blanco Carballo, V. M., Melai, J., Salm, C., & Schmitz, J. (2008). Moisture resistance of SU-8 and KMPR as structural material for integrated gaseous detectors. In *11th Annual Workshop on Semiconductor Advances for Future Electronics and Sensors* (pp. 395–398). Veldhoven: Elsevier. Retrieved from http://doc.utwente.nl/65212/1/blancocarballo.pdf

Bombeli, T., Karsan, A., Tait, J. F., & Harlan, J. M. (1997). Apoptotic vascular endothelial cells become procoagulant. *Blood*, *89*(7), 2429–42. Retrieved from http://www.bloodjournal.org/content/89/7/2429.abstract

Bryche, J.-F., Gillibert, R., Barbillon, G., Gogol, P., Moreau, J., Lamy de la Chapelle, M., … Canva, M. (2016). Plasmonic Enhancement by a Continuous Gold Underlayer: Application to SERS Sensing. *Plasmonics*, *11*(2), 601–608. https://doi.org/10.1007/s11468-015-0088-y

Calander, N. (2004). Theory and Simulation of Surface Plasmon-Coupled Directional Emission from Fluorophores at Planar Structures. *Analytical Chemistry*, *8*(76), 2168–2173. https://doi.org/10.1021/AC049925D

Campbell, L. L., & Polyak, K. (2007). Breast Tumor Heterogeneity: Cancer Stem Cells or Clonal Evolution? *Cell Cycle*, *6*(19), 2332–2338. https://doi.org/10.4161/cc.6.19.4914

Chabot, V., Cuerrier, C. M., Escher, E., Aimez, V., Grandbois, M., & Charette, P. G. (2009). Biosensing based on surface plasmon resonance and living cells. *Biosensors and Bioelectronics*, *24*(6), 1667–1673. https://doi.org/10.1016/j.bios.2008.08.025

Chabot, V., Miron, Y., Charette, P. G., & Grandbois, M. (2013). Identification of the molecular mechanisms in cellular processes that elicit a surface plasmon resonance (SPR) response

using simultaneous surface plasmon-enhanced fluorescence (SPEF) microscopy. *Biosensors & Bioelectronics*, *50*, 125–31. https://doi.org/10.1016/j.bios.2013.06.018

Chabot, V., Miron, Y., Grandbois, M., & Charette, P. G. (2012). Long range surface plasmon resonance for increased sensitivity in living cell biosensing through greater probing depth. *Sensors and Actuators, B: Chemical*, *174*, 94–101. https://doi.org/10.1016/j.snb.2012.08.028

Chen, Y. J., Chen, W. P., & Burstein, E. (1976). Surface-Electromagnetic-Wave-Enhanced Raman Scattering by Overlayers on Metals. *Physical Review Letters*, *36*(20), 1207–1210. https://doi.org/10.1103/PhysRevLett.36.1207

Choi, W., Fang-Yen, C., Badizadegan, K., Oh, S., Lue, N., Dasari, R. R., & Feld, M. S. (2007). Tomographic phase microscopy. *Nature Methods*, *4*(9), 717–719. https://doi.org/10.1038/nmeth1078

Colman-Lerner, A., Gordon, A., Serra, E., Chin, T., Resnekov, O., Endy, D., … Brent, R. (2005). Regulated cell-to-cell variation in a cell-fate decision system. *Nature*, *437*(7059), 699–706. https://doi.org/10.1038/nature03998

Convert, L., Aimez, V., Charette, P. G., & Lecomte, R. (2008). Rapid prototyping of integrated microfluidic devices for combined radiation detection and plasma separation. In *MNRC 2008 - 1st Microsystems and Nanoelectronics Research Conference* (pp. 105–108). Ottawa, ON: IEEE.

Convert, L., Chabot, V., Zermatten, P. J., Hamel, R., Cloarec, J. P., Lecomte, R., … Charette, P. G. (2012). Passivation of KMPR microfluidic channels with bovine serum albumin (BSA) for improved hemocompatibility characterized with metal-clad waveguides. *Sensors and Actuators, B: Chemical*, *173*, 447–454. https://doi.org/10.1016/j.snb.2012.07.061

Coughlin, S. R. (2000). Thrombin signalling and protease-activated receptors. *Nature*, *407*(6801), 258–264. https://doi.org/10.1038/35025229

Cuerrier, C. M., Benoit, M., Guillemette, G., Jr. Gobeil, F., & Grandbois, M. (2009). Real-time monitoring of angiotensin II-induced contractile response and cytoskeleton remodeling in individual cells by atomic force microscopy. *Pflügers Archiv - European Journal of Physiology*, *457*(6), 1361–1372. https://doi.org/10.1007/s00424-008-0596-0

Cuerrier, C. M., Chabot, V., Vigneux, S., Aimez, V., Escher, E., Gobeil, F., … Grandbois, M.

(2008). Surface Plasmon Resonance Monitoring of Cell Monolayer Integrity: Implication of Signaling Pathways Involved in Actin-Driven Morphological Remodeling. *Cellular and Molecular Bioengineering*, *1*(4), 229–239. https://doi.org/10.1007/s12195-008-0028-4

Daimon, M., & Masumura, A. (2007). Measurement of the refractive index of distilled water from the near-infrared region to the ultraviolet region. *Applied Optics*, *46*(18), 3811–3820. https://doi.org/10.1364/AO.46.003811

Dolmetsch, R. E., Xu, K., & Lewis, R. S. (1998). Calcium oscillations increase the efficiency and specificity of gene expression. *Nature*, *392*(6679), 933–936. Retrieved from http://dx.doi.org/10.1038/31960

Dostálek, J., & Knoll, W. (2008). Biosensors based on surface plasmon-enhanced fluorescence spectroscopy. *Biointerphases*, *3*(3), FD12-22. https://doi.org/10.1116/1.2994688

Emmert, D. A., Fee, J. A., Goeckeler, Z. M., Grojean, J. M., Wakatsuki, T., Elson, E. L., … Wysolmerski, R. B. (2003). Rho-kinase-mediated Ca^{2+}-independent contraction in rat embryo fibroblasts. *American Journal of Physiology - Cell Physiology*, *286*(1), C8 LP-C21. Retrieved from http://ajpcell.physiology.org/content/286/1/C8.abstract

Ervin, E. N., White, H. S., & Baker, L. A. (2005). Alternating Current Impedance Imaging of Membrane Pores Using Scanning Electrochemical Microscopy. https://doi.org/10.1021/AC050453S

Fägerstam, L. G., Frostell, a, Karlsson, R., Kullman, M., Larsson, a, Malmqvist, M., & Butt, H. (1990). Detection of antigen-antibody interactions by surface plasmon resonance. Application to epitope mapping. *Journal of Molecular Recognition : JMR*, *3*(5–6), 208–214. https://doi.org/10.1002/jmr.300030507

Fang, Y. (2011). Label-Free Biosensors for Cell Biology. *International Journal of Electrochemistry*, *2011*, 1–16. https://doi.org/10.4061/2011/460850

Fang, Y. (2015). Combining label-free cell phenotypic profiling with computational approaches for novel drug discovery. *Expert Opinion on Drug Discovery*, *10*(4), 331–343. https://doi.org/10.1517/17460441.2015.1020788

Fang, Y., Ferrie, A. M., Fontaine, N. H., Mauro, J., & Balakrishnan, J. (2006). Resonant Waveguide Grating Biosensor for Living Cell Sensing. *Biophysical Journal*, *91*(5), 1925–1940. https://doi.org/10.1529/biophysj.105.077818

Fang, Y., Li, G., & Ferrie, A. M. (2007). Non-invasive optical biosensor for assaying

endogenous G protein-coupled receptors in adherent cells. *Journal of Pharmacological and Toxicological Methods*, *55*(3), 314–322. https://doi.org/10.1016/j.vascn.2006.11.001

Ferrie, A. M., Deichmann, O. D., Wu, Q., & Fang, Y. (2012). High resolution resonant waveguide grating imager for cell cluster analysis under physiological condition. *Applied Physics Letters*, *100*(22), 4–8. https://doi.org/10.1063/1.4723691

Ferrie, A. M., Wu, Q., & Fang, Y. (2010). Resonant waveguide grating imager for live cell sensing. *Applied Physics Letters*, *97*(22), 223704. https://doi.org/10.1063/1.3522894

Fisher, R. J., Fivash, M., Casas-Finet, J., Erickson, J. W., Kondoh, a, Bladen, S. V, … Papas, T. (1994). Real-time DNA binding measurements of the ETS1 recombinant oncoproteins reveal significant kinetic differences between the p42 and p51 isoforms. *Protein Science : A Publication of the Protein Society*, *3*(2), 257–266. https://doi.org/10.1002/pro.5560030210

Fort, E., & Grésillon, S. (2008). Surface enhanced fluorescence. *Journal of Physics D: Applied Physics*, *41*(1), 013001. https://doi.org/10.1088/0022-3727/41/1/013001

Gascoigne, K. E., & Taylor, S. S. (2008). Cancer Cells Display Profound Intra- and Interline Variation following Prolonged Exposure to Antimitotic Drugs. *Cancer Cell*, *14*(2), 111–122. https://doi.org/10.1016/j.ccr.2008.07.002

Giaever, I., & Keese, C. R. (1991). Micromotion of mammalian cells measured electrically. *Proceedings of the National Academy of Sciences of the United States of America*, *88*(17), 7896–900. Retrieved from http://www.ncbi.nlm.nih.gov/pubmed/1881923

Giebel, K., Bechinger, C., Herminghaus, S., Riedel, M., Leiderer, P., Weiland, U., & Bastmeyer, M. (1999). Imaging of cell/substrate contacts of living cells with surface plasmon resonance microscopy. *Biophysical Journal*, *76*(1 Pt 1), 509–16. Retrieved from http://www.pubmedcentral.nih.gov/articlerender.fcgi?artid=1302541&tool=pmcentrez&rendertype=abstract

Gorczyca, W., Gong, J., & Darzynkiewicz, Z. (1993). Detection of DNA strand breaks in individual apoptotic cells by the in situ terminal deoxynucleotidyl transferase and nick translation assays. *Cancer Research*, *53*(8), 1945–51. Retrieved from http://www.ncbi.nlm.nih.gov/pubmed/8467513

Gustafsson, M. G. L. (2005). Nonlinear structured-illumination microscopy: wide-field fluorescence imaging with theoretically unlimited resolution. *Proceedings of the National*

Academy of Sciences of the United States of America, *102*(37), 13081–6. https://doi.org/10.1073/pnas.0406877102

Häcker, G. (2000). The morphology of apoptosis. *Cell and Tissue Research*, *301*(1), 5–17. Retrieved from http://www.ncbi.nlm.nih.gov/pubmed/10928277

Haseyama, M., Sasamura, Y., & Kitajima, H. (2006). An Extraction Method for Apoptotic Cells from Videomicroscopy Images. *Systems and Computers in Japan*, *37*(3), 32–40. https://doi.org/10.1002/scj.20410

He, R.-Y., Chang, G.-L., Wu, H.-L., Lin, C.-H., Chiu, K.-C., Su, Y.-D., & Chen, S.-J. (2006). Enhanced live cell membrane imaging using surface plasmon-enhanced total internal reflection fluorescence microscopy. *Optics Express*, *14*(20), 9307. https://doi.org/10.1364/OE.14.009307

He, R.-Y., Lin, C.-Y., Su, Y.-D., Chiu, K.-C., Chang, N.-S., Wu, H.-L., & Chen, S.-J. (2010). Imaging live cell membranes via surface plasmon-enhanced fluorescence and phase microscopy. *Opt. Express*, *18*(4), 3649–3659. https://doi.org/10.1364/OE.18.003649

He, R.-Y., Su, Y.-D., Cho, K.-C., Lin, C.-Y., Chang, N.-S., Chang, C.-H., & Chen, S.-J. (2009). Surface plasmon-enhanced two-photon fluorescence microscopy for live cell membrane imaging. *Optics Express*, *17*(8), 5987. https://doi.org/10.1364/OE.17.005987

Hecht, E. (2002). *Optics* (4th ed.). Addison Wesley.

Herminghaus, S., & Leiderer, P. (1989). Improved attenuated total reflectance technique for the investigation of dielectric surfaces. *Applied Physics Letters*, *54*(2), 99. https://doi.org/10.1063/1.101201

Hide, M., Tsutsui, T., Sato, H., Nishimura, T., Morimoto, K., Yamamoto, S., & Yoshizato, K. (2002). Real-Time Analysis of Ligand-Induced Cell Surface and Intracellular Reactions of Living Mast Cells Using a Surface Plasmon Resonance-Based Biosensor. *Analytical Biochemistry*, *302*(1), 28–37. https://doi.org/10.1006/abio.2001.5535

Homola, J. (2003). Present and future of surface plasmon resonance biosensors. *Analytical and Bioanalytical Chemistry*, *377*(3), 528–539. https://doi.org/10.1007/s00216-003-2101-0

Huang, B., Yu, F., & Zare, R. N. (2007). Surface plasmon resonance imaging using a high numerical aperture microscope objective. *Analytical Chemistry*, *79*(7), 2979–83. https://doi.org/10.1021/ac062284x

Huang, C. J., Dostalek, J., Sessitsch, A., & Knoll, W. (2011). Long-range surface plasmon-

enhanced fluorescence spectroscopy biosensor for ultrasensitive detection of E. coli O157:H7. *Analytical Chemistry*, *83*(3), 674–677. https://doi.org/10.1021/ac102773r

Huh, S., Ker, D. F. E., Su, H., & Kanade, T. (2012). Apoptosis Detection for Adherent Cell Populations in Time-lapse Phase-contrast Microscopy Images. In *Medical Image Computing and Computer-Assisted Intervention – MICCAI 2012* (pp. 331–339).

Jamil, M. M. A., Denyer, M. C. T., Youseffi, M., Britland, S. T., Liu, S., See, C. W., … Zhang, J. (2008). Imaging of the cell surface interface using objective coupled widefield surface plasmon microscopy. *Journal of Structural Biology*, *164*(1), 75–80. https://doi.org/10.1016/j.jsb.2008.06.005

Jamil, M. M. A., Youseffi, M., Britland, S. T., Liu, S., See, C. W., Somekh, M. G., & Denyer, M. C. T. (2007). Widefield Surface Plasmon Resonance Microscope : A Novel Biosensor Study of Cell Attachment to Micropatterned Substrates. *Image (Rochester, N.Y.)*, *15*, 334–337.

Jirí Homola. (2006). *Surface Plasmon Resonance Based Sensors*. *Springer Series on Chemical Sensors and Biosensors* (Vol. 4). https://doi.org/10.1007/b100321

Johnson, P. B., & Christy, R. W. (1972). Optical Constants of the Noble Metals. *Physical Review B*, *6*(12), 4370–4379. https://doi.org/10.1103/PhysRevB.6.4370

Kaminow, I. P., Mammel, W. L., & Weber, H. P. (1974). Metal-Clad Optical Waveguides: Analytical and Experimental Study. *Applied Optics*, *13*(2), 396. https://doi.org/10.1364/AO.13.000396

Kanchanawong, P., Shtengel, G., Pasapera, A. M., Ramko, E. B., Davidson, M. W., Hess, H. F., & Waterman, C. M. (2010). Nanoscale architecture of integrin-based cell adhesions. *Nature*, *468*(7323), 580–584. https://doi.org/10.1038/nature09621

Kano, H., & Knoll, W. (2000). A scanning microscope employing localized surface-plasmon-polaritons as a sensing probe. *Optics Communications*, *182*(1–3), 11–15. https://doi.org/10.1016/S0030-4018(00)00794-X

Kasry, A., & Knoll, W. (2006). Long range surface plasmon fluorescence spectroscopy. *Applied Physics Letters*, *89*(10), 101106. https://doi.org/10.1063/1.2345594

Kaufman, W. L., Kocman, I., Agrawal, V., Rahn, H.-P., Besser, D., & Gossen, M. (2008). Homogeneity and persistence of transgene expression by omitting antibiotic selection in cell line isolation. *Nucleic Acids Research*, *36*(17), e111–e111.

https://doi.org/10.1093/nar/gkn508

Kim, D. J., & Kim, D. (2010). Subwavelength grating-based nanoplasmonic modulation for surface plasmon resonance imaging with enhanced resolution. *Journal of the Optical Society of America B*, *27*(6), 1252. https://doi.org/10.1364/JOSAB.27.001252

Kim, S.-H., Chegal, W., Doh, J., Cho, H. M., & Moon, D. W. (2011). Study of cell-matrix adhesion dynamics using surface plasmon resonance imaging ellipsometry. *Biophysical Journal*, *100*(7), 1819–28. https://doi.org/10.1016/j.bpj.2011.01.033

Knoll, W., Frank, C. W., Heibel, C., Naumann, R., Offenhäusser, a, Rühe, J., … Sinner, a. (2000). Functional tethered lipid bilayers. *Journal of Biotechnology*, *74*(3), 137–158. https://doi.org/10.1016/S1389-0352(00)00012-X

Koopman, G., Reutelingsperger, C. P., Kuijten, G. A., Keehnen, R. M., Pals, S. T., & van Oers, M. H. (1994). Annexin V for flow cytometric detection of phosphatidylserine expression on B cells undergoing apoptosis. *Blood*, *84*(5), 1415–20. Retrieved from http://www.ncbi.nlm.nih.gov/pubmed/8068938

Kosaihira, A., & Ona, T. (2008). Rapid and quantitative method for evaluating the personal therapeutic potential of cancer drugs. *Analytical and Bioanalytical Chemistry*, *391*(5), 1889–1897. https://doi.org/10.1007/s00216-008-2152-3

Kretschmann, E., & Raether, H. (1968). Radiative decay of non-radiative surface plasmons excited by light. *Z. Naturforsch.*, *23*(November 1968), 2135–2136. https://doi.org/citeulike-article-id:3901347

Krupin, O., Asiri, H., Wang, C., Tait, R. N., & Berini, P. (2013). Biosensing using straight long-range surface plasmon waveguides. *Optics Express*, *21*(1), 698. https://doi.org/10.1364/OE.21.000698

Lahav, G., Rosenfeld, N., Sigal, A., Geva-Zatorsky, N., Levine, A. J., Elowitz, M. B., & Alon, U. (2004). Dynamics of the p53-Mdm2 feedback loop in individual cells. *Nature Genetics*, *36*(2), 147–150. https://doi.org/10.1038/ng1293

Lakowicz, J. R. (Ed.). (2006). *Principles of Fluorescence Spectroscopy*. Boston, MA: Springer US. https://doi.org/10.1007/978-0-387-46312-4

Laplatine, L., Leroy, L., Calemczuk, R., Baganizi, D., Marche, P. N., Roupioz, Y., & Livache, T. (2014). Spatial resolution in prism-based surface plasmon resonance microscopy. *Optics Express*, *22*(19), 22771. https://doi.org/10.1364/OE.22.022771

Levskaya, A., Chevalier, A. A., Tabor, J. J., Simpson, Z. B., Lavery, L. A., Levy, M., … Voigt, C. A. (2005). Engineering Escherichia coli to see light. *Nature*, *438*, 441. Retrieved from http://dx.doi.org/10.1038/nature04405

Liebermann, T., & Knoll, W. (2000). Surface-plasmon field-enhanced fluorescence spectroscopy. *Colloids and Surfaces A: Physicochemical and Engineering Aspects*, *171*(1–3), 115–130. https://doi.org/10.1016/S0927-7757(99)00550-6

Liedberg, B., Lundström, I., & Nylander, C. (1983). Surface plasmon resonance for gas detection and biosensing. *Sensors and Actuators*, *4*, 299. Retrieved from http://www.sciencedirect.com/science/article/B6W97-44W5H3C-4P/2/f9c827c89a8baa32c622fe0a2ff7afee

Liedberg, B., Nylander, C., M, L. ¨, & I. (1995). Biosensing with surface plasmon resonance - how it all started, Biosens. *Bioelectron*, *10i*, ix.

Liu, Q., Wu, C., Cai, H., Hu, N., Zhou, J., & Wang, P. (2014). Cell-Based Biosensors and Their Application in Biomedicine. *Chemical Reviews*, *114*(12), 6423–6461. https://doi.org/10.1021/cr2003129

Liu, Y., Chin, L. K., Ser, W., Chen, H., Hsieh, C.-M., Lee, C.-H., … Leprince-Wang, Y. (2015). Cell Refractive Index for Cell Biology and Disease Diagnosis: Past, Present and Future. *Lab Chip*, *16*(4), 634–644. https://doi.org/10.1039/C5LC01445J

Lo, C. M., Keese, C. R., & Giaever, I. (1993). Monitoring motion of confluent cells in tissue culture. *Experimental Cell Research*. https://doi.org/10.1006/excr.1993.1014

Maltais, J.-S., Denault, J.-B., Gendron, L., & Grandbois, M. (2012). Label-free monitoring of apoptosis by surface plasmon resonance detection of morphological changes. *Apoptosis : An International Journal on Programmed Cell Death*, *17*(8), 916–25. https://doi.org/10.1007/s10495-012-0737-y

Maltais, J.-S., Simard, E., Froehlich, U., Denault, J.-B., Gendron, L., & Grandbois, M. (2016). iRAGE as a novel carboxymethylated peptide that prevents advanced glycation end product-induced apoptosis and endoplasmic reticulum stress in vascular smooth muscle cells. *Pharmacological Research*, *104*, 176–85. https://doi.org/10.1016/j.phrs.2015.12.015

Marx, K. a., Zhou, T., Montrone, A., Schulze, H., & Braunhut, S. J. (2001). A quartz crystal microbalance cell biosensor: Detection of microtubule alterations in living cells at nM nocodazole concentrations. *Biosensors and Bioelectronics*, *16*, 773–782.

https://doi.org/10.1016/S0956-5663(01)00219-6

McLaughlin, J. N. (2005). Functional Selectivity of G Protein Signaling by Agonist Peptides and Thrombin for the Protease-activated Receptor-1. *Journal of Biological Chemistry*, *280*(26), 25048–25059. https://doi.org/10.1074/jbc.M414090200

Méjard, R., Dostálek, J., Huang, C.-J., Griesser, H., & Thierry, B. (2013). Tuneable and robust long range surface plasmon resonance for biosensing applications. *Optical Materials*, *35*(12), 2507–2513. https://doi.org/10.1016/j.optmat.2013.07.011

Melino, G., & Vaux, D. (2010). *Cell Death*. John Wiley & Sons.

Michaelis, S., Wegener, J., & Robelek, R. (2013). Label-free monitoring of cell-based assays: Combining impedance analysis with SPR for multiparametric cell profiling. *Biosensors & Bioelectronics*, *49*(15), 63–70. https://doi.org/http://dx.doi.org/10.1016/j.bios.2013.04.042

Moreau, J., Cloarec, J.-P., Charette, P., Goossens, M., Canva, M., & Vo-Dinh, T. (2014). Chapter 7. Surface Plasmon Resonance Imaging Sensors:: Principle, Development, and Biomedical Applications—Example of Genotyping. In T. Vo-Dinh (Ed.), *Biomedical Diagnostics* (pp. 199–264). CRC Press. https://doi.org/10.1201/b17289-9

Murakami, T., Arima, Y., Toda, M., Takiguchi, H., & Iwata, H. (2012). Effect of dielectric spacer thickness on signal intensity of surface plasmon field-enhanced fluorescence spectroscopy. *Analytical Biochemistry*, *421*(2), 632–9. https://doi.org/10.1016/j.ab.2011.12.008

Nakkach, M., Lecaruyer, P., Bardin, F., Sakly, J., Lakhdar, Z. Ben, & Canva, M. (2008). Absorption and related optical dispersion effects on the spectral response of a surface plasmon resonance sensor. *Applied Optics*, *47*(33), 6177–6182. https://doi.org/10.1364/AO.47.006177

Nemetz, A., & Knoll, W. (1996). Raman Spectroscopy and Microscopy with Plasmon Surface Polaritons. *Journal of Raman Spectroscopy*, *27*(8), 587–592. https://doi.org/10.1002/(SICI)1097-4555(199608)27:8<587::AID-JRS14>3.0.CO;2-0

Nickenig, G., Sachinidis, a., Michaelsen, F., Bohm, M., Seewald, S., & Vetter, H. (1997). Upregulation of Vascular Angiotensin II Receptor Gene Expression by Low-Density Lipoprotein in Vascular Smooth Muscle Cells. *Circulation*, *95*(2), 473–478. https://doi.org/10.1161/01.CIR.95.2.473

Nishijima, H., Kosaihira, A., Shibata, J., & Ona, T. (2010). Development of signaling echo

method for cell-based quantitative efficacy evaluation of anti-cancer drugs in apoptosis without drug presence using high-precision surface plasmon resonance sensing. *Analytical Sciences : The International Journal of the Japan Society for Analytical Chemistry*, *26*(5), 529–34. https://doi.org/10.2116/analsci.26.529

Nylander, C., Liedberg, B., & Lind, T. (1982). Gas detection by means of surface plasmon resonance. *Sensors and Actuators*, *3*, 79–88. https://doi.org/10.1016/0250-6874(82)80008-5

Olveczky, B. P., Periasamy, N., & Verkman, A. S. (1997). Mapping fluorophore distributions in three dimensions by quantitative multiple angle-total internal reflection fluorescence microscopy. *Biophysical Journal*, *73*(5), 2836–47. https://doi.org/10.1016/S0006-3495(97)78312-7

Ong, B. H., Yuan, X., Tjin, S. C., Zhang, J., & Ng, H. M. (2006). Optimised film thickness for maximum evanescent field enhancement of a bimetallic film surface plasmon resonance biosensor. *Sensors and Actuators, B: Chemical*, *114*(2), 1028–1034. https://doi.org/10.1016/j.snb.2005.07.064

Osterfeld, M., Franke, H., & Feger, C. (1993). Optical gas detection using metal film enhanced leaky mode spectroscopy. *Applied Physics Letters*, *62*(19), 2310. https://doi.org/10.1063/1.109401

Otsu, N. (1979). A Threshold Selection Method from Gray-Level Histograms. *IEEE Transactions on Systems, Man, and Cybernetics*, *9*(1), 62–66. https://doi.org/10.1109/TSMC.1979.4310076

Otto, A. (1968). Excitation of nonradiative surface plasma waves in silver by the method of frustrated total reflection. *Zeitschrift Für Physik*, *216*(4), 398–410. https://doi.org/10.1007/BF01391532

Otto, A., & Sohler, W. (1971). Modification of the total reflection modes in a dielectric film by one metal boundary. *Optics Communications*, *3*(4), 254–258. https://doi.org/10.1016/0030-4018(71)90017-4

Ou, K.-S., Yan, H.-Y., & Chen, K.-S. (2008). Mechanical Characterization of KMPR by Nano-Indentation for MEMS Applications. *Strain*, *44*(3), 267–271. https://doi.org/10.1111/j.1475-1305.2007.00367.x

Owens, G. K. (1995). Regulation of differentiation of vascular smooth muscle cells.

Physiological Reviews, *75*(3), 487 LP-517. Retrieved from http://physrev.physiology.org/content/75/3/487.abstract

Owens, G. K., Kumar, M. S., & Wamhoff, B. R. (2004). Molecular Regulation of Vascular Smooth Muscle Cell Differentiation in Development and Disease. *Physiological Reviews*, *84*(3), 767 LP-801. Retrieved from http://physrev.physiology.org/content/84/3/767.abstract

Paddon, C. J., Westfall, P. J., Pitera, D. J., Benjamin, K., Fisher, K., McPhee, D., … Newman, J. D. (2013). High-level semi-synthetic production of the potent antimalarial artemisinin. *Nature*, *496*, 528. Retrieved from http://dx.doi.org/10.1038/nature12051

Palczewski, K., Kumasaka, T., Hori, T., Behnke, C. A., Motoshima, H., Fox, B. A., … Miyano, M. (2000). Crystal Structure of Rhodopsin: A G Protein-Coupled Receptor. *Science*, *289*(5480), 739 LP-745. Retrieved from http://science.sciencemag.org/content/289/5480/739.abstract

Pancrazio, J. J., Whelan, J. P., Borkholder, D. A., Ma, W., & Stenger, D. A. (1999). Development and application of cell-based biosensors. *Annals of Biomedical Engineering*, *27*(6), 697–711. Retrieved from http://www.ncbi.nlm.nih.gov/pubmed/10625143

Park, J. K., Lee, S. O., Kim, Y. G., Kim, S. H., Koh, G. Y., & Cho, K. W. (2002). Role of rho-kinase activity in angiotensin II-induced contraction of rabbit clitoral cavernosum smooth muscle. *International Journal of Impotence Research*, *14*(6), 472–477. https://doi.org/10.1038/sj.ijir.3900911

Peterson, A. W., Halter, M., Tona, A., Bhadriraju, K., & Plant, A. L. (2009). Surface plasmon resonance imaging of cells and surface-associated fibronectin. *BMC Cell Biology*, *10*(1), 16. https://doi.org/10.1186/1471-2121-10-16

Peterson, A. W., Halter, M., Tona, A., & Plant, A. L. (2014). High resolution surface plasmon resonance imaging for single cells. *BMC Cell Biology*, *15*(1), 35. https://doi.org/10.1186/1471-2121-15-35

Podgorsek, R. P., & Franke, H. (1998). Optical determination of molecule diffusion coefficients in polymer films. *Applied Physics Letters*, *73*(20), 2887. https://doi.org/10.1063/1.122619

Podgorsek, R. P., Sterkenburgh, T., Wolters, J., Ehrenreich, T., Nischwitz, S., & Franke, H. (1997). Optical gas sensing by evaluating ATR leaky mode spectra. *Sensors and Actuators B: Chemical*, *39*(1–3), 349–352. https://doi.org/10.1016/S0925-4005(97)80232-8

Pollock, C. R., & Lipson, M. (2003). *Integrated Photonics*. Boston, MA: Springer US. https://doi.org/10.1007/978-1-4757-5522-0

Pyo, H.-B., Shin, Y.-B., Kim, M.-G., & Yoon, H. C. (2005). Multichannel surface plasmon resonance imaging and analysis of micropatterned self-assembled monolayers and protein affinity interactions. *Langmuir : The ACS Journal of Surfaces and Colloids*, *21*(1), 166–71. https://doi.org/10.1021/la0486382

Raser, J. M., & O'Shea, E. K. (2005). Noise in gene expression: origins, consequences, and control. *Science (New York, N.Y.)*, *309*(5743), 2010–3. https://doi.org/10.1126/science.1105891

Rawson, D. M., Willmer, a J., & Turner, a P. (1989). Whole-cell biosensors for environmental monitoring. *Biosensors*, *4*(5), 299–311. https://doi.org/10.1016/0265-928X(89)80011-2

Reisinger, A. (1973). Characteristics of Optical Guided Modes in Lossy Waveguides. *Applied Optics*, *12*(5), 1015. https://doi.org/10.1364/AO.12.001015

Rothenhäusler, B., & Knoll, W. (1988). Surface-plasmon microscopy. *Nature*, *332*, 615–617. https://doi.org/10.1038/332615a0

Rothenhäusler, B., & Knoll, W. (1988). Surface plasmon interferometry in the visible. *Applied Physics Letters*, *52*(19), 1554. https://doi.org/10.1063/1.99698

Sakata, T., & Sugimoto, H. (2011). Continuous Monitoring of Electrical Activity of Pancreatic β-Cells Using Semiconductor-Based Biosensing Devices. *Japanese Journal of Applied Physics*, *50*(2), 020216. https://doi.org/10.1143/JJAP.50.020216

Salamon, Z., Macleod, H. A., & Tollin, G. (1997). Coupled plasmon-waveguide resonators: a new spectroscopic tool for probing proteolipid film structure and properties. *Biophysical Journal*, *73*(5), 2791–2797. https://doi.org/10.1016/S0006-3495(97)78308-5

Salamon, Z., & Tollin, G. (2001). Optical anisotropy in lipid bilayer membranes: coupled plasmon-waveguide resonance measurements of molecular orientation, polarizability, and shape. *Biophysical Journal*, *80*(3), 1557–1567. https://doi.org/10.1016/S0006-3495(01)76128-0

Samadani, A., Mettetal, J., & van Oudenaarden, A. (2006). Cellular asymmetry and individuality in directional sensing. *Proceedings of the National Academy of Sciences of the United States of America*, *103*(31), 11549–54. https://doi.org/10.1073/pnas.0601909103

Schröder, R., Janssen, N., Schmidt, J., Kebig, A., Merten, N., Hennen, S., … Kostenis, E. (2010). Deconvolution of complex G protein–coupled receptor signaling in live cells using dynamic mass redistribution measurements. *Nature Biotechnology*, *28*(9), 943–949. https://doi.org/10.1038/nbt.1671

Scott, C. W., & Peters, M. F. (2010). Label-free whole-cell assays: expanding the scope of GPCR screening. *Drug Discovery Today*, *15*(17–18), 704–716. https://doi.org/10.1016/j.drudis.2010.06.008

Seebach, J., Taha, A. A., Lenk, J., Lindemann, N., Jiang, X., Brinkmann, K., … Schnittler, H.-J. (2015). The CellBorderTracker, a novel tool to quantitatively analyze spatiotemporal endothelial junction dynamics at the subcellular level. *Histochemistry and Cell Biology*, *144*(6), 517–532. https://doi.org/10.1007/s00418-015-1357-8

Sereda, A., Moreau, J., Canva, M., & Maillart, E. (2014). High performance multi-spectral interrogation for surface plasmon resonance imaging sensors. *Biosensors and Bioelectronics*, *54*, 175–180. https://doi.org/10.1016/j.bios.2013.10.049

Skivesen, N., Horvath, R., & Pedersen, H. C. (2005). Optimization of metal-clad waveguide sensors. *Sensors and Actuators B: Chemical*, *106*(2), 668–676. https://doi.org/10.1016/j.snb.2004.09.014

Skivesen, N., Horvath, R., Thinggaard, S., Larsen, N. B., & Pedersen, H. C. (2007). Deep-probe metal-clad waveguide biosensors. *Biosensors and Bioelectronics*, *22*(7), 1282–1288. https://doi.org/10.1016/j.bios.2006.05.025

Slack, M. D., Martinez, E. D., Wu, L. F., & Altschuler, S. J. (2008). Characterizing heterogeneous cellular responses to perturbations. *Proceedings of the National Academy of Sciences of the United States of America*, *105*(49), 19306–19311. https://doi.org/10.1073/pnas.0807038105

Smith, E. A., & Corn, R. M. (2003). Surface Plasmon Resonance Imaging as a Tool to Monitor Biomolecular Interactions in an Array Based Format. *Applied Spectroscopy*, *57*(11), 320A–332A. Retrieved from http://as.osa.org/abstract.cfm?URI=as-57-11-320A

Söllradl, T., Banville, F. A., Chabot, V., Canva, M., Grandbois, M., & Charette, P. G. (2017). Metal clad waveguide (MCWG) based imaging using a high numerical aperture microscope objective. *Optics Express*, *25*(3), 1666. https://doi.org/10.1364/OE.25.001666

Söllradl, T., Banville, F. A., Froehlich, U., Canva, M., Charette, P. G., & Grandbois, M. (2018).

Label-free visualization and quantification of single cell signaling activity using metal-clad waveguide (MCWG)-based microscopy. *Biosensors and Bioelectronics*, *100*, 429–436. https://doi.org/10.1016/J.BIOS.2017.09.002

Stabler, G., Somekh, M. G., & See, C. W. (2004). High-resolution wide-field surface plasmon microscopy. *Journal of Microscopy*, *214*(3), 328–333. https://doi.org/10.1111/j.0022-2720.2004.01309.x

Stolwijk, J. a., Matrougui, K., Renken, C. W., & Trebak, M. (2015). Impedance analysis of GPCR-mediated changes in endothelial barrier function: overview and fundamental considerations for stable and reproducible measurements. *Pflügers Archiv - European Journal of Physiology*, *467*(10), 2193–2218. https://doi.org/10.1007/s00424-014-1674-0

Suematsu, Y., Hakuta, M., Furuya, K., Chiba, K., & Hasumi, R. (1972). Fundamental transverse electric field (TE0) mode selection for thin-film asymmetric light guides. *Applied Physics Letters*, *21*(6), 291. https://doi.org/10.1063/1.1654383

Sund, S. E., Swanson, J. A., & Axelrod, D. (1999). Cell Membrane Orientation Visualized by Polarized Total Internal Reflection Fluorescence. *Biophysical Journal*, *77*(4), 2266–2283. https://doi.org/10.1016/S0006-3495(99)77066-9

Tamir, T. (1975). *Integrated Optics*. Springer-Verlag Berlin Heidelberg. https://doi.org/10.1007/978-3-662-43208-2

Tiruppathi, C., Malik, a B., Del Vecchio, P. J., Keese, C. R., & Giaever, I. (1992). Electrical method for detection of endothelial cell shape change in real time: assessment of endothelial barrier function. *Proc Natl Acad Sci U S A*, *89*(17), 7919–7923. Retrieved from http://www.ncbi.nlm.nih.gov/pubmed/1518814%5Cnhttp://www.pnas.org/content/89/17/7919.full.pdf

Tsien, R. Y. (1998). The Green Fluorescent Protein. *Annual Review of Biochemistry*, *67*(1), 509–544. https://doi.org/10.1146/annurev.biochem.67.1.509

Tumolo, T., Angnes, L., & Baptista, M. S. (2004). Determination of the refractive index increment (dn/dc) of molecule and macromolecule solutions by surface plasmon resonance. *Analytical Biochemistry*, *333*(2), 273–279. https://doi.org/10.1016/j.ab.2004.06.010

Vaisocherová, H., Zítová, A., Lachmanová, M., Stepánek, J., Králíková, S., Liboska, R., … Homola, J. (2006). Investigating oligonucleotide hybridization at subnanomolar level by

surface plasmon resonance biosensor method. *Biopolymers*, *82*(4), 394–398. https://doi.org/10.1002/bip.20433

Wang, W., Foley, K., Shan, X., Wang, S., Eaton, S., Nagaraj, V. J., … Tao, N. (2011). Single cells and intracellular processes studied by a plasmonic-based electrochemical impedance microscopy. *Nature Chem.*, *3*(3), 249–255. https://doi.org/10.1038/nchem.961

Wang, W., Wang, S., Liu, Q., Wu, J., & Tao, N. (2012). Mapping single-cell-substrate interactions by surface plasmon resonance microscopy. *Langmuir : The ACS Journal of Surfaces and Colloids*, *28*(37), 13373–9. https://doi.org/10.1021/la301712h

Wang, W., Yang, Y., Wang, S., Nagaraj, V. J., Liu, Q., Wu, J., & Tao, N. (2012). Label-free measuring and mapping of binding kinetics of membrane proteins in single living cells. *Nature Chemistry*, *4*(10), 846–853. https://doi.org/10.1038/nchem.1434

Ward, L. D., Howlett, G. J., Hammacher, A., Weinstock, J., Yasukawa, K., Simpson, R. J., & Winzor, D. J. (1995). Use of a Biosensor with Surface Plasmon Resonance Detection for the Determination of Binding Constants: Measurement of Interleukin-6 Binding to the Soluble Interleukin-6 Receptor. *Biochemistry*, *34*(9), 2901–2907. https://doi.org/10.1021/bi00009a021

Wark, A. W., Hye Jin Lee, A., & Corn*, R. M. (2005). Long-Range Surface Plasmon Resonance Imaging for Bioaffinity Sensors. https://doi.org/10.1021/AC050402V

Wechsler, M. E., Lehman, E., Lazarus, S. C., Lemanske, R. F., Boushey, H. A., Deykin, A., … Israel, E. (2006). beta-Adrenergic receptor polymorphisms and response to salmeterol. *American Journal of Respiratory and Critical Care Medicine*, *173*(5), 519–26. https://doi.org/10.1164/rccm.200509-1519OC

Wegener, J., & Seebach, J. (2014). Experimental tools to monitor the dynamics of endothelial barrier function: A survey of in vitro approaches. *Cell and Tissue Research*, *355*, 485–514. https://doi.org/10.1007/s00441-014-1810-3

Wen, L. P., Fahrni, J. a., Troie, S., Guan, J. L., Orth, K., & Rosen, G. D. (1997). Cleavage of focal adhesion kinase by caspases during apoptosis. *Journal of Biological Chemistry*, *272*(41), 26056–26061. https://doi.org/10.1074/jbc.272.41.26056

Wood, R. W. (1902). On a Remarkable Case of Uneven Distribution of Light in a Diffraction Grating Spectrum. *Proceedings of the Physical Society of London*, *18*(1), 269–275. https://doi.org/10.1088/1478-7814/18/1/325

Yanase, Y., Hiragun, T., Ishii, K., Kawaguchi, T., Yanase, T., Kawai, M., … Hide, M. (2014). Surface Plasmon Resonance for Cell-Based Clinical Diagnosis. *Sensors*, *14*(3), 4948–4959. https://doi.org/10.3390/s140304948

Yanase, Y., Hiragun, T., Kaneko, S., Gould, H. J., Greaves, M. W., & Hide, M. (2010). Detection of refractive index changes in individual living cells by means of surface plasmon resonance imaging. *Biosensors & Bioelectronics*, *26*(2), 674–81. https://doi.org/10.1016/j.bios.2010.06.065

Yanase, Y., Suzuki, H., Tsutsui, T., Hiragun, T., Kameyoshi, Y., & Hide, M. (2007). The SPR signal in living cells reflects changes other than the area of adhesion and the formation of cell constructions. *Biosensors & Bioelectronics*, *22*, 1081–1086. https://doi.org/10.1016/j.bios.2006.03.011

Yang, M. K., French, R. H., & Tokarsky, E. W. (2008). Optical properties of Teflon® AF amorphous fluoropolymers. *Journal of Micro/Nanolithography, MEMS and MOEMS*, *7*(3), 033010. https://doi.org/10.1117/1.2965541

Yang, M., Yau, H. C. M., & Chan, H. L. (1998). Adsorption Kinetics and Ligand-Binding Properties of Thiol-Modified Double-Stranded DNA on a Gold Surface. *Langmuir*, *14*(21), 6121–6129. https://doi.org/10.1021/la980577i

Yao, D., Yu, F., Kim, J., Scholz, J., Nielsen, P. E., Sinner, E.-K., & Knoll, W. (2004). Surface plasmon field-enhanced fluorescence spectroscopy in PCR product analysis by peptide nucleic acid probes. *Nucleic Acids Research*, *32*(22), e177. https://doi.org/10.1093/nar/gnh175

Yashunsky, V., Kharilker, L., Zlotkin-Rivkin, E., Rund, D., Melamed-Book, N., Zahavi, E. E., … Aroeti, B. (2013). Real-Time Sensing of Enteropathogenic E. coli-Induced Effects on Epithelial Host Cell Height, Cell-Substrate Interactions, and Endocytic Processes by Infrared Surface Plasmon Spectroscopy. *PLoS ONE*, *8*(10), e78431. https://doi.org/10.1371/journal.pone.0078431

Yashunsky, V., Lirtsman, V., Golosovsky, M., Davidov, D., & Aroeti, B. (2010). Real-Time Monitoring of Epithelial Cell-Cell and Cell-Substrate Interactions by Infrared Surface Plasmon Spectroscopy. *Biophysical Journal*, *99*(12), 4028–4036. https://doi.org/10.1016/j.bpj.2010.10.017

Yashunsky, V., Marciano, T., Lirtsman, V., Golosovsky, M., Davidov, D., Aroeti, B., … Gat,

U. (2012). Real-Time Sensing of Cell Morphology by Infrared Waveguide Spectroscopy. *PLoS ONE*, *7*(10), e48454. https://doi.org/10.1371/journal.pone.0048454

Yeatman, E. M. (1996). Resolution and sensitivity in surface plasmon microscopy and sensing. *Biosensors and Bioelectronics*, *11*(6–7), 635–649. https://doi.org/10.1016/0956-5663(96)83298-2

Yeh, P. (2005). *Optical waves in layered media*. New Jersey: Wiley.

Yu, F., Persson, B., Löfås, S., & Knoll, W. (2004). Surface plasmon fluorescence immunoassay of free prostate-specific antigen in human plasma at the femtomolar level. *Analytical Chemistry*, *76*(22), 6765–6770. https://doi.org/10.1021/ac048937w

Yu, F., Yao, D., & Knoll, W. (2003). Surface Plasmon Field-Enhanced Fluorescence Spectroscopy Studies of the Interaction between an Antibody and Its Surface-Coupled Antigen. *Analytical Chemistry*, *75*(11), 2610–2617. https://doi.org/10.1021/ac026161y

Ziegler, C. (2000). Cell-based biosensors, 552–559.

Zourob, M., & Goddard, N. J. (2005). Metal clad leaky waveguides for chemical and biosensing applications. *Biosensors and Bioelectronics*, *20*(9), 1718–1727. https://doi.org/10.1016/j.bios.2004.06.031

Zourob, M., Mohr, S., Brown, B., Fielden, P., Mcdonnell, M., & Goddard, N. (2005). Bacteria detection using disposable optical leaky waveguide sensors. *Biosensors and Bioelectronics*, *21*(2), 293–302. https://doi.org/10.1016/j.bios.2004.10.013

Zourob, M., Mohr, S., Brown, B. J. T., Fielden, P. R., McDonnell, M., & Goddard, N. J. (2003). The development of a metal clad leaky waveguide sensor for the detection of particles. *Sensors and Actuators B: Chemical*, *90*(1–3), 296–307. https://doi.org/10.1016/S0925-4005(03)00052-2